

Summer 2020

Evaluation of Temporal Damage Progression in Concrete Structures Affected by ASR Using Data-driven Methods

Vafa Soltangharaei

Follow this and additional works at: <https://scholarcommons.sc.edu/etd>



Part of the [Civil Engineering Commons](#)

Recommended Citation

Soltangharaei, V.(2020). *Evaluation of Temporal Damage Progression in Concrete Structures Affected by ASR Using Data-driven Methods*. (Doctoral dissertation). Retrieved from <https://scholarcommons.sc.edu/etd/6080>

This Open Access Dissertation is brought to you by Scholar Commons. It has been accepted for inclusion in Theses and Dissertations by an authorized administrator of Scholar Commons. For more information, please contact dillarda@mailbox.sc.edu.

Evaluation of Temporal Damage Progression in Concrete Structures
Affected by ASR Using Data-driven Methods

by

Vafa Soltangharai

Bachelor of Science
Azad University Central Tehran Branch, 2007

Master of Science
Building & Housing Research Center, 2011

Submitted in Partial Fulfillment of the Requirements

For the Degree of Doctor of Philosophy in

Civil Engineering

College of Engineering and Computing

University of South Carolina

2020

Accepted by

Paul Ziehl, Major Professor

Juan Caicedo, Committee Member

Sarah Gassman, Committee Member

John Rose, Committee Member

Cheryl L. Addy, Vice Provost and Dean of the Graduate School

© Copyright by Vafa Soltangharai, 2020
All Rights Reserved.

Dedication

To my father and mother.

Acknowledgments

This work would not be accomplished, unless unsparing help and supports of many people. I am very grateful for their supports. First, my deepest gratitude is to my advisor, Dr. Paul Ziehl, who has always guided me through the course of this work. Working with him is one of the greatest experiences I have had in my life. He gave me an opportunity to involve in different projects and helped me to test my ability to deal with problems and challenges. During difficulties and problems, I have always had his supports and encouragement, which have made me more determined and motivated to move forward and fight rather than surrounded. I would like to appreciate my committee members, Dr. Juan Caicedo, Dr. John Rose, and Dr. Sarah Gassman to provide me with their guidance and comments during my research.

I am also grateful to my friends and colleagues at the University of South Carolina, especially Rafal Anay, Lateef Assi, Li Ai, and Xiaoqun Yan to help me in my research. Thanks to my parents and my sisters for their supports and encouragements.

The financial supports provided by U. S Department of Energy, Office of Basic Energy Sciences and Office of Biological and Environmental Research under Award Number DE-SC-00012530, Department of Energy-Nuclear Energy University Program (NEUP) under the contract DE-NE0008544, South Carolina Department of Transportation, and Fokker Company are acknowledged.

Abstract

Alkali-silica reaction (ASR) is a chemical reaction, which causes damage in concrete structures such as bridges, dams, and nuclear containments and powerplant structures. The ASR-induced damage may endanger the integrity and serviceability of structures. Several methods such as visual inspection, petrographic analysis, demountable mechanical strain gauges, and cracking index have been utilized for study the effect of ASR on structures, which are not always efficient in early damage detection and some are destructive and prohibited in nuclear structures. Nondestructive methods and structural health monitoring techniques can be alternatives for the condition assessment of structures. Among the nondestructive methods, acoustic emission (AE) is preferable due to high sensitivity of AE sensors, source localization ability, and sensing capability in one-side-access structures. The goal is the condition assessment of structures affected by ASR using AE. Therefore, in the current research, data-driven methods in combination with signal processing techniques are employed to find a potential temporal trend in the AE data and relate the trend to the damage progression caused by ASR. In addition, the effect of stress boundary condition on the ASR-induced damage distribution and its reflection on the AE data is investigated. Damage contours based on AE data are developed and utilized to compare event distributions though the medium-scale specimens with different confinements and investigate the temporal evolution of the distributions. Furthermore, the efficacy of differing information entropy calculation

approaches for concrete structures undergoing Alkali-Silica Reaction (ASR) induced damage is investigated.

The results of the studies indicate that confinement affects the distribution of AE events. In the confined specimen, the distribution of AE events in the mid-width region of the specimen is concentrated and has a sharp peak. However, in the unconfined specimen, the distribution of AE events is more uniform, and cracks are randomly distributed.

The entropy results show that the randomness of events increases at the earlier stage of ASR, which is expected due to the microcrack formation and decreases at the later stage due to the formation of macrocracks.

The overall outcome in this dissertation demonstrates the potential of using AE for condition assessment of concrete structures affected by ASR degradation. However, more research is required to standardize the method for the field application.

Table of Contents

Dedication.....	iii
Acknowledgments	iv
Abstract.....	v
List of Tables	xi
List of Figures.....	xii
Chapter 1 Introduction.....	1
1.1 Background.....	2
1.2 Research significance.....	4
1.3 Objectives	5
1.4 Layout of dissertation	8
1.5 References.....	9
Chapter 2 Literature Review	16
2.1 Introduction.....	17
2.2 Damage detection of cementitious material affected by ASR using AE....	18
2.3 Data-driven methods.....	20
2.4 Source location methods.....	24
2.5 Signal processing methods.....	29
2.6 AE-based damage index methods.....	33

2.7 References.....	37
Chapter 3 Evaluation of Damage Propagation in Cement Paste Using Pattern Recognition	46
3.1 Abstract.....	47
3.2 Introduction.....	47
3.3 Materials and experimental test setup.....	51
3.4 Analytical and experimental procedure	54
3.5 Results and discussion	60
3.6 Conclusions.....	75
3.7 References.....	76
Chapter 4 Damage Mechanism Evaluation of Large-scale Concrete Structures Affected by Alkali-silica Reaction Using Pattern Recognition.....	84
4.1 Abstract.....	85
4.2 Introduction.....	85
4.3 Materials and test setup.....	88
4.4 Analysis method.....	94
4.5 Results and Discussions	96
4.6 Conclusions.....	113
4.7 References.....	116
Chapter 5 Temporal Evaluation of ASR Cracking in Concrete Specimens Using Acoustic Emission	122
5.1 Abstract.....	123

5.2 Introduction.....	123
5.3 Test setup and procedure	126
5.4 Analysis procedure.....	131
5.5 Results and discussion	134
5.6 Conclusion	152
5.7 Reference	153
Chapter 6 Investigation of Temporal Evolution of AE Data for Concrete Specimens Affected by ASR Using Information entropy, b-value, Regression analysis, and Gradient of Cumulative Signal Strength.....	162
6.1 Abstract.....	163
6.2 Introduction.....	163
6.3 Test setup	166
6.4 Analysis method and procedure.....	169
6.5 Results.....	175
6.6 Conclusion and summary.....	191
6.7 Acknowledgments.....	193
6.8 References.....	194
Chapter 7 Summary and Conclusion	202
7.1 Summary	203
7.2 Conclusion of each study	206
7.3 Recommendation and future work.....	213

7.4 References.....	215
Appendix A Copyright Permission	217

List of Tables

Table 3.1 Specimens for compression test.....	53
Table 3.2 Average mean square error	68
Table 4.1 Duration-amplitude rejection limits.	100
Table 4.2 Sensor coordinates.	101
Table 5.1 Sensor coordinates.	129
Table 5.2 Data acquisition setting.....	129
Table 5.3 Concrete mixture proportions.	130

List of Figures

Figure 2.1 Clustering approach.....	21
Figure 2.2 Neural network architecture (schematic).....	22
Figure 2.3 Relative frequency histogram for event locations along width of medium-scale specimen.....	23
Figure 2.4 Ray-tracing method	25
Figure 2.5 Damage imaging contours for medium-scale specimens	29
Figure 2.6 Entropy calculation using signal amplitude voltage.....	32
Figure 2.7 FFT Entropy	33
Figure 3.1 Compression test setup and sensor layout	52
Figure 3.2 Bending test setup and sensor layout.....	54
Figure 3.3 Clustering approach.....	56
Figure 3.4 Neural network architecture (schematic).....	57
Figure 3.5 Ray-tracing approach.....	58
Figure 3.6 Visible cracks at conclusion of compression test	61
Figure 3.7 Data from compression testing ¹ Cumulative signal strength. ² Picovolt.second.	62
Figure 3.8 Moment tensor analysis for P-40.....	63
Figure 3.9 Clustering of data.....	64
Figure 3.10 Average feature values for clustered data of compression test. ¹ Cumulative signal strength. ² Picovolt.second.	64

Figure 3.11 Waveform examples for clusters: time history of waves (left), and wavelet energy distributions (right).....	67
Figure 3.12 Neural network error histogram.....	69
Figure 3.13 Cross-correlation figure between output and target matrix	69
Figure 3.14 Average feature values for clustered data of four-point bending test.....	70
Figure 3.15 AE data from four-point bending test.....	71
Figure 3.16 Fracture curves (¹ Cumulative signal strength. ² Picovolt. second).....	72
Figure 3.17 Source location in terms of load level	73
Figure 4.1 Test specimens.....	90
Figure 4.2 Acoustic emission (AE) sensor locations. (a) Internal AE sensors (broadband); (b) External AE sensors (resonant); (c) Internal sensors 3 and 6 installation; (d) Internal sensors 1, 2, 4 and 5 installation.	91
Figure 4.3 Clustering procedure. (a) Energy-frequency based feature extraction; (b) Flow chart of data clustering steps.	96
Figure 4.4 Strain distribution of specimens versus concrete age. (a) Directional expansion; (b) Volumetric strain.	97
Figure 4.5 Amplitude and cumulative signal strength of AE data in terms of concrete age. (a) Confined specimen; (b) Unconfined specimen; (c) Control specimen.	100
Figure 4.6 Cumulative signal strength (CSS) contribution for sensors. (a) CSS vs. age of concrete for confined specimen; (b) CSS vs. age of concrete for unconfined specimen; (c) Normalized CSS for confined specimen; (d) Normalized CSS for unconfined specimen.	102
Figure 4.7 Clustering dendrograms. (a) Confined specimen; (b) Unconfined specimen.	104
Figure 4.8 Clusters in principle component dimensions. (a) Confined specimen; (b) Unconfined specimen.	105
Figure 4.9 Average normalized signal energy in frequency domain. (a) Confined specimen; (b) Unconfined specimen.	105

Figure 4.10 Normalized signal features. (a) Confined specimen; (b) Unconfined specimen.	107
Figure 4.11 Normalized cumulative signal strength. (a) Confined specimen; (b) Unconfined specimen.	109
Figure 4.12 Distribution of total AE signal strength in terms of clusters and sensors. (a) Confined specimen at age of 66 days; (b) Unconfined specimen at age of 66 days; (c) Confined specimen at age of 150 days; (d) Unconfined specimen at age of 150 days; (e) Confined specimen at age of 195 days; (f) Unconfined specimen at age of 195 days.	111
Figure 5.1 Specimen sensor layouts and structural details.	128
Figure 5.2 Measured strains using DEMEC gauge.	135
Figure 5.3 Filtered AE data in terms of amplitude and cumulative signal strength versus time.	136
Figure 5.4 Linking dendrograms.	137
Figure 5.5 Data presentation in principle component space.	138
Figure 5.6 Energy-frequency distributions of clusters.	138
Figure 5.7 Normalized parametric features.	139
Figure 5.8 Cumulative signal strength for clustered data.	140
Figure 5.9 Percentage of signals in clusters in terms of time.	141
Figure 5.10 Source localization contours in the X-Y plane (top view).	143
Figure 5.11 AE event distributions in Y direction at 300 days.	144
Figure 5.12 AE event distribution parameters along Y axis versus experiment time.	146
Figure 5.13 Source location contours in X-Z plane.	147
Figure 5.14 AE event distributions in Z direction at 300 days.	148
Figure 5.15 AE event distribution parameters along Z axis versus experiment time.	149
Figure 5.16 Maximum crack width measurement.	151
Figure 5.17 Crack quantification on top surface in terms of time.	151

Figure 6.1 Entropy calculation using signal amplitude voltage.....	170
Figure 6.2 FFT Entropy	171
Figure 6.3 Discrete voltage entropy (DVE) for medium-scale specimens, bin size: 0.0001 volts	175
Figure 6.4 Discrete voltage entropy for medium-scale specimens using different bin sizes	176
Figure 6.5 Global voltage entropy (GVE) for medium-scale specimens.....	177
Figure 6.6 Counts entropy (CE) for medium-scaled specimens.	178
Figure 6.7 Counts entropy using CDF (CE_CDF) for medium-scale specimens.....	179
Figure 6.8 FFT entropy for medium-scale specimens	179
Figure 6.9 Discrete voltage entropy (DVE) and cumulative entropy for small-scale specimens	180
Figure 6.10 Discrete voltage entropy and cumulative entropy for medium-scale specimens	182
Figure 6.11 Discrete voltage entropy and cumulative entropy for large-scale specimens	183
Figure 6.12 Probability distribution functions of signal strength and entropy.	183
Figure 6.13 Historic index for medium-scale specimens.....	186
Figure 6.14 Probability density function of AE hits in time for the medium-scale specimens	186
Figure 6.15 Intensity analysis graph for medium-scale specimens.....	188
Figure 6.16 CSS gradients for medium-scale specimens.....	189
Figure 6.17 Incremental b values and coefficients of determination of amplitude distribution for medium-scale specimens.....	190
Figure 6.18 Incremental improved b values and coefficients of determination of amplitude distribution for medium-scale specimens.....	191

Chapter 1

Introduction

1.1 Background

Alkali-silica reaction (ASR) is a chemical reaction that has caused damage in concrete structures such as bridges [1-4], nuclear power plants [5-9], and concrete dams [5,10]. This reaction usually occurs between alkali hydroxides in the pore solution and the reactive silica in some aggregates. The result is an alkali-silica gel, which is hygroscopic and imbibes water and humidity. The gel expands in humidity to a point exceeding 80% [6]. This expansion induces pressure on the concrete matrix and aggregates and causes microcracks and cracks when the pressure exceeds the tensile strength of concrete [11,12]. Several traditional methods such as visual inspection, coring, petrographic analysis, demountable mechanical strain gauges (DEMEC), relative humidity or moisture content measurement, and crack indexing have been utilized for monitoring and identifying the damage caused by ASR [13]. Despite the simplicity of these methods, they have some drawbacks. For instance, visual inspection is not efficient for the early detection of ASR damage since ASR damage initiates internally in concrete structures and then extends to the surfaces. This disadvantage is more critical in thick shear walls (e.g., nuclear structures), where most of the expansion happens out-of-plane due to in-plane confinement and the damage on the surface appears in later stages of the ASR reaction. Furthermore, visual inspection is time-consuming and often operator-dependent, especially for large-scale structures, although advances in drone inspection and image analysis could improve visual inspection [14-16]. Crack indexing is also time-consuming and not easily applied for evaluating very large and complex structures. Although DEMEC gauges are generally useful for some structural components such as piles and columns, it is not a well-suited index for studying damage in shear walls, because it measures expansion on the surface

rather than through the thickness. Petrography is helpful for ASR damage quantification using a damage rating index, but it is time-consuming and intrusive. In addition, the method is focused on microscale damage in the concrete and diagnosing the cause(s) of distress, but it is difficult to generalize petrographic results for the structural capacity. Coring is also a destructive method, and large numbers of cores are impractical for potentially sensitive structures such as nuclear containments.

Nondestructive methods [17,18] are alternatives for damage quantification and for the condition assessment of structures affected by ASR. Several methods have been employed for this purpose such as digital image correlation [19], nonlinear Rayleigh surface ultrasonic [20,21], ultrasonic pulse velocity [22], dynamic modulus of elasticity [23], impact-echo [17], and acoustic emission (AE) [21,24-26]. Acoustic emission is a passive structural health monitoring approach which has recently been utilized for detection of damage in concrete elements [21,24-27]. This method uses piezoelectric sensors to respond to elastic stress waves emitted by the crack formation and records the stress waves as digital signals, usually amplified through external or integral preamplifiers. The sensors are very sensitive and can capture internal microscale damage development. Furthermore, AE can monitor structural condition continuously without disrupting the use of the structure, damage localization is feasible [28-30]; and the method is applicable when only one side of the structure is accessible.

The AE technology has been utilized in several applications such as monitoring damage progression induced by corrosion [31-33], pipe leakage detection [34,35], and bridge damage evaluation [36-43]. In spite of the vast application of AE in damage assessment of structures, a limited number of research on AE application in damage

identification and assessment of concrete structures affected by ASR have been published [11,21,24,44]. The published papers regarding ASR and AE were focused on small-scale specimens without considering the effect of stress boundary condition on ASR induced damage and AE data.

1.2 Research significance

ASR is one of the damage sources in concrete structures and infrastructures that may endanger the integrity and serviceability of structures. The conventional methods for monitoring and tracing damage and ASR are subjective, destructive, and sometimes inefficient. Therefore, a need for a health monitoring method, which is sensitive, efficient, and nondestructive to detect ASR induced damage and monitor damage progression is incontrovertible. AE can be an alternative for the condition assessment of structures affected by ASR. This method can be employed independently or as a sector of a comprehensive health monitoring system. However, there are several challenges, and scientific gaps exist in a path toward developing an AE-based condition assessment for ASR induced damage, some of which are addressed in this dissertation. One of the scientific gaps is the lack of knowledge about the damage distribution of concrete structures affected by ASR and the reflection of damage in the temporal evaluation of AE data, which was addressed in this dissertation.

The effect of the stress boundary condition on ASR damage is of significance since ASR expansion and damage are developed in a direction with less confinement. Therefore, damage conditions and the effect of stress boundary condition on the damage distribution of medium-scale and large-scale specimens are investigated in this dissertation. Furthermore, the reflection of damage anisotropy in AE data is also studied.

Damage imaging contours based on AE data are derived to study temporal ASR damage progression. The images are generated by using the minimum sensors required for source localization.

In addition, the efficiency of Shannon entropy, intensity analysis, and b-value for AE data recorded during the ASR process is investigated. Shannon entropy is utilized as a parameter to study the temporal damage evolution of concrete specimens affected by ASR. The entropies are calculated for different specimen scales (large-scale, small-scale, and medium-scale) specimens according to the committee's recommendation.

1.3 Objectives

The primary objective of this study is to use acoustic emission for condition assessment of reinforced concrete structures, which have deteriorated due to ASR. To achieve this goal, data-driven methods, in combination with signal processing techniques, will be employed to find a potential temporal trend in the AE data.

Therefore, four different studies are defined to approach the primary goal. Each research topic has its own specific set of objectives.

1.3.1 Evaluation of damage propagation in cement paste using pattern recognition

Since damage in cementitious materials is related to crack formation, data-driven methods such as unsupervised pattern recognition and artificial neural networks have been utilized to identify the signal signatures associated with microcrack and macrocrack formation mechanisms. The main objectives of this study are as follows:

- Cluster the AE data from compression tests that are based on frequency content and relate them to the AE data derived during a four-point bending test using a neural network.

- Localize the events in the beam and assign them to the potential crack mechanisms based on event location, frequency, and non-frequency dependent signal features, and time of occurrence.
- Evaluate the efficiency of data-driven methods for recognizing crack formation mechanisms in cement paste.

1.3.2 Damage mechanism evaluation of large-scale concrete structures affected by Alkali-Silica Reaction using acoustic emission

Alkali-silica is a chemical reaction which has caused volumetric expansion and consequential damage to concrete structures such as bridges, nuclear power plants, and nuclear waste containments. The volumetric strain of structure components depends directly on stress boundary conditions. The primary objectives of this research are as follows:

- Study the influence of plane confinement on damage distribution in large-scale concrete structures by using acoustic emission.
- Cluster the AE data based on energy-frequency features and observe the potential temporal trend in the data.
- Evaluate cumulative AE signal strength in terms of sensor location to study the correlation between AE data and strain.

1.3.3 Temporal Evaluation of ASR Damage in Concrete Specimens with a Data-driven Approach

In this study, medium-scale concrete specimens were exposed to a high temperature and humidity for accelerated aging. A larger number of sensors corresponding to the volume of concrete were mounted on the medium-scale specimens than large-scale

specimens. The larger number of sensors provide feasibility to elaborately study the ASR process and damage distribution. The primary objectives of this research are as follows:

- Deriving ASR damage contours based on AE data by using minimum sensors required for source localization.
- Studying damage anisotropy caused by steel reinforcements by using data-driven method and AE data.
- Evaluating temporal evolution in signal frequency for studying ASR damage progression using unsupervised pattern recognition.

1.3.4 Investigation of Temporal Evolution of AE Data for Concrete Specimens Affected by ASR Using Information entropy, b-value, Regression analysis, and Gradient of Cumulative Signal Strength

In this study, the efficiency of information entropies with different calculation methods, intensity analysis, and b-value analysis is evaluated for the concrete structures affected by ASR. In addition, the voltage entropy is calculated for the AE data acquired for the specimens with different scales and boundary conditions according to the committee's recommendation. The applicability of intensity analysis and b-value analysis is studied for AE data collected during the ASR process. Regression coefficients are employed for damage identification during ASR. The primary objectives of this research are as follows:

- Comparing and investigating the results of different information entropies for the AE data recorded during the ASR process.
- Studying the effect of specimen dimensions and stress boundary conditions on voltage information entropy values.

- Studying the results of intensity analysis, b-value analysis, and regression coefficients for the AE data collected during the ASR process.

1.4 Layout of dissertation

The dissertation has seven chapters. Chapter 2 is entitled “Literature review” and it includes background information from previously published literature including application of AE for ASR monitoring, AE-based damage indices, source localization and damage imaging methods, data-driven methods, and signal processing techniques.

Chapters 3 through 6 were prepared in paper format, which includes published papers, submitted papers, and papers which are planned to be submitted. Therefore, some basic explanations may be repeated.

Chapter 3 is titled “Evaluation of damage propagation in cement paste using pattern recognition”, where damage mechanisms of a cement paste under a compressive load was related to damage mechanisms of a cement paste under four-point bending using unsupervised pattern recognition, ray-tracing method and a neural network. The methods in this study have been used in later studies, which are focused on ASR damage.

Chapter 4 is titled “Damage mechanism evaluation of large-scale concrete structures affected by Alkali-Silica Reaction using acoustic emission”. In this study, AE sensors were used for condition assessment of large-scale specimens, which were retained in a chamber with high temperature and humidity.

Chapter 5 is titled “Investigation of Temporal Evolution of AE Data for Concrete Specimens Affected by ASR Using Information entropy, b-value, Regression analysis, and Gradient of Cumulative Signal Strength”. In this study, AE sensors were installed on the surfaces of medium-scale specimens. A larger number of AE sensors gave an opportunity

to study the effect of boundary conditions on the ASR damage distribution and temporal ASR damage progression more elaborately.

Chapter 6 is titled “Information entropy, b-value, and intensity analysis for concrete specimens affected by ASR”. In this study, information entropies using different methods were calculated for the AE recorded during the ASR process, and the efficiency of methods and the temporal evolution of entropy were investigated. In addition, the applicability of intensity analysis and b-value analysis were studied for ASR damage monitoring.

Chapter 7 includes a dissertation summary, research conclusions, and recommendations for future research.

1.5 References

1. Schmidt, J.W.; Hansen, S.G.; Barbosa, R.A.; Henriksen, A. Novel shear capacity testing of asr damaged full scale concrete bridge. *Engineering Structures* **2014**, *79*, 365-374.
2. Clark, L. *Critical review of the structural implications of the alkali silica reaction in concrete*. Bridges Design, Structures Group, Transportation and Road Research Laboratory: 1989.
3. Bach, F.; Thorsen, T.S.; Nielsen, M. Load-carrying capacity of structural members subjected to alkali-silica reactions. *Construction and Building Materials* **1993**, *7*, 109-115.
4. Bakker, J. In *Control of asr related risks in the netherlands*, Proceedings of the 13th International Conference on Alkali-Aggregate Reaction in Concrete, 2008; Tondheim:[sn]: pp 21-31.

5. Charlwood, R.; Solymar, S.; Curtis, D. In *A review of alkali aggregate reactions in hydroelectric plants and dams*, Proceedings of the international conference of alkali-aggregate reactions in hydroelectric plants and dams, 1992.
6. Saouma, V.E.; Hariri-Ardebili, M.A. A proposed aging management program for alkali silica reactions in a nuclear power plant. *Nuclear Engineering and Design* **2014**, 277, 248-264.
7. Takakura, T.; Ishikawa, T.; Mitsuki, S.; Matsumoto, N.; Takiguchi, K.; Masuda, Y.; Nishiguchi, I. In *Investigation on the expansion value of turbine generator foundation affected by alkali-silica reaction*, Proceedings of 18th International Conference on Structural Mechanics in Reactor Technology, 2005.
8. Takakura, T.; Masuda, H.; Murazumi, Y.; Takiguchi, K.; Masuda, Y.; Nishiguchi, I. Structural soundness for turbine-generator foundation affected by alkali-silica reaction and its maintenance plans. **2007**.
9. Tchernier, J.; Aziz, T. In *Effects of aar on seismic assessment of nuclear power plants for life extensions*, Proceedings SMiRT, 2009; pp 1-8.
10. Charlwood, R. In *Predicting the long term behaviour and service life of concrete dams*, Long Term Behaviour of Dams, LTBD09, Graz, Austria, 2009; Graz, Austria.
11. Abdelrahman, M.; ElBatanouny, M.K.; Ziehl, P.; Fasl, J.; Larosche, C.J.; Fraczek, J. Classification of alkali-silica reaction damage using acoustic emission: A proof-of-concept study. *Construction and Building Materials* **2015**, 95, 406-413.
12. Garcia-Diaz, E.; Riche, J.; Bulteel, D.; Vernet, C. Mechanism of damage for the alkali-silica reaction. *Cement and Concrete Research* **2006**, 36, 395-400.

13. Thomas, M.D.; Folliard, K.J.; Fournier, B.; Rivard, P.; Drimalas, T.; Garber, S.I. *Methods for evaluating and treating asr-affected structures: Results of field application and demonstration projects—volume ii: Details of field applications and analysis*; 2013.
14. Seo, J.; Wacker, J.P.; Duque, L. *Evaluating the use of drones for timber bridge inspection*; General Technical Report FPL-GTR-258; Department of Agriculture, Forest Service, Forest Products Laboratory: Madison, WI, U.S., 2018; pp 1-152.
15. Zink, J.; Lovelace, B. *Unmanned aerial vehicle bridge inspection demonstration project*; MN/RC 2015-40; Minnesota Department of Transportation, Office of Transportation System Management: 2015.
16. Yang, C.-H.; Wen, M.-C.; Chen, Y.-C.; Kang, S.-C. In *An optimized unmanned aerial system for bridge inspection*, ISARC. Proceedings of the International Symposium on Automation and Robotics in Construction, 2015; IAARC Publications: p 1.
17. Giannini, E.R.; Folliard, K.J.; Zhu, J.; Bayrak, O.; Kreitman, K.; Webb, Z.; Hanson, B. *Non-destructive evaluation of in-service concrete structures affected by alkali-silica reaction (asr) or delayed ettringite formation (def)—final report, part i*; 2013.
18. Mahadevan, S.; Agarwal, V.; Neal, K.; Nath, P.; Bao, Y.; Cai, G.; Orme, P.; Adams, D.; Kosson, D. *A demonstration of concrete structural health monitoring framework for degradation due to alkali-silica reaction*; Idaho National Lab.(INL), Idaho Falls, ID (United States): 2016.

19. Teramoto, A.; Watanabe, M.; Murakami, R.; Ohkubo, T. Visualization of internal crack growth due to alkali-silica reaction using digital image correlation. *Construction Building Materials* **2018**, *190*, 851-860.
20. Kim, G.; Park, S.; Kim, J.-Y.; Kurtis, K.E.; Hayes, N.W.; Jacobs, L.J. Nonlinear rayleigh surface waves to characterize microscale damage due to alkali-silica reaction (asr) in full-scale, nuclear concrete specimens. *Construction Building Materials* **2018**, *186*, 1114-1118.
21. Lokajíček, T.; Přikryl, R.; Šachlová, Š.; Kuchařová, A. Acoustic emission monitoring of crack formation during alkali silica reactivity accelerated mortar bar test. *Engineering geology* **2017**, *220*, 175-182.
22. Rivard, P.; Saint-Pierre, F. Assessing alkali-silica reaction damage to concrete with non-destructive methods: From the lab to the field. *Construction Building Materials* **2009**, *23*, 902-909.
23. Sargolzahi, M.; Kodjo, S.A.; Rivard, P.; Rhazi, J. Effectiveness of nondestructive testing for the evaluation of alkali-silica reaction in concrete. *Construction Building Materials* **2010**, *24*, 1398-1403.
24. Farnam, Y.; Geiker, M.R.; Bentz, D.; Weiss, J. Acoustic emission waveform characterization of crack origin and mode in fractured and asr damaged concrete. *Cement and Concrete Composites* **2015**, *60*, 135-145.
25. Abdelrahman, M.; ElBatanouny, M.K.; Ziehl, P.; Fasl, J.; Larosche, C.J.; Fraczek, J. Classification of alkali-silica reaction damage using acoustic emission: A proof-of-concept study. *Construction Building Materials* **2015**, *95*, 406-413.

26. Weise, F.; Voland, K.; Pirskawetz, S.; Meinel, D. In *Innovative measurement techniques for characterising internal damage processes in concrete due to asr*, Proceedings of the International Conference on Alkali Aggregate Reaction (ICAAR), University of Texas, Austin, TX, USA, 2012; pp 20-25.
27. Soltangharaei, V.; Anay, R.; Hayes, N.; Assi, L.; Le Pape, Y.; Ma, Z.; Ziehl, P. Damage mechanism evaluation of large-scale concrete structures affected by alkali-silica reaction using acoustic emission. *Applied Sciences* **2018**, *8*, 2148.
28. Shiotani, T.; Osawa, S.; Kobayashi, Y.; Momoki, S. Application of 3d ae tomography for triaxial tests of rocky specimens. In *Proceedings of the European Working Group on Acoustic Emission*, Dresden, Germany, 2014; pp 3-5.
29. Shiotani, T.; Nishida, T.; Nakayama, H.; Asaue, H.; Chang, K.-C.; Miyagawa, T.; Kobayashi, Y. Fatigue failure evaluation of rc bridge deck in wheel loading test by ae tomography. In *Advances in acoustic emission technology*, Springer: 2017; pp 251-264.
30. ElBatanouny, M.K.; Ziehl, P.H.; Larosche, A.; Mangual, J.; Matta, F.; Nanni, A. Acoustic emission monitoring for assessment of prestressed concrete beams. *Construction Building Materials* **2014**, *58*, 46-53.
31. Patil, S.; Karkare, B.; Goyal, S. Corrosion induced damage detection of in-service rc slabs using acoustic emission technique. *Construction and Building Materials* **2017**, *156*, 123-130.
32. Elfergani, H.A.; Pullin, R.; Holford, K.M. Damage assessment of corrosion in prestressed concrete by acoustic emission. *Construction and Building Materials* **2013**, *40*, 925-933.

33. Ziehl, P.; ElBatanouny, M. Acoustic emission monitoring for corrosion damage detection and classification. In *Corrosion of steel in concrete structures*, Elsevier: 2016; pp 193-209.
34. Anastasopoulos, A.; Kourousis, D.; Bollas, K. Acoustic emission leak detection of liquid filled buried pipeline. *Journal of Acoustic Emission* **2009**, *27*.
35. Mostafapour, A.; Davoudi, S. Analysis of leakage in high pressure pipe using acoustic emission method. *Applied Acoustics* **2013**, *74*, 335-342.
36. ElBatanouny, M.K.; Ziehl, P.H.; Larosche, A.; Mangual, J.; Matta, F.; Nanni, A. Acoustic emission monitoring for assessment of prestressed concrete beams. *Construction and Building Materials* **2014**, *58*, 46-53.
37. Yu, J.; Ziehl, P.; Zárate, B.; Caicedo, J. Prediction of fatigue crack growth in steel bridge components using acoustic emission. *Journal of Constructional Steel Research* **2011**, *67*, 1254-1260.
38. Abdelrahman, M.; ElBatanouny, M.K.; Ziehl, P.H. Acoustic emission based damage assessment method for prestressed concrete structures: Modified index of damage. *Engineering Structures* **2014**, *60*, 258-264.
39. Nair, A.; Cai, C. Acoustic emission monitoring of bridges: Review and case studies. *Engineering Structures* **2010**, *32*, 1704-1714.
40. Noorsuhada, M. An overview on fatigue damage assessment of reinforced concrete structures with the aid of acoustic emission technique. *Construction Building Materials* **2016**, *112*, 424-439.

41. Behnia, A.; Chai, H.K.; Ranjbar, N.; Jumaat, M.Z. Damage detection of sfrc concrete beams subjected to pure torsion by integrating acoustic emission and weibull damage function. *Structural Control Health Monitoring* **2016**, *23*, 51-68.
42. Golaski, L.; Gebski, P.; Ono, K. Diagnostics of reinforced concrete bridges by acoustic emission. *Journal of acoustic emission* **2002**, *20*, 83-89.
43. Zaki, A.; Chai, H.K.; Behnia, A.; Aggelis, D.G.; Tan, J.Y.; Ibrahim, Z. Monitoring fracture of steel corroded reinforced concrete members under flexure by acoustic emission technique. *Construction building materials* **2017**, *136*, 609-618.
44. Weise, F. Innovative measurement techniques for characterising internal damage processes in concrete due to asr. **2012**.

Chapter 2

Literature Review

2.1 Introduction

Acoustic emission (AE) is one of the health monitoring methods which has been utilized for damage detection and the condition assessment of structures [1-5]. Generally, AE is referred to as a phenomenon where elastic waves are emitted due to sudden energy release caused by a defect and crack formation in a material [6]. The waves travel through a specimen and reach to surfaces and sensors. The AE sensors are commonly piezoelectric sensors. They are excited by surface vibrations and they transfer mechanical stress waves to voltages, and the voltages are digitized through a data acquisition system. The AE piezoelectric sensors are very sensitive and can detect even small-scale cracks inside structures. The method is passive, and there is no need for the excitation of structures. In addition, it can continuously monitor structures without halting structure serviceability. The method is non-destructive, which can be employed in situations where the destructive methods are forbidden such as nuclear facilities or prestressed bridges. The damage location can be identified if an appropriate sensor layout is defined.

AE has been utilized in several applications such as detecting corrosion-induced damage [7-17], pipe leakage detection [18-20], bridge and beam damage evaluation [7,21-26], and damage caused by alkali-silica reaction (ASR) [3,4,27-29].

The focus of this study is the condition assessment of concrete structures affected by ASR. Several conventional methods have been employed for this purpose such as visual inspection, coring, petrographic analysis, demountable mechanical strain gauges (DEMEC), relative humidity or moisture content measurement, and cracking index [30]. These methods are not always efficient and have some limitations and drawbacks. For example, visual inspection is not efficient for early detection of damage since ASR

damage initiates internally in concrete structures and then extends to surfaces. This problem is more critical in thick shear walls (e.g., nuclear structures), where most of the expansion occurs out-of-plane due to in-plane confinement and damage on the surface appears in the latter stages of ASR reaction.

Furthermore, visual inspection is time-consuming and often operator-dependent, especially for large-scale structures, although advances in drone inspection and image analysis could improve visual inspection [31-33]. Crack indexing is also time-consuming and not easily applied for evaluating very large and complex structures. This method is usually focused on a limited region of structures, and it is difficult to generalize the cracking index to the condition of entire structures. Although DEMEC gauges are generally useful for some structural components such as piles and columns, it is not a well-suited index for studying damage in shear walls, because it measures expansion on surfaces rather than through the thickness. Petrography is helpful for ASR damage quantification using a damage rating index, but it is time-consuming and intrusive. In addition, the method is focused on microscale damage in the concrete and diagnosing the cause(s) of distress, but it is difficult to generalize petrographic results for the structural capacity. Coring is also a destructive method, and large numbers of cores are impractical for potentially sensitive structures such as nuclear containments.

2.2 Damage detection of cementitious material affected by ASR using AE

To date, there is few published literature regarding AE as a structural health monitoring technique for ASR degradation. AE has mainly been employed for small-scale concrete specimens affected by ASR without steel reinforcement. Abdelrahman et al. [27] utilized AE for monitoring ASR in ASTM standard concrete prisms. Petrography

was conducted for the six specimens with three different ages (two specimens for each age). A damage rating index (DRI) was used to quantify the degradation damage using petrography. The authors found a correlation between AE activity and expansion from ASR measured per ASTM C1293. They concluded that the rate of ASR degradation can be related to the rate of AE activity. In addition, AE results were correlated to petrography DIR through the intensity analysis.

Farnam et al. [4] used mortar cylinders with a diameter and a height of 20 mm and 40 mm. A single broadband AE sensor was attached to each specimen. AE was used to identify the frequency of signals emitted from cement paste, aggregate, and interfacial transition zone (ITZ). At first, the frequency ranges were determined by analyzing data collected during wedge splitting tests on four different specimens of granite rocks, hydrated cement paste, composite samples which contained a granite rock and cement paste, and mortar samples. It was concluded that aggregate cracking caused higher frequency AE signals than the crack formation in cement paste and ITZ. The AE frequency range for aggregate was 300-400 kHz, while the frequency range for cement matrix was 100-300 kHz. The authors monitored the ASR progress for the small-scale specimens using AE. They have observed that at the earlier stage of ASR (up to 21 days), most of AE hits had a frequency range of 300 to 400 kHz, however, in the later stage (e.g. after 43 days), most of AE hits possessed a frequency range of less than 150 kHz. Comparing the results of ASR and the wedge test, they concluded that cracking started to appear at aggregates and then propagated inside the cement matrix.

Lokajčėk et al. [3] employed both ultrasonic pulse velocity and AE to monitor ASR reaction in the ASTM standard mortar prisms. The prisms had different aggregates

and reactivities. Ultrasonic sounding results correlated with the expansion and reactivity of specimens. The larger was the ASR expansion, the earlier decrease in P-wave velocity was observed. In addition, the authors found a correlation between AE cumulative energy and the reactivity of the specimens. They concluded that AE emission due to ASR damage depended not only on brittle damage characteristics but also on the ASR gel formation. Moreover, the ASR gel and decrease in sensor coupling due to expansion could be reasons the AE amplitudes reduced at the later ASR stages.

2.3 Data-driven methods

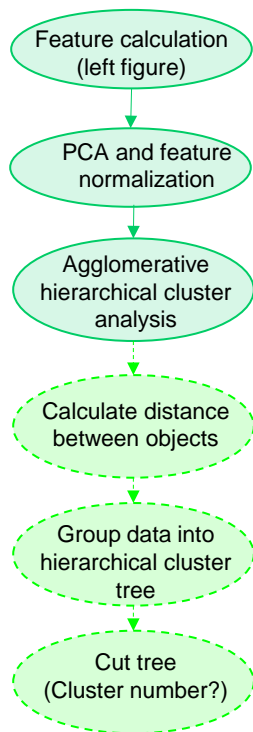
In this dissertation, data-driven methods, such as unsupervised pattern recognition and neural network have been employed.

2.3.1 Unsupervised pattern recognition

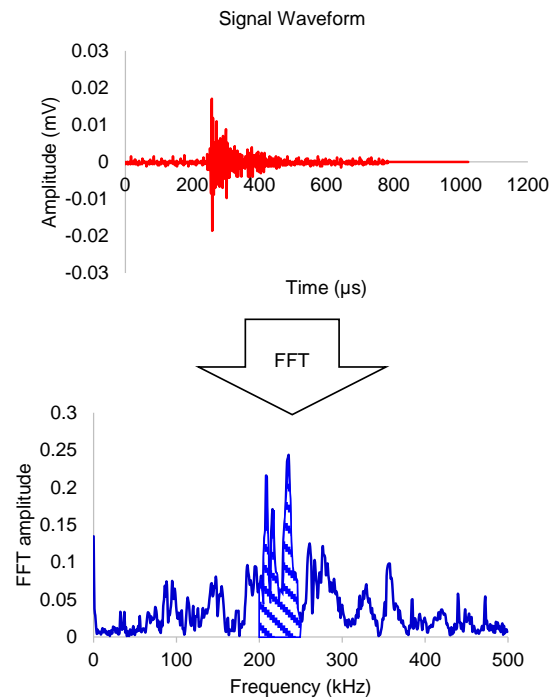
Unsupervised pattern recognition is a data-driven method which is used to discriminate unlabeled multidimensional data into clusters. The data in each cluster share similar characteristics [34].

An agglomerative hierarchical clustering method is utilized for clustering the AE signals based on their frequency content. Each input data is initially assumed to be a cluster. Then, based on a calculated proximity matrix (similarity and dissimilarity), the initial clusters are grouped to form a new cluster. The proximity matrix is updated at each merging level. This procedure is repeated for the new clusters and terminated with one final cluster. After forming a dendrogram for all data, the required number of clusters is determined based on the height of each link in a cluster to the neighboring links [35]. The procedure is shown in Figure 2.1. In this study, Euclidean distance and Ward's method are utilized for finding distances and to linkage of data, respectively [36].

The derived features are based on the frequency contents of signals. The AE signals are transferred to the frequency domain using the Fast Fourier Transform (FFT). Then, the Fourier magnitudes are calculated in terms of frequency. The frequency domain is divided into ten equal frequency bands, and the area under each band is normalized by the total area of the FFT spectrum. The resulted values are utilized as the clustering features (Figure 2.1a and b). Principle Component Analysis (PCA) is used to reduce the dimension of the input matrix. In PCA, the original data is projected to the new orthogonal coordinates with the high variation.



(a) Clustering algorithm



(b) Signal feature calculation

Figure 2.1 Clustering approach

2.3.2 Artificial neural network

Artificial neural network (ANN) is a supervised pattern recognition method, which can be utilized when a labeled dataset and history of data are available. ANNs have three primary layers: input, hidden, and output. In the input layer, the data matrix and the target matrix are defined. The data matrix includes all observations with their associated features, and the target matrix includes data labels. The algorithm trains a network to reach the target matrix, and results are presented as an output matrix. The most significant layer in ANN is the hidden layer, where an ANN learns the relationship between the input data and the target layer [37,38]. The schematic architecture of a trained neural network is presented in Figure 2.2. The network includes one hidden layer with 25 neurons. The data matrix is separated into three data sets; training, validation, and test data. The training data set is utilized for training the network. The validation data is usually selected from the input data to evaluate the network during the training process. This data is utilized to help a network to be generalized for a new dataset. The testing data is an independent dataset to test the performance of the trained network [39].

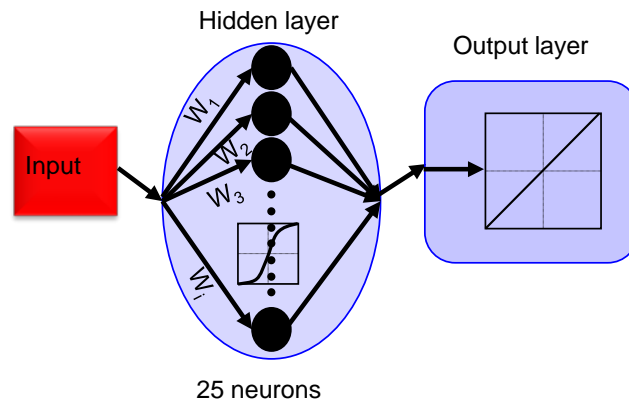


Figure 2.2 Neural network architecture (schematic)

2.3.3 Statistical analysis and distribution

In this dissertation, statistical distributions are utilized for AE feature analyses. The first distribution is a normalized histogram of events (relative frequency histogram), which has been utilized in the medium-scale specimens. The relative frequency histogram is a bar graph, which illustrates how often a variable occurs within a specific variable value range. The range widths are referred to bin size [40]. Examples of histograms for event locations are presented in Figure 2.3. The vertical solid red line is the median of events, which separates the lowest 50% and the highest 50% of data [40]. The first and third quartiles separate the lowest 25% of the data from the highest 75%, and the highest 25% of data from the lowest 75%, respectively. The difference between 3rd quartile and 1st quartile is called “interquartile range”. In this dissertation, the interquartile ranges were normalized to the corresponding specimen dimension.

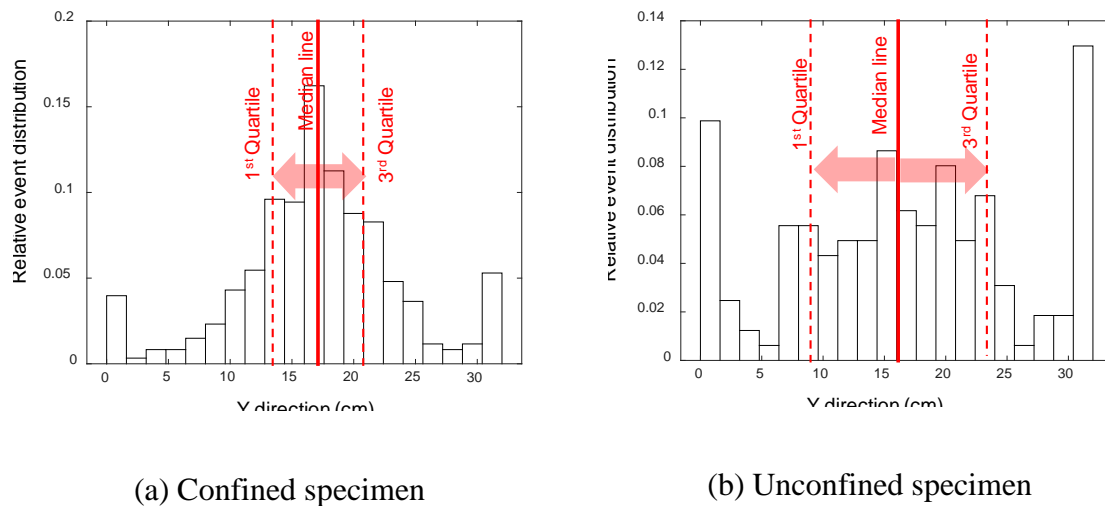


Figure 2.3 Relative frequency histogram for event locations along width of medium-scale specimen

The vertical axis of the figure is the relative frequency of events. For example, in Figure 2.3a, the value for the first bin from the left is approximately equal to 0.04, which

means only 4% of data is between 0 to 1.6 cm. In other words, the probability of event occurrence between 0 to 1.6 cm is 4%.

The relative frequency histogram was also employed for calculating the Shannon entropy (information entropy). This is going to be explained in the entropy section.

Another distribution, which is used in this dissertation, is kernel distribution. The kernel density estimator is calculated by the following equation [41,42]:

$$\hat{f}_h(x) = \frac{1}{nh} \sum_{i=1}^n K\left(\frac{x-x_i}{h}\right) \quad (2.1)$$

Where n is the number of samples, h is scaled kernel, and K is a kernel function.

Nonparametric kernel distribution was used to derive the distribution of ASR data in terms of time and also the distribution of features.

2.4 Source location methods

In this dissertation, two methods were used for source localization; ray-tracing method and damage imaging based on iterative source localization. Both methods are based on the time of arrival of signals.

2.4.1 Ray-tracing source location

A MATLAB script was developed for source location of AE events based on the ray-tracing concept [43]. The algorithm and an example of the results are shown in Figure 2.4.

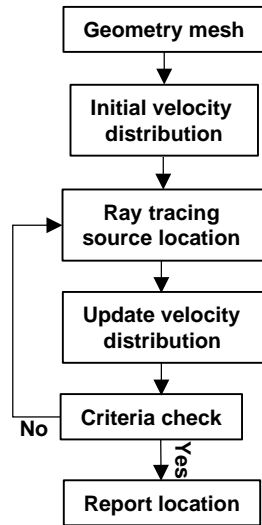
The first step is meshing a specimen. An example of meshing and source location using ray-tracing is shown in Figure 2.4b. In the figure, mesh lengths of 15.2 mm (0.6 inches), and 3.81 mm (0.15 inches) were employed along the long and short dimensions of a beam (152 mm and 38.1 mm), respectively. The velocity distribution is initially assumed to be constant within the resulting cells.

Possible emission times of all nodes (intersection of meshes) for the detected sensors based on the observed arrival times are calculated. Details of the procedure are explained by Shiotani et al. [44].

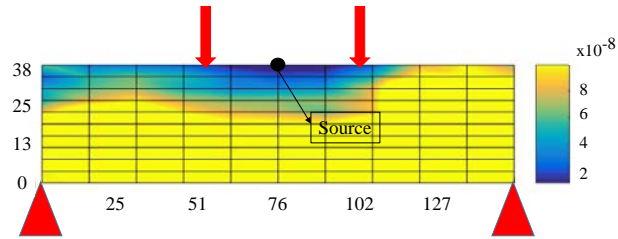
$$E_{ij} = T_i - t_{ij} \quad (2.2)$$

Where E_{ij} is a possible emission time between node j and sensor i . t_{ij} is travel time between node j and sensor i , and T_i is an observed arrival time at sensor i .

The average and variance of the calculated possible emission times for all nodes are calculated by the following equations:



(a) Algorithm



(b) Source location result (dimensions in mm)

Figure 2.4 Ray-tracing method

$$\sigma_j = \frac{\sum_{i=1}^N (E_{ij} - m_j)^2}{N} \quad (2.3)$$

$$m_j = \frac{\sum_{i=1}^N E_{ij}}{N} \quad (2.4)$$

In the above equations, N is the total number of sensors which detect an event. The nodes with the minimum variance are expected to be nearby the real event location. Therefore, a geometrical average of the coordinates for the nodes with the lowest variances is reported as the source location. The associated average possible emission time is assumed to be an event emission time.

A residual slowness in each cell is calculated based on the difference between the observed and estimated travel times. Finally, the slowness or velocity matrix is updated by redistribution of the weighted average residual cell slowness [43,45]. Figure 2.4b shows an example of a source location for one AE event in the four-point bending test. The contour shows the uncertainty in calculating the travel times of the nodes. The lowest uncertainty values present the region with the highest probability of event location.

2.4.2 Time of arrival picker algorithm

One of the methods for source locations of AE data is the arrival time approach [46]. This method is based on the TOAs of signals registered in each sensor and solving a nonlinear equation of velocity versus distance. Therefore, estimating a realistic TOA for signals has a direct effect on the source location precision. The commercial AE data acquisitions have two options for estimating TOAs (peak timing and first time crossing), which are based on peak time and threshold [47]. These methods commonly do not show realistic TOAs, especially when the source is far away from the sensors, due to wave dispersion and attenuation. Errors related to TOAs are getting worse, especially in heterogeneous materials such as concrete compared to homogeneous materials. Therefore, in this study, the Akaike Information Criterion (AIC) was utilized for estimating the TOAs. This method has shown good results in previous researches on

concrete [10,48-50]. In this method, a window is defined at the beginning of signals to include the region of the expected signal initiation. In this dissertation, the first 356 μs of each signal is considered for TOA calculation. For the windowed signals, the AICs are calculated according to the following equation [48,51]:

$$AIC(t_w) = t_w \log \left(\sigma^2(S(1:t_w)) \right) + (n_w - k_w) \log \left(\sigma^2((1 + t_w):n_w) \right) \quad (2.5)$$

Where n_w is the last point of the windowed signal, which is equal to the sample point corresponding to 356 μs . S is the signal voltage values for all samples. t_w is the desired sample point for calculating the AIC, which ranges from 1 to n_w . σ^2 is the variance of signal voltages in the desired range. The AICs are calculated for all the sample points in the windowed signals, and the minimum values denote TOAs of the signals.

Another factor which can affect the source location results is the selection of appropriate signals (hits) in an event for source location. Each event may have more than four hits (the minimum hit number for 3D source location), some of which are very weak, and it is hard to find the TOA even by using AIC. Therefore, a method [48] based on the second derivative of AIC was employed for hit selection in an event. The certainty levels (CL) of calculated TOAs are calculated by the following equation [48]:

$$CL = [AIC(t_{min} - \delta t) + AIC(t_{min} + \delta t) - 2AIC(t_{min})]/\delta t^2 \quad (2.6)$$

Where t_{min} is the time in a signal corresponding to the minimum AIC. δt is a small-time interval around the estimated TOA (minimum AIC). This parameter is set to 15 μs according to the AE data for the medium-scale specimens. The lower values for CL show unreliably estimated TOA by AIC and can be deleted if there is a sufficient number of hits.

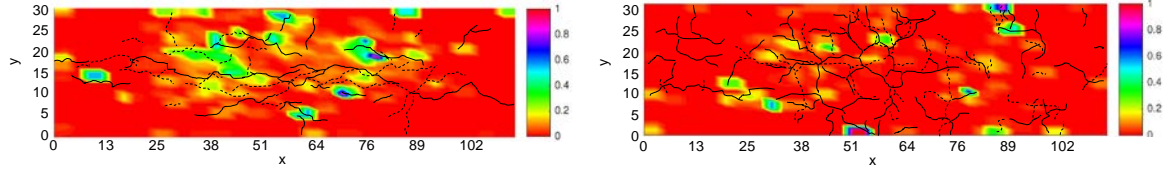
2.4.3 Iterative method and damage imaging

After modifying the time of arrivals of AE signals, the following formulation should be solved and optimized:

$$F_n(X_S, Y_S, Z_S, V) = (t_n - t_1) - [\sqrt{(x_n - X_S)^2 + (y_n - Y_S)^2 + (z_n - Z_S)^2} - \sqrt{(x_1 - X_S)^2 + (y_1 - Y_S)^2 + (z_1 - Z_S)^2}] / V \quad (2.7)$$

Where X_S , Y_S , and Z_S are source coordinates and “ V ” is wave velocity. n ranges between 2 to the number of sensors, which register an event. x_1 , y_1 , and z_1 are the coordinates of the first sensor which captures the signal. The nonlinear least-squares method [52-55] was used to minimize the Eq. (2.7).

The results of source locations were presented in contour diagrams by considering the cumulative signal strength of the events. The specimens are initially meshed. The enclosed area in each mesh is called a “cell”. Then, a code was developed to read the input file which was the result of the source location, and weight values were assigned to the nodes in each cell according to the number of repeated events in each cell and the average signal strength of each event. The weights for each source location was added to the previous events if the events were located in the same cell. The weights in all cells were normalized to the maximum weight at the end of the test. The result is a contour diagram which shows the concentration of damage. An example of damage contours is presented in Figure 2.5 for the medium-scale specimens affected by ASR after 300 days.



(a) Confined specimen

(b) Unconfined specimen

Figure 2.5 Damage imaging contours for medium-scale specimens

2.5 Signal processing methods

2.5.1 Fast Fourier transform (FFT)

Fourier transform is a common method for transferring a signal from the time domain to the frequency domain. The discrete version of Fourier transform is utilized for digital waveforms, which is referred to as Discrete Fourier Transform (DFT), and is presented in the following equation:

$$X_k = \sum_{n=0}^{N-1} x_n e^{-\frac{j2\pi kn}{N}} \quad (2.8)$$

Where N is the number of samples. “ x_n ” is a signal in a time domain and X_k is the Fourier transform coefficients for k^{th} frequency. An example of the application of FFT in this dissertation is deriving frequency-energy based features for clustering the data as mentioned in the previous section.

2.5.2 Continuous wavelet analysis

The wavelet transform (WT) is utilized to present the energy distributions of signals in the time-frequency domain. Contrary to windowed Fourier transform (WFT), wavelet transform (WT) presents data in a high time resolution for the high-frequency components and a high-frequency resolution for the low-frequency components. The continuous wavelet transform (CWT) is defined according to the following equation:

$$CWT(a, b) = \int S(t) * |a|^{-0.5} \Psi \left(\frac{t-b}{a} \right) dt \quad (2.9)$$

Where “a” and “b” are scale and shift parameters, respectively. Scale parameters govern the compactness or extension of a signal (frequency), and shift parameters determine the position of the mobile window in the time domain. “S(t)” is a signal time history. Eq. (2.10) is referred to as the wavelet, which is the second portion of Eq. (2.9). The basic window function without scale and shift parameters are referred to as the mother wavelet.

$$\Psi_{a,b}(t) = |a|^{-0.5} \Psi \left(\frac{t-b}{a} \right) \quad (2.10)$$

The mother wavelet used in this study is the Gabor wavelet, which is based on a Gaussian function [56]. The results of wavelet analysis are the wavelet coefficients for the different combinations of time and frequency, which are presented in a contour diagram or spectrogram.

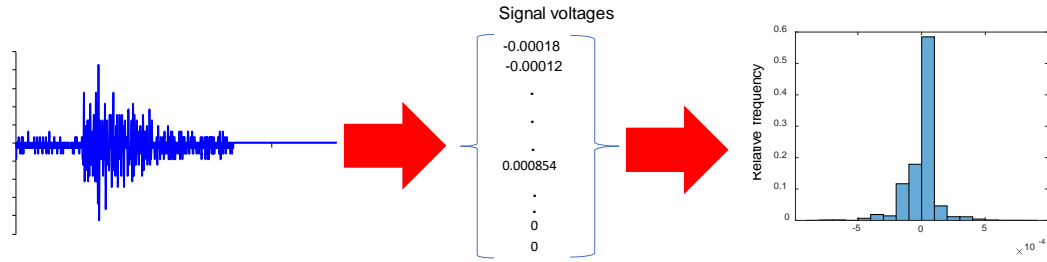
2.5.3 Shannon's entropy (Information entropy)

There are different methods for calculating signal entropy in literature, which have been mostly employed for fatigue tests [57-61]. The methods, which include voltage amplitude entropy, feature entropy, and fast Fourier transform (FFT) entropy, are presented in this section.

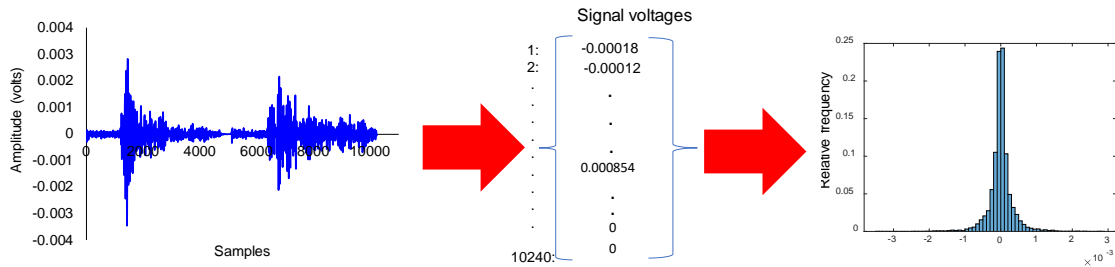
The voltage entropy is calculated based on the distribution of amplitude voltages of AE signals. The voltage amplitudes of each AE signal are used to develop a histogram of signal. The bin size is recommended to be close to the resolution of AE data acquisition systems [58]. The resulted histogram contains several bars corresponding to the bins. Each bar shows the relative frequency of voltages within a bin. Then, voltage entropy is calculated according to the Shannon entropy equation:

$$Entropy = - \sum_{i=1}^n P(x_i) * \log (P(x_i)) \quad (2.11)$$

In the equation, n is the number of bins in each signal. x_i represents the bins defined in each signal. $P(x_i)$ is the relative frequency of each bin calculated according to the signal histogram. The procedure is shown in Figure 2.6. In this method, it is assumed that the voltage value changes constantly and independently between samples. There are two approaches for calculating the entropy. One approach is calculating the entropy for each signal, namely discrete voltage entropy (DVE) in this paper (Figure 2.6a). The other approach is calculating the entropy, based on all signal voltages up to the desired experiment time. In this method, the amplitude voltages of all signals up to the desired time are used to derive a histogram and calculate an entropy. This method is referred to as global voltage entropy (GVE). In Figure 2.6b, the signal voltages for two signals were used for developing a histogram and calculating an entropy. The next entropy is going to be calculated by using three signals. This will be continued until all signals are included in the calculation.



(a) Discrete voltage entropy



(b) Global voltage entropy

Figure 2.6 Entropy calculation using signal amplitude voltage

Another method is named the counts-entropy. There are two methods for calculating the counts-entropy. For both calculation methods, it is assumed that each count is independent of other counts. In the first calculation method, the probability is calculated by dividing the counts of a signal corresponding to the desired time over the cumulative counts up to that time. Then counts-entropy is calculated by using Shannon entropy Eq. (2.11). This method is referred to as CE. CE will be updated when a new signal is received. In the second procedure, the cumulative distribution function (CDF) for counts up to the desired time is estimated by using the empirical CDF method [59] and the corresponding probability distribution function (PDF) is derived. The entropy is estimated using the probability distribution for each bin using Eq. (2.11). This method is

referred to as CE_CDF in this study. The procedure is repeated when a new signal is received.

The third method, namely FFT Entropy, is calculated by using FFT spectra of signals. The AE signals are converted into the frequency domains using FFT. The results are the FFT spectra. The spectra are normalized by the total energies of the signals. The normalized spectra are considered as probability distributions in the frequency domain. Then, Shannon entropy is estimated from each spectrum. The procedure is presented in Figure 2.7.

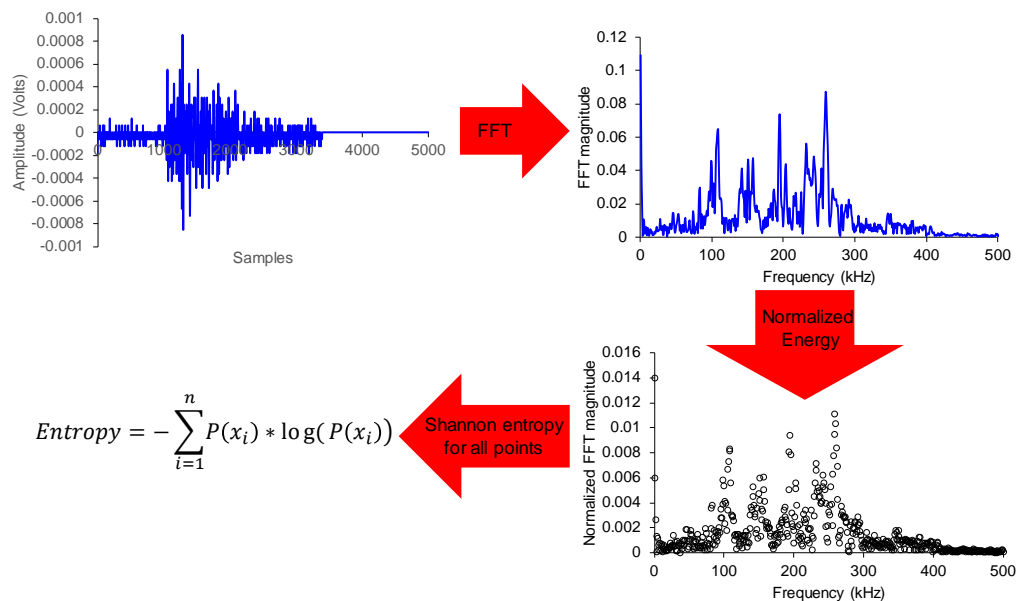


Figure 2.7 FFT Entropy

2.6 AE-based damage index methods

2.6.1 Intensity analysis and CSS gradient

One of the common methods for deriving damage indices based on AE data is intensity analysis. This analysis has been utilized for damage level identification for different structures under loading [26,62-65]. In this analysis, two parameters of the

historic index (HI) and severity (S_r) are calculated. The parameters are presented as follows:

$$H(t) = \frac{N}{N-K} \frac{\sum_{i=k+1}^N S_{oi}}{\sum_{i=1}^N S_{oi}} \quad (2.12)$$

$$S_r = \frac{1}{J} \sum_{i=1}^{i=50} S_{oi} \quad (2.13)$$

In the above equations, N is the number of hits up to the desired time. K and J are empirically derived parameters. Although this method has been utilized for different structures, especially structures under external loading, the empirical dependency of parameters causes limitations. Researchers have proposed different parameters for the intensity analysis [23,63,65] Therefore, a comparison between analysis results from case to case is very challenging.

In the case of ASR, the variability between empirical parameters for the intensity analysis is even worse, because AE temporal distribution depends on several factors such as stress boundary conditions, the concrete mixture, aggregate types, and environmental conditions (e.g. temperature and humidity) in addition to specimen size, sensor types, and sensor layout.

The rate change in cumulative signal strength (CSS) can be an appropriate parameter to evaluate damage in structures based on AE data. The CSS rate is roughly estimated by HI in the intensity analysis. The HI in each desired time is an average ratio between the CSS for the hits adjacent to the desired time to the CSS for the hits from the beginning of the test up to the desired time. Therefore, HI depends directly on the AE data distribution adjacent to the desired time. For example, HI for a case with a denser AE data adjacent to the desired time would be different from a case with a smaller amount of data even if the CSS curves for two cases are identical. Therefore, HI does not

present consistent results for the two identical tests. In addition, HI does not show consistent results during a single test because the AE temporal distribution is not uniform during the test.

In this study, gradients of normalized CSS of the medium-scale unconfined and confined specimens are employed for comparison purposes and observation of their temporal trends. Numerical gradients using centered differentiation is used according to the following equation.

$$G(i) = \frac{CSS(i+1) - CSS(i-1)}{2} \quad (2.14)$$

To reduce the dependency of the gradient to the AE distribution, linear interpolation is used to derive samples corresponding to the desired time with a constant sampling rate. Then, resulting CSS is used for calculating the gradient in each sample (i). The sampling rate in this study is one sample per day.

2.6.2 *b*-value analysis

Another common method for damage detection using AE is *b*-value analysis. This method is based on the Gutenberg-Richter equation in seismology [66]. The equation states that large-magnitude earthquakes occur less frequently than small-magnitude earthquakes. This concept has been utilized in AE for damage identification [66-68]. The *b*-values are usually calculated using the following equation:

$$\log N = a - b \left(\frac{A_{dB}}{20} \right) \quad (2.15)$$

Where N is the number of AE hits with a magnitude equal to or greater than an amplitude of a hit. Linear regression is conducted between the $\log N$ and $A_{dB}/20$ to calculate model parameters (a and b). All data are separated into a specific subset

number. Then, the b-values are calculated separately in each subset. This method is referred to as the incremental b-value (Inc-b).

The coefficient of determination for each b-value is calculated. This factor may also be considered as a damage identification criterion because it is expected that severe damage formation emits AE signals with large amplitudes. The AE signals with large amplitudes cause deviation from mostly linear amplitude-logN distribution and consequently, reduction in coefficient of determination. The coefficient of determination is calculated using the following equation:

$$\text{Regression coefficient} = 1 - \frac{\sum_{i=1}^n (\hat{y}_i - y_i)^2}{\sum_{i=1}^n (y_i - \bar{y})^2} \quad (2.16)$$

Where \hat{y}_i is the estimated value of $\log N$ for an i^{th} point by using a fitted line and y_i is the real value of $\log N$ for the i^{th} point. \bar{y} is the average value of $\log N$. Index n denotes the last desired data to calculate the b-value.

The $\log N$ versus amplitude distribution is usually not perfectly linear, especially for large and small amplitudes (upper and lower part of the distribution). Therefore, some researchers have proposed to consider upper and lower bands for the dataset [67,69,70]. This method is referred to as Improved b-value in the literature. If it is calculated based on incremental intervals, it is referred to as the incrementally improved b-value (Inc-Ib). The upper limit and lower limit are defined by A_2 and A_1 .

$$A_2 = \mu - \alpha_1 \sigma \text{ and } A_1 = \mu + \alpha_2 \sigma \quad (2.17)$$

The slope between upper and lower limits in $\log N$ versus amplitude distribution results in an improved b-value (Ib). This calculation is based on the assumption that the distribution between upper and lower limits is linear.

$$Ib = \frac{[\log A_2 - \log A_1]}{[A_2 - A_1]} \quad (2.18)$$

In this dissertation, instead of using the above equation, average (μ) and standard deviation (σ) of each data subset is calculated, and the data, which exceed $\mu + \alpha_2\sigma$ or are less than $\mu - \alpha_1\sigma$, are deleted. Then, b-values for the remaining data are calculated. The parameters α_1 and α_2 range from 0.5 to 2. In this paper, α_1 and α_2 are equal to unity.

2.7 References

1. ElBatanouny, M.K.; Ziehl, P.H.; Larosche, A.; Mangual, J.; Matta, F.; Nanni, A. Acoustic emission monitoring for assessment of prestressed concrete beams. *Construction and Building Materials* **2014**, *58*, 46-53.
2. Abdelrahman, M.; ElBatanouny, M.K.; Ziehl, P.; Fasl, J.; Larosche, C.J.; Fraczek, J. Classification of alkali-silica reaction damage using acoustic emission: A proof-of-concept study. *Construction and Building Materials* **2015**, *95*, 406-413.
3. Lokajíček, T.; Přikryl, R.; Šachlová, Š.; Kuchařová, A. Acoustic emission monitoring of crack formation during alkali silica reactivity accelerated mortar bar test. *Engineering geology* **2017**, *220*, 175-182.
4. Farnam, Y.; Geiker, M.R.; Bentz, D.; Weiss, J. Acoustic emission waveform characterization of crack origin and mode in fractured and asr damaged concrete. *Cement and Concrete Composites* **2015**, *60*, 135-145.
5. Weise, F. Innovative measurement techniques for characterising internal damage processes in concrete due to asr. **2012**.
6. ASTM, E. Standard terminology for nondestructive examinations. 2006.
7. ElBatanouny, M.K.; Ziehl, P.H.; Larosche, A.; Mangual, J.; Matta, F.; Nanni, A. Acoustic emission monitoring for assessment of prestressed concrete beams. *Construction Building Materials* **2014**, *58*, 46-53.

8. Elfergani, H.A.; Pullin, R.; Holford, K.M. Damage assessment of corrosion in prestressed concrete by acoustic emission. *Construction and Building Materials* **2013**, *40*, 925-933.
9. Ziehl, P.; ElBatanouny, M. Acoustic emission monitoring for corrosion damage detection and classification. In *Corrosion of steel in concrete structures*, Elsevier: 2016; pp 193-209.
10. Van Steen, C.; Pahlavan, L.; Wevers, M.; Verstrynge, E. Localisation and characterisation of corrosion damage in reinforced concrete by means of acoustic emission and x-ray computed tomography. *Construction Building Materials* **2019**, *197*, 21-29.
11. Van Steen, C.; Verstrynge, E.; Wevers, M.; Vandewalle, L. Assessing the bond behaviour of corroded smooth and ribbed rebars with acoustic emission monitoring. *Cement Concrete Research* **2019**, *120*, 176-186.
12. Patil, S.; Karkare, B.; Goyal, S. Corrosion induced damage detection of in-service rc slabs using acoustic emission technique. *Construction Building Materials* **2017**, *156*, 123-130.
13. Xu, J.; Han, E.-H.; Wu, X. Acoustic emission response of 304 stainless steel during constant load test in high temperature aqueous environment. *Corrosion Science* **2012**, *63*, 91-99.
14. Alvarez, M.; Lapitz, P.; Ruzzante, J. Ae response of type 304 stainless steel during stress corrosion crack propagation. *Corrosion Science* **2008**, *50*, 3382-3388.

15. Kovač, J.; Legat, A.; Zajec, B.; Kosec, T.; Govekar, E. Detection and characterization of stainless steel scc by the analysis of crack related acoustic emission. *Ultrasonics* **2015**, *62*, 312-322.
16. Du, G.; Li, J.; Wang, W.; Jiang, C.; Song, S.J.C.S. Detection and characterization of stress-corrosion cracking on 304 stainless steel by electrochemical noise and acoustic emission techniques. **2011**, *53*, 2918-2926.
17. Shaikh, H.; Amirthalingam, R.; Anita, T.; Sivaibharasi, N.; Jaykumar, T.; Manohar, P.; Khatak, H. Evaluation of stress corrosion cracking phenomenon in an aisi type 316ln stainless steel using acoustic emission technique. *Corrosion Science* **2007**, *49*, 740-765.
18. Anastasopoulos, A.; Kourousis, D.; Bollas, K. Acoustic emission leak detection of liquid filled buried pipeline. *Journal of Acoustic Emission* **2009**, *27*.
19. Mostafapour, A.; Davoudi, S. Analysis of leakage in high pressure pipe using acoustic emission method. *Applied Acoustics* **2013**, *74*, 335-342.
20. Ye, G.-Y.; Xu, K.-J.; Wu, W.-K. Standard deviation based acoustic emission signal analysis for detecting valve internal leakage. *Sensors Actuators A: Physical* **2018**, *283*, 340-347.
21. Yu, J.; Ziehl, P.; Zárate, B.; Caicedo, J. Prediction of fatigue crack growth in steel bridge components using acoustic emission. *Journal of Constructional Steel Research* **2011**, *67*, 1254-1260.
22. Abdelrahman, M.; ElBatanouny, M.K.; Ziehl, P.H. Acoustic emission based damage assessment method for prestressed concrete structures: Modified index of damage. *Engineering Structures* **2014**, *60*, 258-264.

23. Nair, A.; Cai, C. Acoustic emission monitoring of bridges: Review and case studies. *Engineering Structures* **2010**, *32*, 1704-1714.
24. Noorsuhada, M. An overview on fatigue damage assessment of reinforced concrete structures with the aid of acoustic emission technique. *Construction Building Materials* **2016**, *112*, 424-439.
25. Behnia, A.; Chai, H.K.; Ranjbar, N.; Jumaat, M.Z. Damage detection of sfrc concrete beams subjected to pure torsion by integrating acoustic emission and weibull damage function. *Structural Control Health Monitoring* **2016**, *23*, 51-68.
26. Golaski, L.; Gebski, P.; Ono, K. Diagnostics of reinforced concrete bridges by acoustic emission. *Journal of acoustic emission* **2002**, *20*, 83-89.
27. Abdelrahman, M.; ElBatanouny, M.K.; Ziehl, P.; Fasl, J.; Larosche, C.J.; Fraczek, J. Classification of alkali-silica reaction damage using acoustic emission: A proof-of-concept study. *Construction Building Materials* **2015**, *95*, 406-413.
28. Weise, F.; Voland, K.; Pirskawetz, S.; Meinel, D. In *Innovative measurement techniques for characterising internal damage processes in concrete due to asr*, Proceedings of the International Conference on Alkali Aggregate Reaction (ICAAR), University of Texas, Austin, TX, USA, 2012; pp 20-25.
29. Soltangharaei, V.; Anay, R.; Hayes, N.; Assi, L.; Le Pape, Y.; Ma, Z.; Ziehl, P. Damage mechanism evaluation of large-scale concrete structures affected by alkali-silica reaction using acoustic emission. *Applied Sciences* **2018**, *8*, 2148.
30. Thomas, M.D.; Folliard, K.J.; Fournier, B.; Rivard, P.; Drimalas, T.; Garber, S.I. *Methods for evaluating and treating asr-affected structures: Results of field*

- application and demonstration projects–volume ii: Details of field applications and analysis*; 2013.
31. Seo, J.; Wacker, J.P.; Duque, L. *Evaluating the use of drones for timber bridge inspection*; General Technical Report FPL-GTR-258; Department of Agriculture, Forest Service, Forest Products Laboratory: Madison, WI, U.S., 2018; pp 1-152.
 32. Zink, J.; Lovelace, B. *Unmanned aerial vehicle bridge inspection demonstration project*; MN/RC 2015-40; Minnesota Department of Transportation, Office of Transportation System Management: 2015.
 33. Yang, C.-H.; Wen, M.-C.; Chen, Y.-C.; Kang, S.-C. In *An optimized unmanned aerial system for bridge inspection*, ISARC. Proceedings of the International Symposium on Automation and Robotics in Construction, 2015; IAARC Publications: p 1.
 34. Everitt, B.S. *An r and s-plus® companion to multivariate analysis*. Springer Science & Business Media: 2006.
 35. Tan, P.N.; Steinbach, M.; Kumar, V. Data mining cluster analysis: Basic concepts and algorithms. *Introduction to data mining* **2013**.
 36. Murtagh, F.; Legendre, P. Ward's hierarchical agglomerative clustering method: Which algorithms implement ward's criterion? *Journal of classification* **2014**, *31*, 274-295.
 37. Solomatine, D.; See, L.M.; Abrahart, R. Data-driven modelling: Concepts, approaches and experiences. In *Practical hydroinformatics*, Springer: 2009; pp 17-30.

38. Sobieszczanski-Sobieski, J.; Morris, A.; van Tooren, M.J.; La Rocca, G.; Yao, W. Guided random search and network techniques. *Multidisciplinary Design Optimization Supported by Knowledge Based Engineering* **2015**, 80-97.
39. Gavin, H. The levenberg-marquardt method for nonlinear least squares curve-fitting problems. 2011.
40. Ott, R.L.; Longnecker, M.T. *An introduction to statistical methods and data analysis*. Nelson Education: 2015.
41. Epanechnikov, V.A. Non-parametric estimation of a multivariate probability density. *Theory of Probability Its Applications* **1969**, *14*, 153-158.
42. Wand, M.P.; Jones, M.C. *Kernel smoothing*. Chapman and Hall/CRC: 1994.
43. Kobayashi, Y.; Shiotani, T. Computerized ae tomography. In *Innovative ae and ndt techniques for on-site measurement of concrete and masonry structures*, Springer: 2016; pp 47-68.
44. Shiotani, T.; Nishida, T.; Nakayama, H.; Asaue, H.; Chang, K.-C.; Miyagawa, T.; Kobayashi, Y. Fatigue failure evaluation of rc bridge deck in wheel loading test by ae tomography. In *Advances in acoustic emission technology*, Springer: 2017; pp 251-264.
45. Schubert, F. Basic principles of acoustic emission tomography. *Journal of Acoustic Emission* **2004**, *22*, 147-158.
46. Ge, M. Analysis of source location algorithms part 1: Overview and non-iterative methods. *Acoustic Emission* **2003**, *21*, 14-24.
47. Mistras-Group. Express-8 ae system user manual. Princeton Junction, NJ, USA, 2014.

48. Carpinteri, A.; Xu, J.; Lacidogna, G.; Manuello, A. Reliable onset time determination and source location of acoustic emissions in concrete structures. *Cement concrete composites* **2012**, *34*, 529-537.
49. Madarshahian, R.; Ziehl, P.; Caicedo, J.M. Acoustic emission bayesian source location: Onset time challenge. *Mechanical Systems Signal Processing* **2019**, *123*, 483-495.
50. Bai, F.; Gagar, D.; Foote, P.; Zhao, Y. Comparison of alternatives to amplitude thresholding for onset detection of acoustic emission signals. *Mechanical Systems Signal Processing* **2017**, *84*, 717-730.
51. Akaike, H. Information theory and an extension of the maximum likelihood principle. In *Selected papers of hirotugu akaike*, Springer: 1998; pp 199-213.
52. Ge, M. Analysis of source location algorithms: Part 2. Iterative methods. *Journal of Acoustic Emission* **2003**, *21*, 29-51.
53. Dennis Jr, J.E.; Welsch, R.E. Techniques for nonlinear least squares and robust regression. *Communications in Statistics-Simulation Computation* **1978**, *7*, 345-359.
54. Torkjazi, M.; Mirjafari, P.S.; Poorzahedy, H. Reliability-based network flow estimation with day-to-day variation: A model validation on real large-scale urban networks. *Journal of Intelligent Transportation Systems* **2018**, *22*, 121-143.
55. Khan, S.M.; Islam, S.; Khan, M.Z.; Dey, K.; Chowdhury, M.; Huynh, N.; Torkjazi, M. Development of statewide annual average daily traffic estimation model from short-term counts: A comparative study for south carolina. *Transportation Research Record* **2018**, *2672*, 55-64.

56. Suzuki, H.; Kinjo, T.; Hayashi, Y.; Takemoto, M.; Ono, K.; Hayashi, Y. Wavelet transform of acoustic emission signals. *Journal of Acoustic Emission* **1996**, *14*, 69-84.
57. Kahirdeh, A.; Sauerbrunn, C.; Yun, H.; Modarres, M. A parametric approach to acoustic entropy estimation for assessment of fatigue damage. *International Journal of Fatigue* **2017**, *100*, 229-237.
58. Chai, M.; Zhang, Z.; Duan, Q. A new qualitative acoustic emission parameter based on shannon's entropy for damage monitoring. *Mechanical Systems Signal Processing* **2018**, *100*, 617-629.
59. Kahirdeh, A. Energy dissipation and entropy generation during the fatigue degradation: Application to health monitoring of composites. Louisiana State University, 2014.
60. Sauerbrunn, C.M. Evaluation of information entropy from acoustic emission waveforms as a fatigue damage metric for al7075-t6. 2016.
61. Kahirdeh, A.; Sauerbrunn, C.; Modarres, M. In *Acoustic emission entropy as a measure of damage in materials*, AIP Conference Proceedings, 2016; AIP Publishing: p 060007.
62. Fowler, T.J.; Blessing, J.A.; Conlisk, P.J.; Swanson, T.L. The monpac system. *Journal of acoustic emission* **1989**, *8*, 1-8.
63. Di Benedetti, M.; Nanni, A. Acoustic emission intensity analysis for in situ evaluation of reinforced concrete slabs. *Journal of materials in civil engineering* **2013**, *26*, 6-13.

64. Abouhussien, A.A.; Hassan, A.A. The use of acoustic emission intensity analysis for the assessment of cover crack growth in corroded concrete structures. *Journal of Nondestructive Evaluation* **2016**, *35*, 52.
65. Vélez, W.; Matta, F.; Ziehl, P. In *Acoustic emission intensity analysis of corrosion in prestressed concrete piles*, AIP Conference Proceedings, 2014; AIP: pp 888-894.
66. Colombo, I.S.; Main, I.; Forde, M. Assessing damage of reinforced concrete beam using “b-value” analysis of acoustic emission signals. *Journal of Materials in Civil Engineering* **2003**, *15*, 280-286.
67. Rao, M.; Lakshmi, K.P. Analysis of b-value and improved b-value of acoustic emissions accompanying rock fracture. *Current science* **2005**, 1577-1582.
68. Jung, D.Y.; Mizutani, Y.; Todoroki, A.; Suzuki, Y. Frequency dependence of the b-value used for acoustic emission analysis of glass fiber reinforced plastics. *Open Journal of Composite Materials* **2017**, *7*, 117.
69. Shiotani, T. Evaluation of progressive failure using ae sources and improved b-value on slope model tests. *Progress in Acoustic Emission VII* **1994**, 529-534.
70. Shiotani, T. Application of the ae improved b-value to quantitative evaluation of fracture process in concrete-materials. *Journal of acoustic emission* **2001**, *19*, 118-133.

Chapter 3
Evaluation of Damage Propagation in Cement Paste Using Pattern
Recognition¹

¹ Vafa Soltangharai, Rafal Anay, Lateef Assi, John R. Rose, and Paul Ziehl. Evaluation of damage propagation in cement paste using pattern recognition. To be submitted to the *Journal of Construction and Building Materials*.

3.1 Abstract

The focus of this research is the identification of cracking mechanisms for cement paste using acoustic emission (AE) data. The data is recorded from compression and notched four-point bending tests. Cracks in cement paste prisms under compressive loading randomly appear and scatter through specimens. Therefore, investigating cracking mechanisms using acoustic emission and the identification of signal signature will be challenging for data recorded during compression tests. The primary innovation in this manuscript lies in a recommended method to relate AE data from a compression test to a more controlled test in terms of crack formation (e.g., four-point bending) to analyze the AE data and study cracking mechanisms. The method includes an agglomerative hierarchical clustering method, an artificial neural network, and a ray-tracing source localization algorithm. An agglomerative hierarchical clustering method is utilized for clustering the AE data from a compression test using frequency-dependent features. A neural network is trained using the compression test data and applied to the AE data emitted during the four-point bending test. The clustered data from the four-point bending test are localized using a ray-tracing algorithm. Based on the occurrence and locations of the clustered events and signal feature analyses, potential cracking mechanisms are identified and assigned to the AE signals.

Keywords: Acoustic emission; artificial neural network; cement paste; crack mechanism; ray-tracing algorithm; unsupervised pattern recognition

3.2 Introduction

Cracks in cementitious material have shown to have an influence on the durability of concrete structures [1-3]. Cracks raise hydraulic permeability rate of water flow inside

concrete structures and provide easier paths to transfer deteriorating agents such as chlorides [4-8]. Cracks may be formed due to several external and internal factors including alkali-silica reaction, rebar corrosion, drying and chemical shrinkage, freeze-thaw cycling, temperature gradients, sulfate attack, and loading [9-13]. Concrete is inherently brittle; but, it is one of the most widely used materials for construction [14]. Therefore, evaluating damage mechanisms for this material is of interest.

One of the most important mechanical characteristics of concrete is its compressive strength. Aggregate, the quality of interfacial transition zone, and air voids are primary factors which affect the mechanical behavior of concrete under compressive loading [15]. The cement matrix is one of the concrete components, and the nonlinear damage behavior of concrete depends strongly on the cement paste [16,17]. Furthermore, the cementation of radioactive waste material in saltstone is considered as one of the common immobilization methods for nuclear power plant waste [18,19]. Microcracks in cementitious materials increase the hydraulic conductivity of water and consequently transfer the nuclear waste material from cementitious materials [7,20]. Consequently, evaluation of crack formation mechanisms provides insight for long term evaluation of nuclear waste disposal structures.

In this paper, crack formation mechanisms of cement paste during compression and flexural tests are evaluated. Several methods are described in the literature for studying the compressive behavior of cementitious materials, including strain gauges, x-ray tomography [21-24], and acoustic emission (AE). Acoustic emission is a nondestructive method, which has been utilized for health monitoring and condition assessment of structures and to assess damage behavior of stone and cementitious

materials under compression and bending [14,25-36]. The effect of aggregate size and weight ratio on the fracture energy of concrete beams using AE data was evaluated by Chen and Liu [30]. They observed that fracture energy increased for a mixture with large aggregates due to the deviation of crack paths toward the cement paste, resulting in a larger fracture process zone. Elaqla et al. [13] studied the effect of aggregates to cement weight ratio on compressive behavior of cement mortar by utilizing x-ray tomography, AE, and strain gauges. Lacidogna et al. [36] conducted four-point bending tests on pre-notched concrete beams and compared released AE energy with dissipated energy. Carpinteri et al. [32] investigated crack formation modes by utilizing rise angle and average frequency of signals. Furthermore, they studied the correlation between absorbed, released, and cumulative AE energy for concrete under uniaxial compressive loading. Guzman, et al. [33] utilized AE to study the behavior of reinforced concrete beams under four-point bending tests. AE parameters such as rise angle, average frequency, and the b-value were used to investigate the mechanical behavior of beams. It was concluded that b-value had an increasing trend up to 55% of the final load when microcracks were predominant over macrocracks and decreased when macrocracks were observed. Fracture mechanisms of concrete and mortar beams were studied using AE parametric analyses in Sagar and Prasad [34]. Three stages were determined before failure: crack initiation, stable crack growth, and nucleation.

Researchers have utilized different methods and parameters to analyze AE data and study damage mechanisms. The parameters are mainly threshold-dependent, i.e., they change with threshold and do not fully represent characteristics of AE waveforms, especially for weak signals. Furthermore, AE signals have several descriptors which

should be simultaneously accounted due to the complexity of damage evaluation. Traditional methods do not consider multi-variable input features. Therefore, in this study, multiple-features were employed to overcome the limitations of conventional analysis methods.

In this manuscript, cracking mechanisms of cement paste prisms under compressive and bending loading were studied through AE. Cracking in cement paste prisms under compressive loading in this study was very scattered and random due to the brittleness and a large aspect ratio. Therefore, AE source location and the identification of cracking mechanisms for the compression test were challenging. An innovative method was recommended to relate compression results to a test with a more controlled crack opening, e.g. notched four-point bending test. An agglomerative hierarchical clustering method was employed for classifying AE data emitted during a compression test for a cement paste prism using frequency-dependent features. An artificial neural network (ANN) was trained using the clustered data and applied to the AE data recorded during a four-point bending test, thereby classifying the new data, and clustered hits were localized using a ray-tracing source location algorithm. The potential damage mechanisms for the flexural and compression specimens were then determined through evaluating frequency and non-frequency dependent features, event locations, and the sequence of event occurrence. The mechanical fracture behavior of the cement paste in flexure was also studied.

Limited research has been published regarding AE data analysis using unsupervised pattern recognition for damage evaluation of cementitious material under compressive and flexural loading with only non-frequency dependent features [37,38]

and there is no published paper regarding using frequency-dependent features and pattern recognition to study the fracture in cement paste. This gap in the literature is also addressed in the current manuscript.

3.3 Materials and experimental test setup

Portland cement Type I/II was mixed with water in accordance with ASTM C305 [39]. A water to cement weight ratio of 0.5 was used for the mixture. The high water to mixture ratio is commonly utilized in saltstone grout (one of the immobilization methods for radioactive waste) [40]. Therefore, in this study, a water to cement ratio of 0.5 was selected. Specimen dimensions for compression and four-point bending tests were 38.1mm × 38.1mm × 152.4mm (1.5 inch × 1.5 inch × 6 inches) and 38.1mm × 38.1mm × 177.8mm (1.5 inch × 1.5 inch × 7 inches), respectively. The specimens were demolded after 24 hours and cured in a lime and water solution at the temperature of $23 \pm 2^\circ \text{C}$ for 49 days. The specimens were removed from the solution and dried at ambient temperature for 8 to 10 hours before testing.

3.3.1 Compression test setup

Ten sensors were attached to specimen surfaces. Eight micro 30 resonant sensors (operating frequency range of 150-400 kHz) and two broadband sensors (operating frequency range of 50-2000 kHz) were utilized. A thin layer of epoxy coated the specimen surfaces to provide a smooth surface, and then the sensors were attached with hot glue. For reducing potential noise due to friction, Teflon sheets and polyurethane pads were located at the ends of the specimens. The test setup for the compression test is presented in Figure 3.1. Sensors 5 and 6 are on the back face, and sensors 7 and 8 are on the right side of the specimen. The specimen was loaded with a uniaxial compressive

displacement at a constant rate of 0.1 mm/min employing a 20-kip capacity closed-loop test frame.

A 16-channel DiSP system manufactured by MISTRAS Group, Inc. (Princeton Junction, New Jersey) was utilized for data acquisition. Pre-amplifiers with 40 dB gain and bandpass internal filters with a frequency range of 100 to 1200 kHz were connected to the sensors. A background noise test was conducted, and the threshold was set to 32 dB. The sensitivity of the sensors was checked by applying Hsu-Nielsen sources [41].

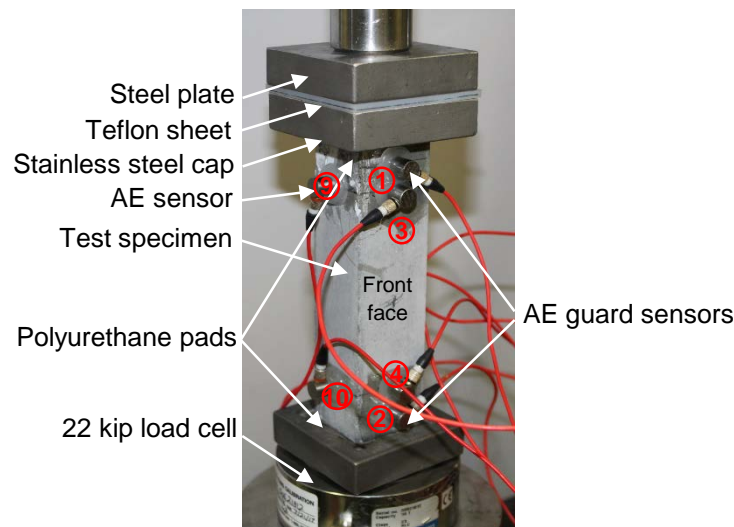


Figure 3.1 Compression test setup and sensor layout

Four specimens with AE sensors were tested under compressive loads. The first specimen was loaded close to ultimate capacity. The test was stopped for this specimen when large vertical cracks were observed in the specimen and the cracks divided the specimen. This specimen was named P-100. Then, different percentages of the final compressive load for P-100% were assumed for loading other specimens. The specimens and corresponding load values are presented in Table 3.1. The AE data for P-40 were used for data analysis. This specimen contained a few visible cracks. A large amount of

AE data was captured before the first visible crack, which can be attributed to microcrack formations. Therefore, AE data for this specimen is expected to include both data from microcrack and macrocrack formations, and it has minimal extraneous AE data caused by crack friction. The AE data is also sufficient for clustering analysis. Afterward, frequency-dependent features were derived from the recorded signals, and unsupervised pattern recognition was utilized to cluster the data.

Table 3.1 Specimens for compression test

Specimen	Load (N)	Load percentage (%)
P-100	10253	100
P-80	8385	82
P-60	6808	66
P-40	4343	42

3.3.2 Four-point bending test setup

A beam with similar dimensions to the compression specimens was used for a four-point bending test. Twelve sensors (four broadband and eight resonant) were used. Sensor types and installation procedures were as mentioned in the previous section. Sensor location and test setup are shown in Figure 3.2. A notch with a width and depth of 1mm was made at the mid-span bottom of the specimen. The span length of the beam was 152 mm (6 inches), and the distance between two localized forces was 50.8 mm (2 inches). A clip gauge was installed at the mid-span of the beam to measure the opening of the notch. The specimen was loaded in displacement-control mode at a rate of 0.01 mm/min employing a 50-kip capacity closed-loop test frame. A one-kip load cell was employed to record the load during the test. The data acquisition setup and specimen preparation were identical to the procedure for the compression test.

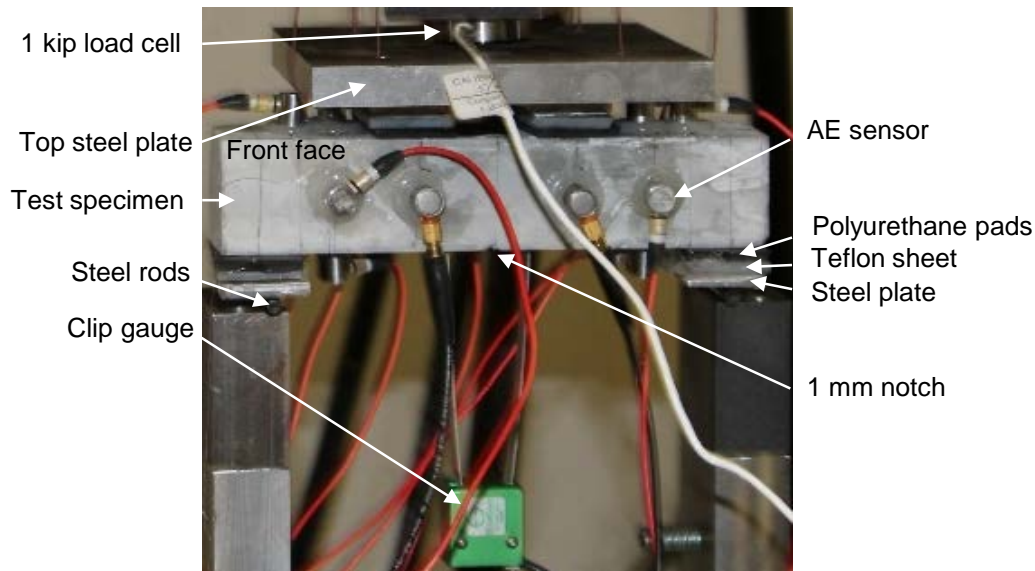


Figure 3.2 Bending test setup and sensor layout

3.4 Analytical and experimental procedure

Analyzing AE data and related damage mechanisms for cement paste prisms under compressive loading is complex because cracks randomly appear and scatter. It is more straightforward to investigate crack formation mechanisms, especially for a brittle material under a more controlled condition, through a notched four-point bending test. Therefore, a notched beam with the same dimension as the compression specimen was loaded to failure. AE data were recorded, and frequency-dependent features were derived. The features were used to cluster the AE data from the compression test.

The clusters from the compression test were related to the AE data in the four-point bending test through supervised pattern recognition. A neural network was trained using the clusters from the compression test. The trained network was then applied to the data recorded during the four-point bending test. Using source location and signal feature

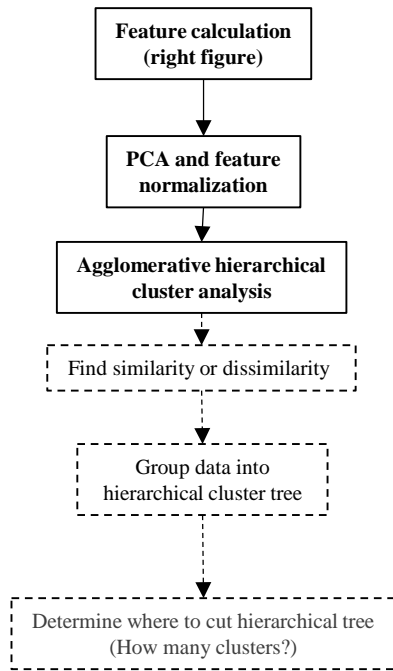
analyses, damage mechanisms were assigned to the clusters. The following sub-sections explain analysis methods in this paper.

3.4.1 Unsupervised pattern recognition

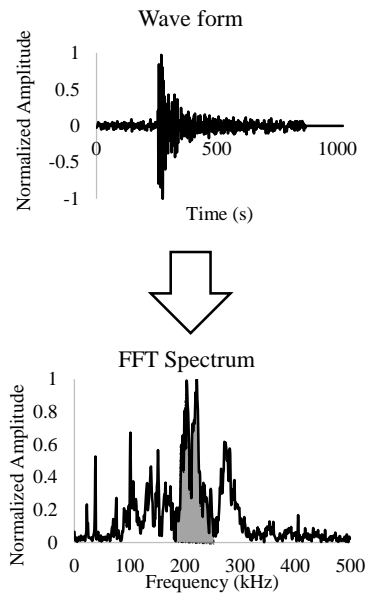
Unsupervised pattern recognition is a data-driven method which is used to discriminate unlabeled multidimensional data into potential existing clusters. The data in each cluster share homogeneous characteristics [42]. In this study, an agglomerative hierarchical clustering method was utilized for clustering AE signals based on their frequency content. Each input data is initially assumed to be a cluster. Then, based on a calculated proximity matrix (similarity and dissimilarity), initial clusters are grouped to form a new cluster. The proximity matrix is updated at each merging level. This procedure is repeated for the new clusters and terminated with one final cluster. After forming a dendrogram for all data, the required number of clusters is determined based on the height differences of each link and the neighboring links in the cluster [43]. The procedure is shown in Figure 3.3. In this study, Euclidean distance and Ward's method were utilized for finding distances and a linkage of data, respectively [44].

Frequency-energy based features were derived from each AE signal. AE signals were transferred to the frequency domain using the Fast Fourier Transform (FFT). Then, Fourier magnitude was calculated in terms of frequency. The frequency domain was divided into 10 equal frequency bands, and areas under each band were normalized by the total area under the FFT amplitude spectrum. These values are utilized as clustering features (Figure 3.3a and b). Principle Component Analysis (PCA) was used to reduce the dimension of the input matrix. The first four components, a representative of 93% of

the whole data, were selected as an input matrix for the agglomerative hierarchical clustering algorithm.



(a) Clustering algorithm



(b) Signal feature calculation

Figure 3.3 Clustering approach

3.4.2 Artificial neural network

An artificial neural network (ANN) is a supervised pattern recognition method, which can be utilized when a labeled dataset and history of data are available. ANNs have three primary layers: input, hidden, and output. In the input layer, the data matrix and target matrix are defined. The data matrix includes all observations with their associated features, and the target matrix includes data labels. The algorithm trains a network to reach the target matrix, and results are presented as an output matrix. The most significant layer in ANN is the hidden layer, where an ANN learns relationships between the input data and target layer [45,46]. The schematic architecture of a trained

neural network is presented in Figure 3.4. The network includes one hidden layer with 25 neurons. The data matrix is separated into three data sets; training, validation, and test data. The training data set is utilized for training the network. The validation data is usually selected from the input data to evaluate the network during the training process. This data is utilized to help a network to be generalized for a new dataset. The testing data is an independent data set to test the performance of the trained network [47].

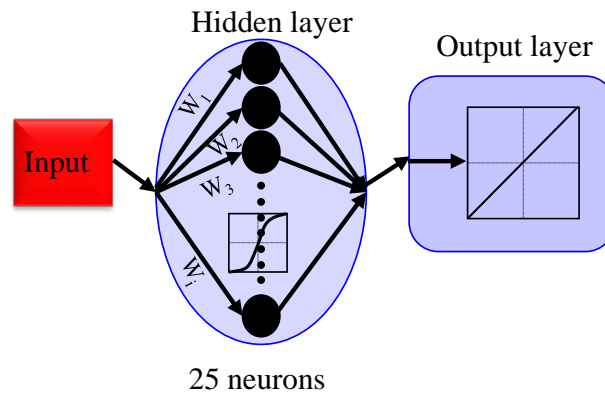
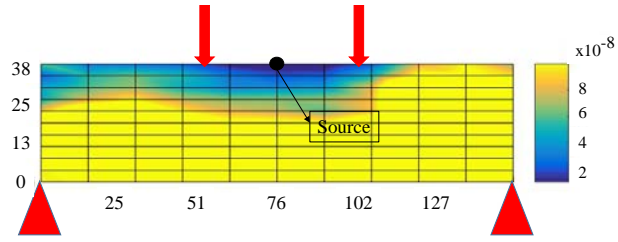
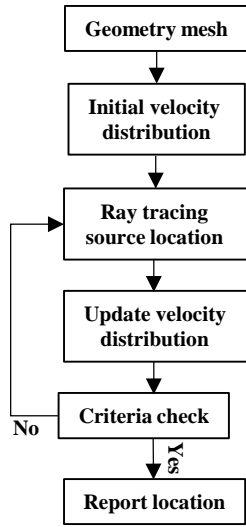


Figure 3.4 Neural network architecture (schematic)

3.4.3 Ray-tracing source location

A MATLAB script was developed for localizing the events recorded during the notched four-point bending test based on the ray-tracing concept [48]. The algorithm and a result example are shown in Figure 3.5.

The first step is to mesh the surface geometry of the beam. In this study, mesh lengths of 15.2 mm (0.6 inch), and 3.81 mm (0.15 inch) were employed along the long and short dimensions of the beam (152 mm and 38.1 mm), respectively. The velocity distribution was initially assumed to be constant within the meshes.



(a) Algorithm

(b) Source location result (dimensions in mm)

Figure 3.5 Ray-tracing approach

Possible emission times between all nodes (intersection of meshes) and sensors, which registered a hit, were calculated based on observed arrival times. Procedure details are explained by Shiotani et al. [49].

$$E_{ij} = T_i - t_{ij} \quad (3.1)$$

Where E_{ij} is a possible emission time between node j and sensor i . t_{ij} is travel time between node j and sensor i , and T_i is an observed arrival time at sensor i .

The average and variance of the calculated possible emission times for all nodes are calculated in accordance with the following equations:

$$\sigma_j = \frac{\sum_{i=1}^N (E_{ij} - m_j)^2}{N} \quad (3.2)$$

$$m_j = \frac{\sum_{i=1}^N E_{ij}}{N} \quad (3.3)$$

In the above equations, N is the total number of sensors which detect an event.

The nodes with the minimum variance are expected to be nearby the real event location.

Therefore, a geometrical average of the coordinates for the nodes with the lowest variances is reported as the source location. Average possible emission time associated with the source location is assumed to be an event emission time.

A residual slowness in each cell is calculated based on the difference between the observed and estimated travel times. Finally, the slowness or velocity matrix is updated by a redistribution of weighted average residual cell slowness [48] [50]. Figure 3.5b shows an example of source localization for one AE event in the four-point bending test. The contour shows the uncertainty in calculating the travel times of the nodes. The lowest uncertainty values present the region with the highest probability of event occurrence.

3.4.4 Wavelet analysis

To present signals in the time-frequency domain, the wavelet transform (WT) is utilized. Contrary to windowed Fourier transforms (WFT), wavelet transforms (WT) present data in a high time resolution for high-frequency components and a high resolution in the frequency domain for low-frequency components. Therefore, wavelets are suitable for presenting AE signals because AE signals are usually characterized by short high-frequency and long low-frequency signal components [51]. The continuous wavelet transform (CWT) is defined according to the following equation:

$$CWT(a, b) = \int S(t) * |a|^{-0.5} \psi \left(\frac{t-b}{a} \right) dt \quad (3.4)$$

Where “*a*” and “*b*” are scale and shift parameters, respectively. The scale parameter governs the compactness or extension of a signal (frequency), and the shift parameter determines the position of a mobile window in the time domain. “*S(t)*” is a signal time history. Eq. (3.5) is referred to as the wavelet, which is the second portion of

Eq. (3.4). Basic window function (without scale and shift parameters) is referred to as the mother wavelet.

$$\Psi_{a,b}(t) = |a|^{-0.5} \Psi\left(\frac{t-b}{a}\right) \quad (3.5)$$

The mother wavelet used in this study is the Gabor wavelet based on a Gaussian function [51]. This wavelet is generally suitable for AE data analysis [52]. The results of wavelet analysis are the wavelet coefficients for the different combinations of time and frequency, which are presented in a contour diagram or spectrogram.

3.4.5 Moment tensor analysis

Moment tensor analysis has been recently utilized to characterize prominent modes of AE sources. Ohtsu [53,54] developed a simplified equation to relate amplitudes of received signals to AE sources by defining a moment tensor of sources. The tensor is second-order, which is defined by six components. The six components can be derived by solving an equation proposed by Ohtsu [53,54] and having at least six sensors registering events. The eigenvalues and eigenvectors of the tensor have information about AE source mechanisms. Direction and fracture modes are determined by decomposing the moment tensor by using eigenvalue analysis [53,54].

3.5 Results and discussion

AE data were recorded during the compression test. Visible cracks started to appear from the top of the specimen due to concentration of stress at the ends of the specimen as shown in Figure 3.6. The AE data caused by compressive loading (at 40% of ultimate capacity) is presented in Figure 3.7. Figure 3.7a illustrates the load curve and AE amplitude in terms of test time and Figure 3.7b shows load and cumulative signal strength (CSS) curves in terms of test time. The jumps in the CSS curve indicate crack



Figure 3.6 Visible cracks at conclusion of compression test

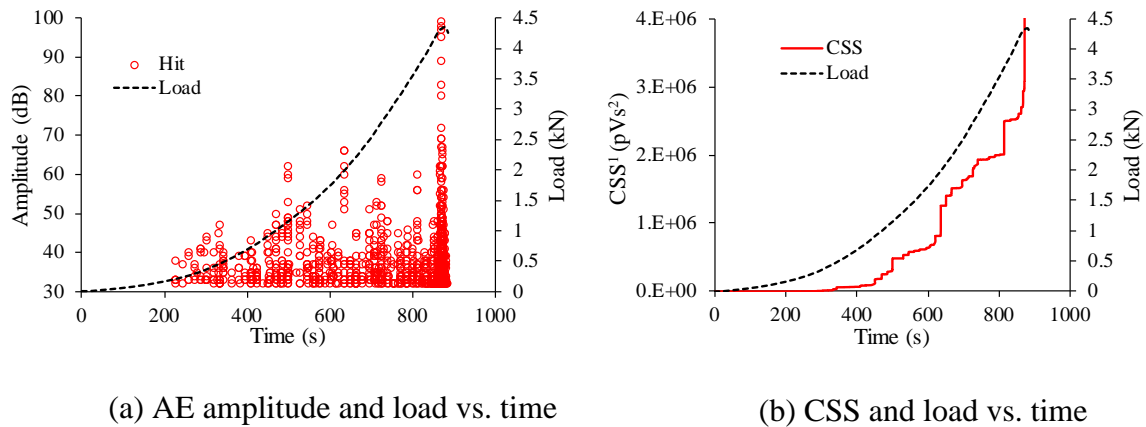


Figure 3.7 Data from compression testing ¹Cumulative signal strength. ²Picovolt.second.

formations, which coincides with the larger AE event amplitudes. The macrocrack formation at the end of the test is indicated in AE data by large-amplitude signals and a jump in CSS at the end of loading (Figure 3.7). The CSS is scaled to 4×10^6 pVs to show curve variation before macrocrack formation. Moreover, the concentration of data at the end of loading (at 849-850 seconds) is denser than the region between 0 to 849 seconds. At the end of loading, a significant number of microcracks occurred and coalesced with

the pre-existing microcracks; resulting in the visible cracks (macrocracks) shown in Figure 3.6.

A moment tensor analysis was conducted on the AE data recorded during the compression test. The result for specimen P-40 is presented in Figure 3.8. The density of events suddenly increased at the end of loading close to the top end of the specimen, where visible cracks were observed. Most of events were in tensile mode, which confirms the failure mechanisms observed in these specimens. The failure mechanism was the formation of vertical cracks which divided the specimens into long vertical pieces [35]. Moreover, the event locations at the end of the test (Figure 3.8) indicate the location of stress concentration and the start of macrocracks. Most of the events were accumulated close to the top end of the specimen.

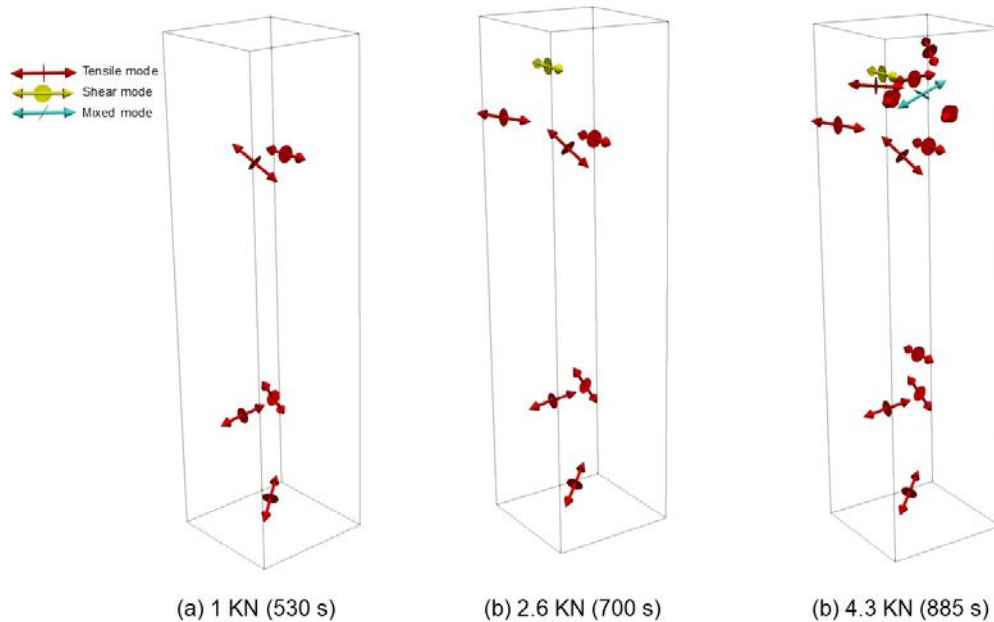
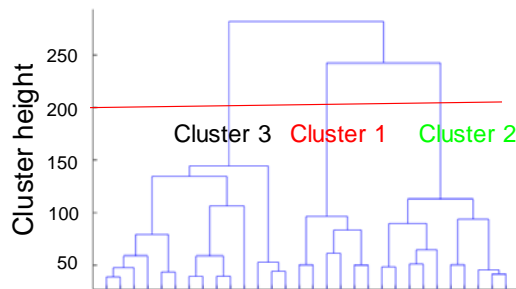


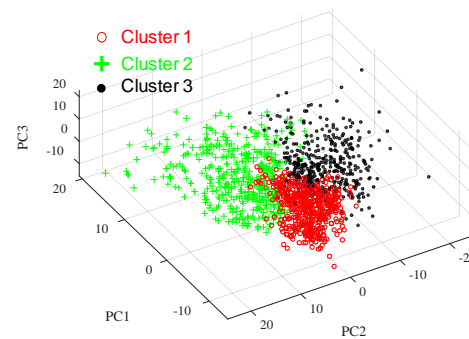
Figure 3.8 Moment tensor analysis for P-40

3.5.1 Clustering of AE data and training

The AE signals in the compression test were clustered through the procedure mentioned in section 3.4.1. The binary cluster tree (dendrogram) was created by the algorithm and is shown in Figure 3.9a. Three clusters were identified by conducting the agglomerative hierarchical algorithm. Their names are Cluster 1, Cluster 2, Cluster 3. The clusters were determined according to the dendrogram and link heights. In Figure 3.9b, the clustered data are presented in terms of the first three principal components.



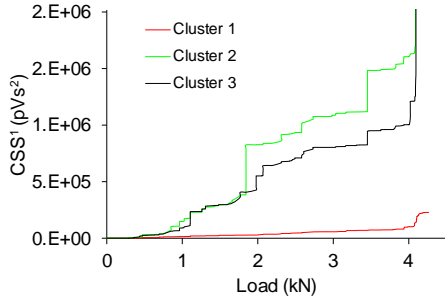
(a) Clustering dendrogram



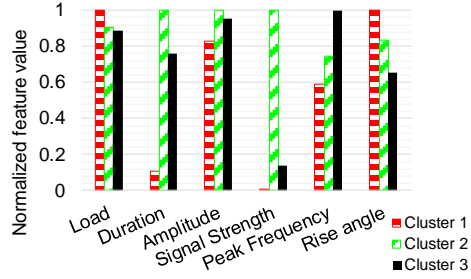
(b) Clustered data in principle component space

Figure 3.9 Clustering of data

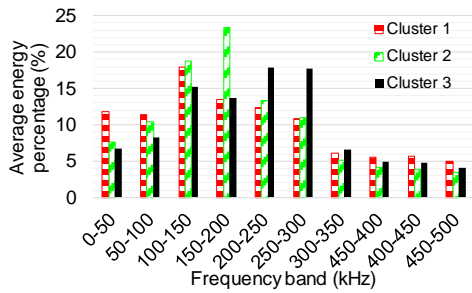
Cumulative signal strength curves versus load for the three clusters are presented in Figure 3.10a. Most of the energy was released through the occurrence of Cluster 2 and Cluster 3. These clusters have average signal strengths higher than cluster Cluster 1, although the number of hits in Cluster 1 exceeds those in Cluster 2 and Cluster 3. Moreover, as seen in Figure 3.10b, duration and amplitude for Cluster 2 and Cluster 3 are greater than for Cluster 1. The reason may be that Cluster 1 includes several weak signals, and most of the signal amplitudes are below the threshold.



(a) Cumulative signal strength in terms of load



(b) Normalized signal features



(c) Average energy percentage

Figure 3.10 Average feature values for clustered data of compression test.
¹Cumulative signal strength. ²Picovolt.second.

The other feature is the rise angle (RA), which is the ratio of rise time to amplitude, and the signal amplitude. This value is normalized in Figure 3.10b. The lower value of RA presents a greater sudden release of energy. RAs for Cluster 2 and Cluster 3 are steeper than for Cluster 1. Most of the features in Figure 3.10b is threshold-dependent and are not efficient for evaluating the characteristics of weak signals. Therefore, the utilization of frequency content and threshold-independent features is required.

The area under each frequency band in the FFT spectrum is divided by the total area under the entire spectrum for all signals in the clusters, and the results are presented in Figure 3.10c. In Cluster 3, a large portion of energy (36%) is in the range of 200 to 300

kHz, and 36% of signal energy is concentrated between 150 to 250 kHz for Cluster 2. Cluster 3 and Cluster 2 are referred to as high-frequency and medium-frequency clusters, respectively. The highest energy concentration in the frequency domain for Cluster 1 appears in the range of 100 to 150 kHz and 23% of its energy occurs below 100 kHz, which is the highest percentage among the clusters. This Cluster is referred to as the low-frequency cluster. Moreover, the average peak frequency of Cluster 3 exceeds that of Cluster 2 and Cluster 2 exceeds Cluster 1 as shown in Figure 3.10b. The examples of waveforms and wavelet energy distributions for the clustered data are shown in Figure 3.11. The amplitudes are normalized to their peaks. The wavelet coefficients for Cluster 1 are higher in the frequencies close to 100 kHz or less. The peak wavelet coefficient for Cluster 2 is approximately at a frequency of 150 kHz, and the high energy region is in the range of 100 to 200 kHz. The largest wavelet coefficients of Cluster 3 initiate at a frequency of 100 kHz and extends beyond a frequency of 300 kHz.

From the above observations, Cluster 1 may be attributed to a coalescence of existing cracks and crack extensions, and Cluster 2 and Cluster 3 can be related to microcrack and macrocrack initiation, due to their high-frequency components, lower rise angles, and concentration in the earlier levels of loading. Low rise angles and high frequencies of AE signals have been related to crack initiation, and low frequencies and high rise angles have been attributed to crack propagation and coalescence [25,36].

Cracking in the compression test happened randomly and scattered in terms of location. Therefore, the AE signals should be related to an experiment with more control on crack opening such as a notched four-point bending test. Furthermore, the cracking mechanism in specimens under compressive loading was dominated by tensile mode as

concluded from the moment tensor analysis and observed from failure mechanism results, and the prominent failure mode in the four-point bending test with a mid-span notch is also expected to be tensile [55].

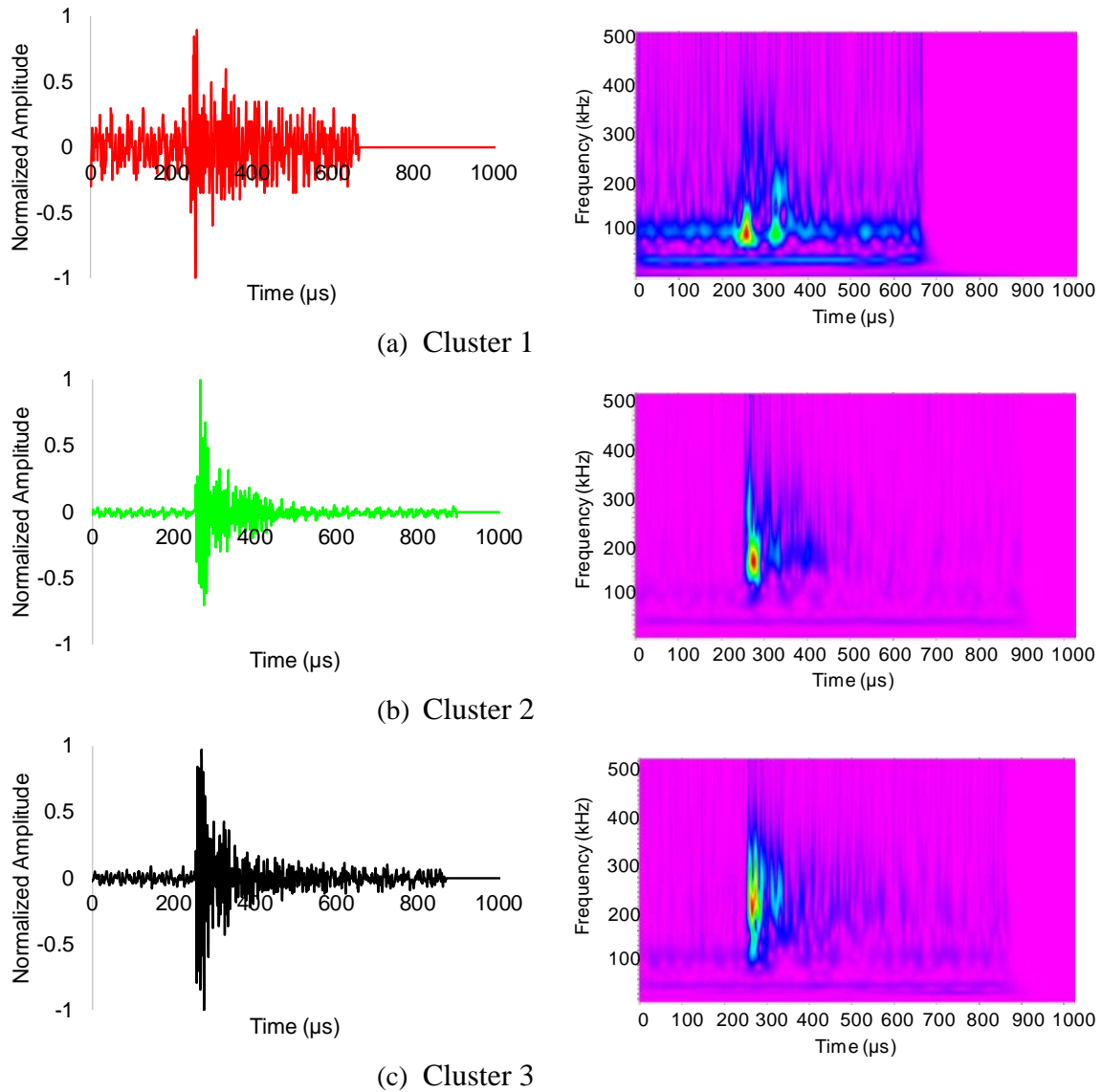


Figure 3.11 Waveform examples for clusters: time history of waves (left), and wavelet energy distributions (right)

Therefore, an ANN was trained based on frequency-dependent features and the resulting clusters from the compression test according to the procedure mentioned in section 3.4.2. The k-fold method was used for cross-validation of the network [56]. In this method, the data is separated into k random subsets. Then, k-2 subsets are merged to form a training set, and two remaining subsets are selected for validation and test data. This procedure is repeated k times, and the average performance of trained networks is evaluated [56]. In this paper, ten subsets were chosen for cross-validation. An average error histogram diagram for the trained neural networks is presented in Figure 3.12 for the training, validation, and test subsets of the input data. The errors were calculated based on the difference between the target and output matrices.

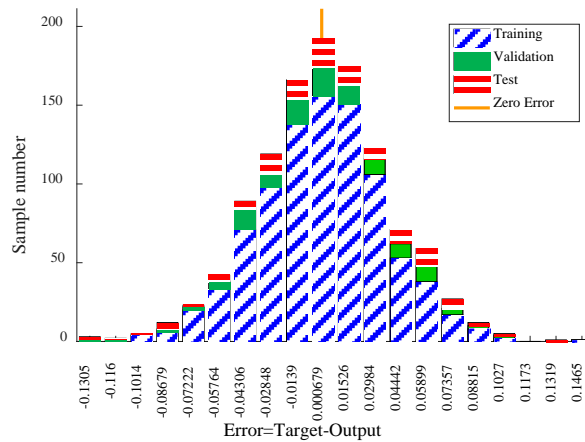


Figure 3.12 Neural network error histogram

The sample errors are concentrated between -0.13 to 0.15. Furthermore, the average mean square errors for the clusters are presented in Table 3.2. Cross-correlation figures for the trained neural networks between outputs and targets matrixes are shown in Figure 3.13 for all data, training, validation, and test data. Regression coefficients, based on consideration of all ten networks, are presented above each of the sub-figures. All

coefficients are close to unity. Although the regression coefficient for the test data is lower than the others (validation and training), the value is still close to unity. According to the error histogram, mean square errors, and cross-correlation figures, it is concluded that the trained ANN has acceptable performance and the capability to recognize the associated clusters even for a randomly-selected dataset such as the test data.

Table 3.2 Average mean square error

	All data	Training	Validation	Test
Cluster 1	0.0080	0.0101	0.0152	0.0180
Cluster 2	0.0114	0.0129	0.0235	0.0236
Cluster 3	0.0082	0.0099	0.0165	0.0196

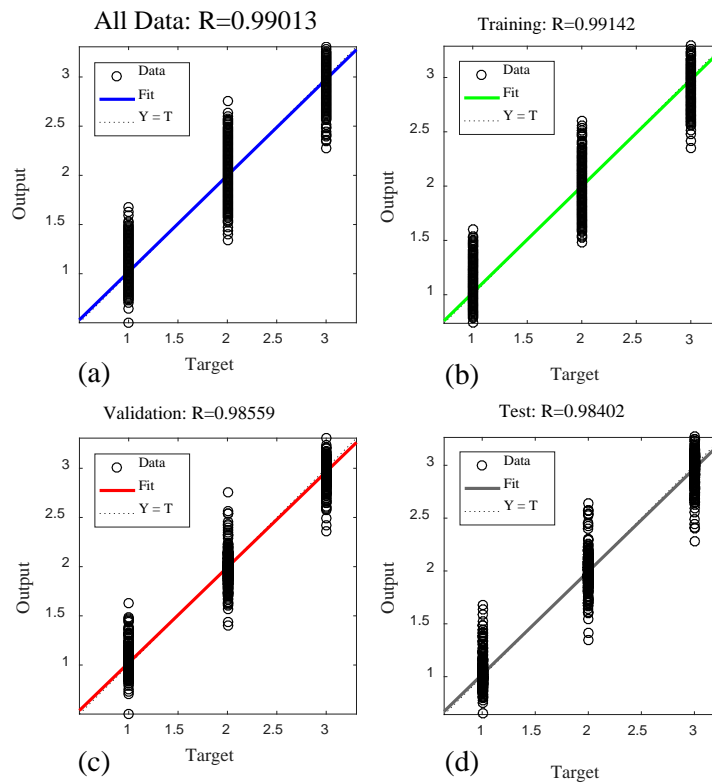


Figure 3.13 Cross-correlation figure between output and target matrix

3.5.2 Applying trained ANN for notched four-point bending test

AE data were also collected during flexural loading as discussed in the previous section. The frequency-dependent features were derived from the signals, and the trained ANN was utilized for classifying the resulting signals. The statistical feature analysis of clustered data is shown in Fig. 14. Both non-frequency and frequency-dependent features approximately follow the trend observed in the compression test.

As shown in Fig. 14, 31% of signal energy for Cluster 3 is in the range of 200-300 kHz. This cluster is high-frequency. In Cluster 2, 35% of the energy concentrates between 150 to 250 kHz. This cluster contains medium-frequency signals. The highest energy portion ratio for the low-frequency range (0-100 kHz) is 23%, which is attributed to Cluster 1 (low-frequency cluster). The highest average peak frequency is related to Cluster 3, and the lowest is associated with Cluster 1. Moreover, as for the compression test, it can be observed that the signals with higher frequency components (Cluster 3) have the lowest rise angles.

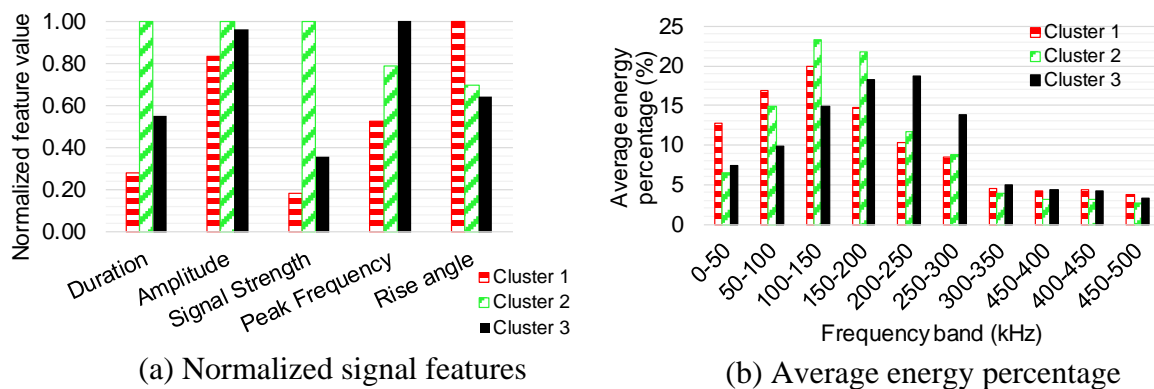
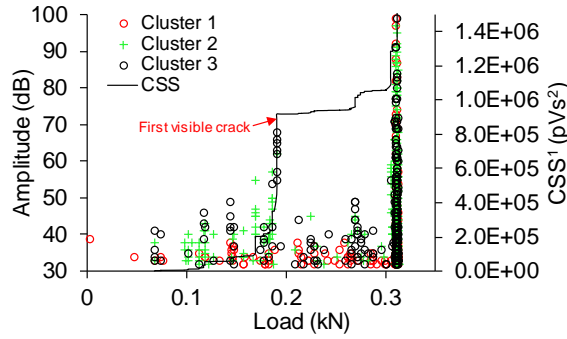
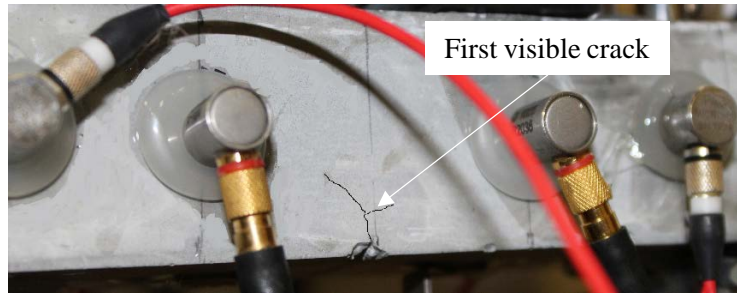


Figure 3.14 Average feature values for clustered data of four-point bending test



(a) Clustered four-point bend AE data



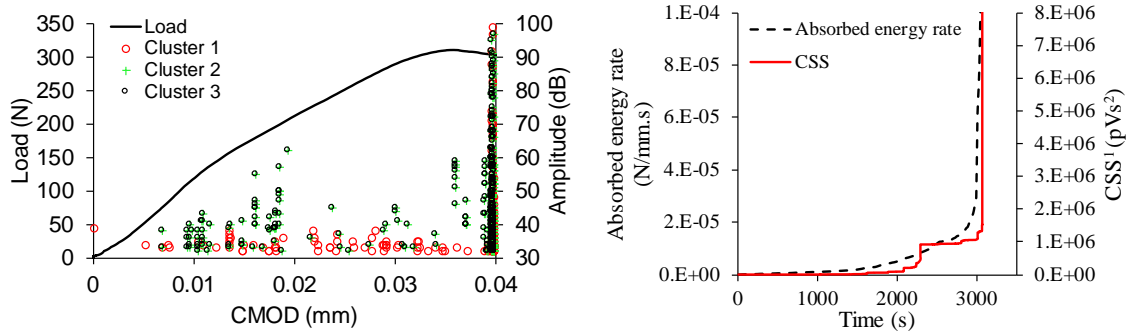
(b) First visible crack

Figure 3.15 AE data from four-point bending test
¹Cumulative signal strength. ²Picovolt second

The amplitude and cumulative signal strength (CSS) for the AE data in terms of load level and classified clusters are shown in Figure 3.15. The CSS curve was scaled to the maximum value of 1,500,000 pVs (picovolt second) to show the CSS evolution prior to failure. The visible crack occurred at a load of 191 N with a large jump in CSS as shown in Figure 3.15a. The AE events occurring before the first visible crack were mostly related to the small-scale cracks (non-visible cracks). Most of the signals in Cluster 3 occurred at the jumps in the CSS curve.

The load-displacement history of the four-point bending test is presented in Figure 3.16. Crack mouth opening displacement (CMOD) was measured by a clip gauge, as shown in Figure 3.2. As seen in Figure 3.16a, the load was monotonically increased

until the maximum load and then softening appeared in the post-peak regime. At the beginning of loading, the slope of the load curve versus CMOD was slightly decreased due to the formation of microcracks which were verified by AE data (Figure 3.16a). The post-peak regime for the cement paste beam was short. After an increase in CMOD in the post-peak region, an unstable crack occurred, and the specimen failed. The cement paste specimen showed very brittle behavior. The fracture energy (post-peak region) was only 18.6% of the entire absorbed energy. This behavior can also be observed from the absorbed energy rate (Figure 3.16b). The absorbed energy increased abruptly with a rise in CMOD in the post-peak regime, due to an occurrence of an unstable crack. Moreover, CSS was correlated to the absorbed energy rate. A significant CSS jump occurred at the same time as the large absorbed energy rate, and the unstable crack occurred.



(a) Load and AE data in terms of CMOD

(b) Absorbed energy rate and CSS in term of CMOD

Figure 3.16 Fracture curves (¹Cumulative signal strength. ²Picovolt. second)

To further analyze the AE data, AE events were localized in the beam specimen using the ray-tracing algorithm explained in section 3.4.3. The focus of the analysis is the events which were localized in the mid-span and close to the notch location. The ray-

tracing algorithm was utilized due to its expected accuracy. Due to the inherent heterogeneous characteristic of cementitious material, the velocity of elastic waves is not constant in different emission directions. Therefore, using an algorithm to consider directional velocity diversity is necessary for source location. The results of the source location.

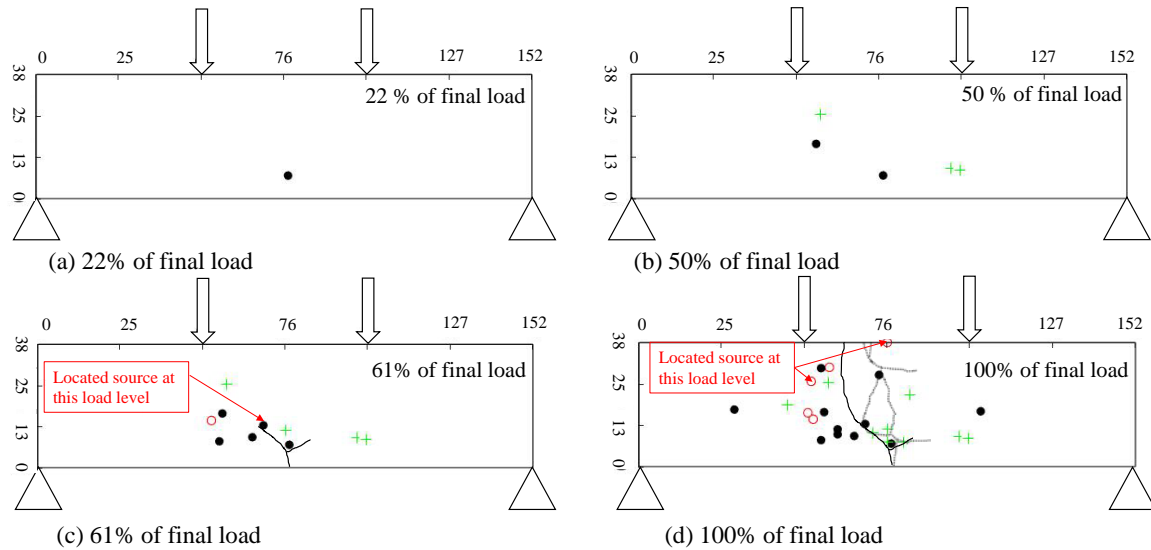


Figure 3.17 Source location in terms of load level

are presented in Figure 3.17.

The continuous black lines illustrate cracks in the front face of the beam and dotted lines illustrate the cracks at the back of the beam. The shape of dots (events) are based on their associated clusters (e.g., red empty circle, green plus symbol, and black dots are related to Cluster1, Cluster 2, and Cluster3, respectively). In Figure 3.17c, an event which occurred at 61% of the final load is shown by an arrow. At this load level, the first visible crack was observed. In Figure 3.17d, two events (which occurred at the final load) were marked by arrows. The first located event occurred at 22% of the final load and had high-frequency components in its FFT spectrum (Cluster 3). As the load

increased, a combination of green and black clusters (Cluster 2 and Cluster 3) appeared. The red events (related to Cluster 1) started to occur at 61% of the final load but mostly occurred after 90% of the ultimate load.

From the observations mentioned above, it is postulated that high-frequency AE signals in plain cement paste occurred when cracks were not already formed in the specimen, and the specimen was intact in the location of crack formation. Cracking in this condition released more energy and was more sudden than low-frequency events. When cracks were already formed in the specimen, smaller energy was required for a crack to propagate in the same location. Therefore, the low-frequency signals (Cluster 1) can be assigned to the propagation and coalescence of cracks, and the higher frequency signals (Cluster 2 and Cluster 3) can be attributed to the crack initiation.

The clusters in the compression test can be attributed to the cracking mechanisms similar to the clusters for the four-point bending test since these tests were related using the neural network. Crack initiation, extension, and coalescence appeared simultaneously and more randomly throughout the specimen under the compressive load due to concentration of stress at the ends and brittleness of the cement paste. However, cracking mechanisms in the compression test were mostly controlled by tensile mode similar to four-point bending due to the large aspect ratio. Therefore, AE data in the compression test can be attributed to the data in the four-point bending test.

3.6 Conclusions

In this study, a combination of unsupervised and supervised pattern recognition was employed to relate the crack formation mechanisms of a cement paste prism under a compression test to a more controlled test, i.e., notched four-point bending. The ray-

tracing algorithm was utilized for a source location of AE events. The following conclusions may be drawn:

- The cement paste specimen showed brittle behavior during the four-point bending test. The post-peak regime in the load-CMOD curve is narrow. The fracture energy of the cement paste is very low compared to the absorbed energy (18.6% of the total, energy). Moreover, a correlation between CSS and absorbed energy rate can be observed. The CSS and absorbed energy rate showed a large jump at the end of loading in the post-peak regime due to the propagation of an unstable crack.
- The cracking mechanisms in the compression test were governed by tensile mode due to a large aspect ratio of the specimens. It is confirmed by the results of the moment tensor analysis and observing the failure mechanism of the compression test.
- The cluster with the highest frequency components (Cluster 3), initiates at the beginning of the four-point bending. The potential mechanism assigned to the cluster is microcrack initiation. The cluster with the lower frequency components in the FFT spectrum occurred when cracks were already formed in the specimen, and near the end of loading. Therefore, this cluster may be assigned to propagation and coalescence of cracks.
- There is a correlation between frequency and non-frequency dependent features of AE signals. The AE signals with the higher frequency components have larger signal strength and lower rise angles compared to the AE signals with the lower frequency components. This is also supported by observing the CSS curve. The

jumps in the cumulative signal strength are mostly due to the signals with higher frequency components (Cluster 2 and Cluster 3).

- The located events using the ray-tracing algorithm approximately match the observed crack path. This result is achieved by employing the capability of the algorithm to consider diverse elastic wave velocities in different emission directions. The observed error is caused by scattering of the waves due to damage concentration in the midspan.

Acknowledgments: This research was partially supported by the U.S. Department of Energy Office of Science, Office of Basic Energy Sciences and Office of Biological and Environmental Research under Award Number DE-SC-00012530, and by the U.S Department of Energy-Nuclear Energy University Program (NEUP) under the contract DE-NE0008544.

3.7 References

1. Pease, B. Influence of concrete cracking on ingress and reinforcement corrosion. PhD Thesis, Technical University of Denmark, Lyngby, Denmark, 2010.
2. Li, X.; Li, D.; Xu, Y. Modeling the effects of microcracks on water permeability of concrete using 3d discrete crack network. *Composite Structures* **2019**, *210*, 262-273.
3. Van Hung, N.; Hung, V.V.; Viet, T.B. In *The effect of crack width on the service life of reinforced concrete structures*, IOP Conference Series: Earth and Environmental Science, 2018; IOP Publishing: p 012044.
4. Gérard, B.; Breyse, D.; Ammouche, A.; Houdusse, O.; Didry, O. Cracking and permeability of concrete under tension. *Materials Structures* **1996**, *29*, 141-151.

5. Aldea, C.-M.; Shah, S.P.; Karr, A. Effect of cracking on water and chloride permeability of concrete. *Journal of materials in civil engineering* **1999**, *11*, 181-187.
6. Banthia, N.; Biparva, A.; Mindess, S. Permeability of concrete under stress. *Cement Concrete Research* **2005**, *35*, 1651-1655.
7. Aldea, C.-M.; Shah, S.P.; Karr, A. Permeability of cracked concrete. *Materials and structures* **1999**, *32*, 370-376.
8. Liu, H.; Zhang, Q.; Gu, C.; Su, H.; Li, V.C. Influence of micro-cracking on the permeability of engineered cementitious composites. *Cement Concrete Composites* **2016**, *72*, 104-113.
9. Kim, M.O.; Bordelon, A.C.; Lee, N.K. Early-age crack widths of thin fiber reinforced concrete overlays subjected to temperature gradients. *Construction and Building Materials* **2017**, *148*, 492-503.
10. Molero, M.; Aparicio, S.; Al-Assadi, G.; Casati, M.; Hernández, M.; Anaya, J. Evaluation of freeze–thaw damage in concrete by ultrasonic imaging. *NDT & E International* **2012**, *52*, 86-94.
11. Assi, L.; Soltangharai, V.; Anay, R.; Ziehl, P.; Matta, F. Unsupervised and supervised pattern recognition of acoustic emission signals during early hydration of portland cement paste. *Cement and Concrete Research* **2017**.
12. Xi, X.; Yang, S. Time to surface cracking and crack width of reinforced concrete structures under corrosion of multiple rebars. *Construction and Building Materials* **2017**, *155*, 114-125.

13. Abdelrahman, M.; ElBatanouny, M.K.; Ziehl, P.; Fasl, J.; Larosche, C.J.; Fraczek, J. Classification of alkali–silica reaction damage using acoustic emission: A proof-of-concept study. *Construction and Building Materials* **2015**, *95*, 406-413.
14. Tragazikis, I.K.; Dassios, K.G.; Exarchos, D.A.; Dalla, P.T.; Matikas, T.E. Acoustic emission investigation of the mechanical performance of carbon nanotube-modified cement-based mortars. *Construction and Building Materials* **2016**, *122*, 518-524.
15. Hlobil, M.; Šmilauer, V.; Chanvillard, G. Micromechanical multiscale fracture model for compressive strength of blended cement pastes. *Cement and Concrete Research* **2016**, *83*, 188-202.
16. Spooner, D.; Pomeroy, C.; Dougill, J. Damage and energy dissipation in cement pastes in compression. *Magazine of Concrete Research* **1976**, *28*, 21-29.
17. Abou-Zeid, M.; Fowler, D.W.; Nawy, E.G.; Allen, J.H.; Halvorsen, G.T.; Poston, R.W.; Barlow, J.P.; Hansen, W.; Rhoads, R.J.; Brander, M.E. Control of cracking in concrete structures. *Report, ACI Committee* **2001**, *224*, 12-16.
18. Rahman, R.O.A.; Rakhimov, R.Z.; Ojovan, M.I.; Rakhimova, N.R. *Cementitious materials for nuclear waste immobilization*. John Wiley & Sons: 2014.
19. Closure, S.R.R.; Authority, W.D. Performance assessment for the saltstone disposal facility at the savannah river site. *Savannah River Remediation LLC, Aiken, SC, SRR-CWDA-2009-00017 Revision 0* **2009**.
20. Gérard, B.; Breyse, D.; Ammouche, A.; Houdusse, O.; Didry, O. Cracking and permeability of concrete under tension. *Materials and Structures* **1996**, *29*, 141-151.

21. Landis, E.N.; Nagy, E.N.; Keane, D.T. Microstructure and fracture in three dimensions. *Engineering Fracture Mechanics* **2003**, *70*, 911-925.
22. Landis, E.N.; Nagy, E.N. Three-dimensional work of fracture for mortar in compression. *Engineering Fracture Mechanics* **2000**, *65*, 223-234.
23. Elaqra, H.; Godin, N.; Peix, G.; R'Mili, M.; Fantozzi, G. Damage evolution analysis in mortar, during compressive loading using acoustic emission and x-ray tomography: Effects of the sand/cement ratio. *Cement and Concrete Research* **2007**, *37*, 703-713.
24. Loo, Y. Propagation of microcracks in concrete under uniaxial compression. *Magazine of Concrete Research* **1995**, *47*, 83-91.
25. Kong, B.; Wang, E.; Li, Z.; Wang, X.; Niu, Y.; Kong, X. Acoustic emission signals frequency-amplitude characteristics of sandstone after thermal treated under uniaxial compression. *Journal of Applied Geophysics* **2017**, *136*, 190-197.
26. Landis, E.N. Micro–macro fracture relationships and acoustic emissions in concrete. *Construction and Building Materials* **1999**, *13*, 65-72.
27. Ohtsu, M.; Watanabe, H. Quantitative damage estimation of concrete by acoustic emission. *Construction and Building Materials* **2001**, *15*, 217-224.
28. Watanabe, K.; Niwa, J.; Iwanami, M.; Yokota, H. Localized failure of concrete in compression identified by ae method. *Construction and Building Materials* **2004**, *18*, 189-196.
29. Wu, K.; Chen, B.; Yao, W. Study of the influence of aggregate size distribution on mechanical properties of concrete by acoustic emission technique. *Cement and Concrete Research* **2001**, *31*, 919-923.

30. Chen, B.; Liu, J. Effect of aggregate on the fracture behavior of high strength concrete. *Construction and Building Materials* **2004**, *18*, 585-590.
31. Tschegg, E.K.; Schneemayer, A.; Merta, I.; Rieder, K.A. Energy dissipation capacity of fibre reinforced concrete under biaxial tension–compression load. Part ii: Determination of the fracture process zone with the acoustic emission technique. *Cement and Concrete Composites* **2015**, *62*, 187-194.
32. Carpinteri, A.; Corrado, M.; Lacidogna, G. Heterogeneous materials in compression: Correlations between absorbed, released and acoustic emission energies. *Engineering Failure Analysis* **2013**, *33*, 236-250.
33. Guzmán, C.; Torres, D.; Hucailuk, C.; Filipussi, D. Analysis of the acoustic emission in a reinforced concrete beam using a four points bending test. *Procedia Materials Science* **2015**, *8*, 148-154.
34. Sagar, R.V.; Prasad, R.; Prasad, B.R.; Rao, M. Microcracking and fracture process in cement mortar and concrete: A comparative study using acoustic emission technique. *Experimental Mechanics* **2013**, *53*, 1161-1175.
35. Anay, R.; Soltangharaei, V.; Assi, L.; DeVol, T.; Ziehl, P. Identification of damage mechanisms in cement paste based on acoustic emission. *Construction and Building Materials* **2018**, *164*, 286-296.
36. Lacidogna, G.; Piana, G.; Carpinteri, A. Acoustic emission and modal frequency variation in concrete specimens under four-point bending. *Applied Sciences* **2017**, *7*, 339.

37. Calabrese, L.; Campanella, G.; Proverbio, E. Use of cluster analysis of acoustic emission signals in evaluating damage severity in concrete structures. *Journal of Acoustic Emission* **2010**, *28*.
38. Farhidzadeh, A.; Mpalaskas, A.C.; Matikas, T.E.; Farhidzadeh, H.; Aggelis, D.G. Fracture mode identification in cementitious materials using supervised pattern recognition of acoustic emission features. *Construction and Building Materials* **2014**, *67*, 129-138.
39. ASTM, C. 305, standard practice for mechanical mixing of hydraulic cement pastes and mortars of plastic consistency. *ASTM International* **1999**.
40. Dixon, K.; Harbour, J.; Phifer, M. *Hydraulic and physical properties of saltstone grouts and vault concretes*; SRS (US). Funding organisation: US Department of Energy (United States): 2008.
41. Hsu, N. Characterization and calibration of acoustic emission sensors. *Mater. Eval.* **1981**, *39*, 60-68.
42. Everitt, B.S. *An r and s-plus® companion to multivariate analysis*. Springer Science & Business Media: 2006.
43. Tan, P.N.; Steinbach, M.; Kumar, V. Data mining cluster analysis: Basic concepts and algorithms. *Introduction to data mining* **2013**.
44. Murtagh, F.; Legendre, P. Ward's hierarchical agglomerative clustering method: Which algorithms implement ward's criterion? *Journal of classification* **2014**, *31*, 274-295.

45. Solomatine, D.; See, L.M.; Abraham, R. Data-driven modelling: Concepts, approaches and experiences. In *Practical hydroinformatics*, Springer: 2009; pp 17-30.
46. Sobieszcanski-Sobieski, J.; Morris, A.; van Tooren, M.J.; La Rocca, G.; Yao, W. Guided random search and network techniques. *Multidisciplinary Design Optimization Supported by Knowledge Based Engineering* **2015**, 80-97.
47. Gavin, H. The levenberg-marquardt method for nonlinear least squares curve-fitting problems. 2011.
48. Kobayashi, Y.; Shiotani, T. Computerized ae tomography. In *Innovative ae and ndt techniques for on-site measurement of concrete and masonry structures*, Springer: 2016; pp 47-68.
49. Shiotani, T.; Nishida, T.; Nakayama, H.; Asaue, H.; Chang, K.-C.; Miyagawa, T.; Kobayashi, Y. Fatigue failure evaluation of rc bridge deck in wheel loading test by ae tomography. In *Advances in acoustic emission technology*, Springer: 2017; pp 251-264.
50. Schubert, F. Basic principles of acoustic emission tomography. *Journal of Acoustic Emission* **2004**, 22, 147-158.
51. Suzuki, H.; Kinjo, T.; Hayashi, Y.; Takemoto, M.; Ono, K.; Hayashi, Y. Wavelet transform of acoustic emission signals. *Journal of Acoustic Emission* **1996**, 14, 69-84.
52. Ni, Q.-Q.; Iwamoto, M. Wavelet transform of acoustic emission signals in failure of model composites. *Engineering Fracture Mechanics* **2002**, 69, 717-728.

53. Ohtsu, M. Acoustic emission theory for moment tensor analysis. *Research in Nondestructive Evaluation* **1995**, 6, 169-184.
54. Ohtsu, M. Moment tensor analysis. In *Acoustic emission testing*, Springer: 2008; pp 175-200.
55. Yin, Y.; Qiao, Y.; Hu, S. Four-point bending tests for the fracture properties of concrete. *Engineering Fracture Mechanics* **2019**.
56. Refaeilzadeh, P.; Tang, L.; Liu, H. Cross-validation. In *Encyclopedia of database systems*, Springer: 2009; pp 532-538.

Chapter 4

Damage Mechanism Evaluation of Large-scale Concrete Structures

Affected by Alkali-silica Reaction Using Pattern Recognition¹

¹ Vafa Soltangharai, Rafal Anay, Nolan W. Hayes, Lateef Assi, Yann Le Pape, Zhongguo John Ma, and Paul Ziehl. (2018), Damage mechanism evaluation of large-scale concrete structures affected by alkali-silica reaction using pattern recognition. *Applied Science*, 8 (11), p.2148. Reprinted here with permission of publisher.

4.1 Abstract

Alkali-silica reaction has caused damage to concrete structures, endangering structural serviceability and integrity. This is of concern in sensitive structures such as nuclear power plants. In this study, acoustic emission (AE) was employed as a structural health monitoring strategy in large-scale, reinforced concrete specimens affected by alkali-silica reaction with differing boundary conditions resembling the common conditions found in nuclear containments. An agglomerative hierarchical algorithm was utilized to classify the AE data based on energy-frequency based features. The AE signals were transferred into the frequency domain and the energies in several frequency bands were calculated and normalized to the total energy of signals. Principle component analysis was used to reduce feature redundancy. Then the selected principal components were considered as features in an input of the pattern recognition algorithm. The sensor located in the center of the confined specimen registered the largest portion of AE energy release, while in the unconfined specimen the energy is distributed more uniformly. This confirms the results of the volumetric strain, which shows that the expansion in the confined specimen is oriented along the thickness of the specimen.

Keywords: Alkali-silica reaction; acoustic emission; pattern recognition; confinement; damage evaluation

4.2 Introduction

Alkali-silica reaction (ASR) is a chemical processes that has caused damage in concrete structures such as bridges [1-4], nuclear power plants [5-9], and concrete dams [5,10]. This reaction usually occurs between alkali hydroxides in the pore solution and

the reactive silica in some aggregates. The result is an alkali-silica gel, which is hygroscopic and imbibes water and humidity. The gel expands in humidity exceeding 80% [6]. This expansion induces pressure on the concrete matrix and aggregates and causes micro-cracks and cracks when the pressure exceeds the tensile strength of the concrete [11,12]. Several traditional methods such as visual inspection, coring, and petrographic analysis have been utilized for monitoring and identifying the behavior of damage caused by ASR. Visual inspection is very subjective and depends on experience [13]. In addition, damage can only be detected by using this method, once it has reached the surface. Coring is a destructive method, which is discouraged in sensitive structures like nuclear power plants. Moreover, it is difficult to generalize the global condition of structures through evaluation of a few cores. Petrographic analysis is also mostly dependent on the experience of the examiner, is likewise a destructive method, and is costly and time-consuming. Linking the micro-state of the material examined to the condition of the entire structure using petrographic analysis is difficult [11], although this is an active research area (RILEM TC-259). Therefore, to monitor structures affected by ASR, non-destructive and global/semi-global methods are attractive. Acoustic emission (AE) is a health monitoring approach which acts as a passive receiver to record internal activities in structures. This method is capable of continuous monitoring which is not the case with most traditional methods. In addition, AE sensors are very sensitive and can capture signals due to micro-scale defect formations coming from the internal regions of structures rather than only those at the surface [14,15]. Several studies have been conducted to evaluate the use of AE in detecting the damage in concrete caused by ASR in the laboratory [11,16-19].

Lokajíček et al. [16] employed ultrasonic sounding and AE to monitor the microstructural changes in mortar bars with different levels of aggregate reactivity. The P-wave velocity increased in the first days of the experiments and then declined abruptly for the specimens with the reactive aggregates. Furthermore, AE cumulative energy indicated the clear difference between the specimens with the reactive aggregates compared to the specimens without any ASR reactivity. Farnam et al. [17] characterized the AE signature for crack formations in aggregates, cement matrix, and interfacial transition zones (ITZ) during alkali-silica reaction using peak frequency and frequency of centroid of the AE signals. The high-frequency signals were assigned to the crack formation in the aggregate, while low-frequency signals were attributed to the crack formation in ITZ and cement matrix. Abdelrahman et al. [11], conducted an accelerated ASR test on concrete prism specimens. A correlation between cumulative signal strength and length change of the prism specimens was identified, and an AE based intensity analysis chart for the classification of ASR damage conditions in correlation with petrographic damage rating indices was developed.

All previously mentioned, research has been focused on ASR-induced damage detection using AE data in small-scale specimens (laboratory scale), which is far from the conditions found in real structures in the field. Furthermore, the stress boundary condition has generally not been taken into consideration in previous studies, while the stress boundary condition has proven to have a large effect on damage distribution in concrete structures affected by ASR [20,21].

In this study, acoustic emission is utilized to monitor the effects of ASR on large-scale, reinforced concrete structures while considering stress induced boundary

conditions in completely plane-confined and partially plane-confined specimens. There are several differences between damage detection of small-scale and large scale structures using acoustic emission. The main challenge with monitoring of small-scale structures using AE is reflections. An example of an ASR study using AE on small-scale specimens was conducted by Abdelrahman et al. [11]. For large-scale structures, attenuation and dispersion of waves are of primary concern. Many sensors with an appropriate layout are needed for damage detection and source localization.

The test specimens were assembled, cured, and monitored at the University of Tennessee, Knoxville, and are part of a test program sponsored by the US DOE Light Water Reactor Sustainability Program. The confined specimen has a complete confinement provided by a rigid steel frame and steel reinforcement meshes. The unconfined specimen has partial confinement provided by steel reinforcement meshes. The specimens without transverse reinforcement resemble construction reminiscent of nuclear power plant containments. An unsupervised pattern recognition algorithm was employed to classify the AE signals based on frequency-energy based features. Different damage mechanisms for the confined and unconfined specimens were identified using AE data.

4.3 Materials and test setup

4.3.1 Specimen and chamber preparation

In this study, three large-scale reinforced concrete blocks were cast. Two specimens were reactive and one was a control specimen (Figure 4.1). Reactive specimens are the specimens that experience expansion due to alkali-silica reaction. Two layers of steel reinforcement mesh were located at the top and bottom surfaces of the

specimens. The reinforcement mesh includes US #11 Grade 60 with a nominal diameter of 36 mm (1.41 inches) at 25 cm (10 inches) spacing (Figure 4.2). The specimens have 7.62 cm (3 inches) cover at top and bottom of the specimens. Moreover, the square steel plates were installed on the ends of the rebar to achieve the full development length in a relatively short distance inside the specimens. For concrete mixture, 350 kg/m³ cement, 175 kg/m³ water, 1180 kg/m³ coarse aggregate, and 728 kg/m³ fine aggregate were used for both reactive and control specimens. The main difference between the specimens was using of NaOH or LiNO₃. In the reactive specimens, 9.8 kg/m³ NaOH solution was added, while in the control specimen 1.9 kg/m³ LiNO₃ was included in the mixture [22].

The coarse aggregates in both control and reactive specimens were greenschist coarse aggregates from North Carolina, which were highly-reactive. Non-reactive manufactured sand and low-alkali Portland cement Type II were also utilized in the concrete mixture. Water to cement weight ratio for both control and reactive specimens was 50%. To increase the alkali content of reactive specimens, 50% sodium hydroxide solution was added to the mixture for reactive specimens. Additionally, a 30% lithium nitrate solution was added to the control specimens to mitigate the ASR effect. More details regarding concrete mixture design was presented by Hayes et al. [22].

The specimens shown in Figure 4.1 have a cubic shape with dimensions of 3.50 m × 3.0 m × 1.0 m (136 inch × 116 inch × 40 inch). There are two reactive specimens; confined and unconfined specimens. A rigid steel brace was utilized to restrain the confined specimen from expanding in the lateral plane. The unconfined specimen does not have a steel brace in its plane. The two reactive specimens resemble the different stress boundary conditions found in real structures. A 1.5 mm layer of polyethylene was

employed between the concrete and the steel frame in the confined specimen to reduce friction. More detailed information about the specimens and steel frame design were presented in Hayes, et al. [22]. In this experiment, the specimens stand on four short, steel columns (76 cm height) to provide access to the bottom of the specimens.

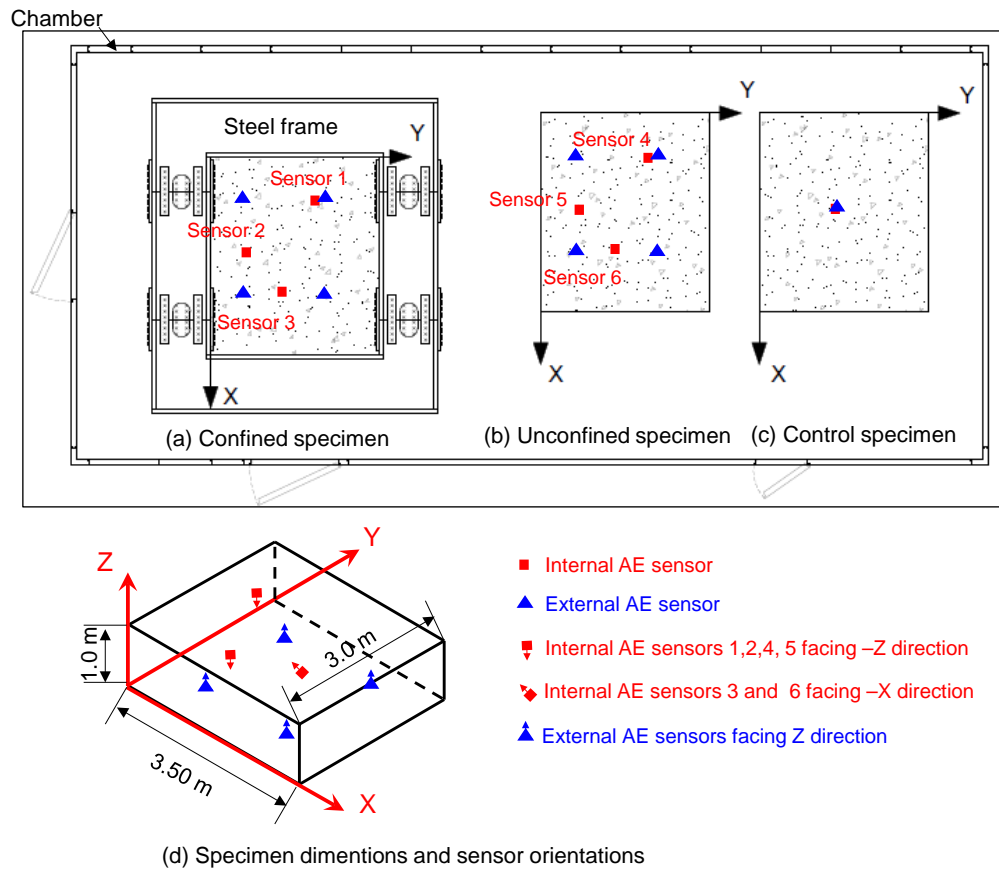


Figure 4.1 Test specimens

Each specimen's formwork was removed 12 days after casting which gave them time for final finishing and concrete setting. After casting, the specimen surfaces were sprayed with curing compound and covered with wet burlap and plastic sheets to reduce moisture loss and cracks from shrinkage during drying. The burlap was kept wet until chamber construction was complete [22].

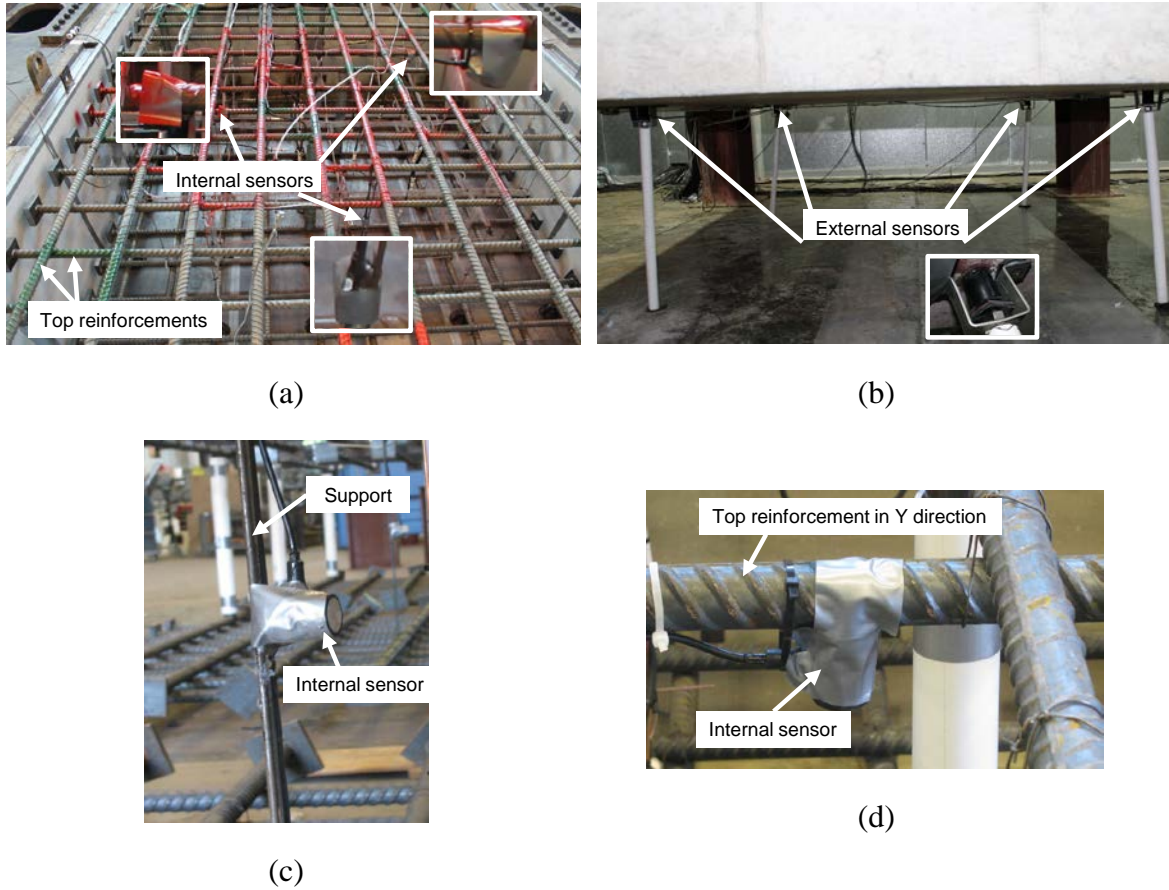


Figure 4.2 Acoustic emission (AE) sensor locations. (a) Internal AE sensors (broadband); (b) External AE sensors (resonant); (c) Internal sensors 3 and 6 installation; (d) Internal sensors 1, 2, 4 and 5 installation.

A large chamber with the dimensions of 16.2 m long, 7.3 m wide, and 3.7 m high was constructed around the specimens to control the temperature and relative humidity of the environment. The chamber was equipped with systems that kept the specimens at the environmental temperature of 38 ± 1 °C and humidity of $95\% \pm 5\%$. The environmental chamber was initiated 26 days after casting and operated continuously except for shutdown for measurements and inspections [22].

4.3.2 Measurement equipment

To measure the strain inside the specimens, two kinds of strain sensors, alkali-tolerant strain transducers (KM-100B from Tokyo Sokki Kenkyujo) and long-gauge fiber optic extensometers (from SMARTECH/Roctest), were employed. In total, sixty-four 100 mm-gauge strain transducers were placed inside the specimens, along with the specimen dimensions. The sensors were fixed on the support fabricated by smooth steel bars with a diameter of 3 mm. Additionally, five high-precision, fiber optic extensometers were installed inside the specimens. The sensors in the X-Y plane had 1.5 m and 1.8 m gauge lengths and were located at the bottom of the specimens. Two fiber optic sensors were installed along the specimen thickness with a gauge length of 0.8 m [22].

Seven acoustic emission sensors were utilized in each of the confined and unconfined specimens (reactive specimens) as shown in Figure 4.1 and Figure 4.2. Two sensors were employed for the control specimen. The internal AE sensors were broadband WDIUC-AST (manufactured by MISTRAS Group, Inc., New Jersey, USA), with an operating frequency range of 200–900 kHz and an internal low-noise 40 dB preamplifier. The external sensors were resonant R6I-UC (manufactured by MISTRAS Group, Inc., New Jersey, USA), with an operating frequency range of 35–100 kHz and an internal 40 dB preamplifier. The special polymer coating on the sensors (internal and external) with an internal waterproof cable makes the sensors insulated, non-conductive, and capable of operating under water.

Three broadband sensors were installed inside the reinforcement cages prior to casting for reactive specimens and one sensor was installed in the control specimen. Sensors 1, 2, 4, and 5 were attached under the second layer of top reinforcement mesh

(under reinforcement in the Y direction) with epoxy and fastened to the rebar by several cable ties and duct tape, with the sensing surface facing downward along the negative Z axis (Figure 4.1d and Figure 4.2d). Sensors 3 and 6 were in the middle of the specimen thickness, with the sensing surface facing toward the negative X axis (Figure 4.1d). Sensors 3 and 6 were attached on the supports by epoxy and duct tape and cables were fastened on the support by cable ties (Figure 4.2c). The supports were fastened to the top and bottom reinforcement meshes. The locations of internal sensors were colored on the top reinforcements to avoid over-vibrating during casting and potentially decoupling the sensors.

Four resonant sensors were attached at the bottom of the reactive specimens and one to the control specimen (Figure 4.2b). The resonant sensors were attached with epoxy on the surface of the concrete and fixed by holders as shown in Figure 4.2b. Internal and external sensors are referred to as broadband and resonant sensors, respectively, in this paper. The holders were made of stainless steel and polyurethane pads were attached between the concrete and the holders to avoid potential corrosion in the holders.

External and internal sensors pose differing technical challenges. Internal sensors are of scientific interest and are not well-suited for implementation in existing structures. One potential technical consideration is the formation of voids around the sensors due to concrete shrinkage. This may result in interruption of data or reduction of sensitivity. Another technical challenge is lack of access after casting. The external sensors are accessible, but decoupling may be a consideration.

A 16-channel Sensor Highway II (SHII), manufactured by MISTRAS Group, Inc. (Princeton Junction, NJ, USA), was utilized as a data acquisition system. The sensitivity of external sensors was checked by applying Hsu-Nielsen sources [23].

The sampling rate was set to 1000 kHz. Pre-trigger time is the period required for data acquisition to save a signal prior to threshold intersection, which was set to 256 μ s. HDT (hit definition time) is the time for which if a signal crosses the threshold the signal will continue until the end of HDT without stopping. HDT was set to 400 μ s. HLT (hit lockout time) is the time defined at the end of a signal for neglecting any reflected signal that exceeds the threshold, which was set to 200 μ s. PDT (peak definition time) is the time which ensures correct identification of the signal peak for rise time and peak amplitude measurements [24]. In this study, PDT was set to 200 μ s. The initial threshold was 32 dB.

4.4 Analysis method

4.4.1 Pattern recognition algorithm

To identify the damage mechanisms in the reactive specimens a pattern recognition algorithm was employed for data classification. Pattern recognition is under the machine learning field and has two major types: unsupervised and supervised. When a background history for a data set is available or the data set has labeled classes, supervised pattern recognition is employed. If there are no labeled classes available, unsupervised pattern recognition can be utilized to identify the potential patterns in the data set based on the selected features.

An agglomerative hierarchical clustering algorithm [25] was employed for classifying the AE data into subsets. The clustering procedure is chronologically

illustrated in Figure 4.3. The first step in the pattern recognition was deriving the frequency-based features for the signals. AE signals were transferred into the frequency domain using the Fast Fourier Transform (FFT). The FFT amplitude spectra were determined for each AE signal and the frequency domain was divided into ten frequency ranges. Then, signal energy in each frequency range was calculated and normalized to the total energy of the signal. These ten signal energies are the signal features. For example, in Figure 4.3a, the area of the hatched region is the energy of the signal in the frequency band from 200 kHz to 250 kHz. This value is normalized to the total energy of the signal, which is the entire area under the FFT spectrum. Principle component analysis (PCA) was used to reduce redundancy in the data. In this analysis, the original data is projected to the new orthogonal coordinates having high variation. An input for PCA is a matrix with the number of columns and rows equal to the feature numbers and the number of hits. Then a variance-covariance matrix for the features was calculated. The coefficients and variance of a specific principle component were calculated by eigenvalue analysis of the variance-covariance matrix. The principal components were selected in a way that represented more than 90% of the entire data. The principal components of the original features were selected as the input features for the pattern recognition algorithm. The algorithm initially calculated the Euclidian distance between the resulting data from PCA analysis. The result was a proximity matrix that contained distances between the original objects (data).

The objects were initially linked together according to calculated distances in the previous step and Ward's method. Ward's method is based on calculating the total within-cluster sum of squares of the data resulting from combining the clusters [25]. In

each level, the data was merged into a binary linkage and the clusters were again merged into new clusters according to the Ward's method. This procedure was continued to form a single cluster which includes all data. The number of the cluster was determined according to the developed dendrogram and the height of each link with respect to the adjacent links [26].

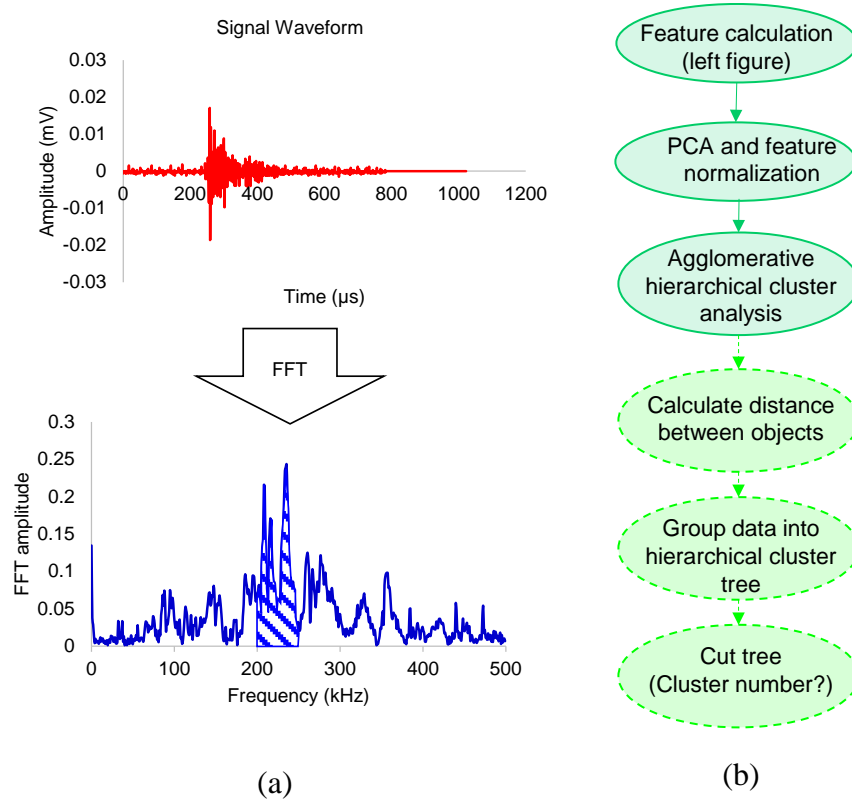


Figure 4.3 Clustering procedure. (a) Energy-frequency based feature extraction; (b) Flow chart of data clustering steps.

4.5 Results and Discussions

The internal strains of the specimens in X, Y, and Z directions were recorded from the casting date. The results are presented up to 200 days in Figure 4.4. The data is presented from 51 days in the figures since external sensors were attached in this day and all the figures in this paper remain in a same time scale for a convenient comparison.

Figure 4.4a shows the average expansion along the specimen dimensions for the reactive specimens and the average volumetric expansions for both reactive and control specimens are presented in Figure 4.4b. The results for volumetric strains show that reactive specimens were expanded. Conversely, the control specimens had no expansion and the internal strain was relatively constant, only showing small shrinkage over time. However, the volumetric strains for both confined and unconfined specimens were very close. This observation indicates that an imposed confinement in the specimens did not influence the expansion of the entire specimens (volumetric strain). Furthermore, the confinement changed the direction of expansion (Figure 4.4a).

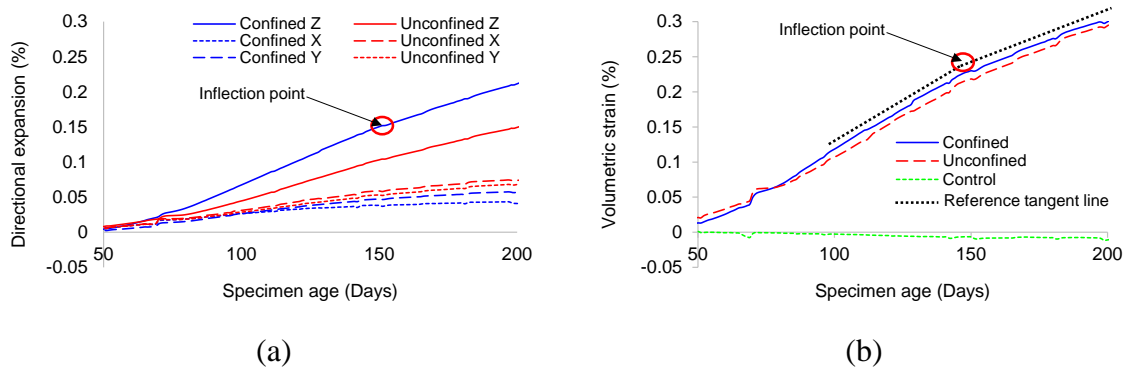


Figure 4.4 Strain distribution of specimens versus concrete age. (a) Directional expansion; (b) Volumetric strain.

Generally, the expansion through the thickness of the reactive specimens (Z direction) is much larger than the expansion throughout the X-Y plane, due to partial or complete confinement in the plane and lack of steel reinforcement through the thickness. The maximum strains in the Z direction for confined and unconfined specimens are approximately 3.6 and 2.1 times the strain in the Y direction, respectively, at 200 days. The steel frame in the confined specimen causes a reduction of both in-plane strains. In the confined specimen, the strain along the X direction is less than the Y direction, while

in the unconfined specimen, the strain along X and Y are almost the same. The strain along the X direction in the confined specimen is 58% of the strain along the X direction in the unconfined specimen at 200 days. However, the strain along the Y direction in the confined specimen is 84% of the strain along the Y direction in the unconfined specimen at 200 days. Moreover, the confinement in X-Y plane for the confined specimen caused an increased strain rate along the Z direction (thickness). The expansion strain rate in terms of time decreases at the point around 150 days, which is named inflection point as seen in Figure 4.4. The inflection point in volumetric strain is considered as one of the important point for ASR modeling, where the curvature of volumetric strain is changed [27,28]. The latency and characteristic times (two modeling parameters) are experimentally determined by knowing the location of inflection point [6,28]. The inflection point is shown in Figure 4.4b and marked in other figures in this paper.

Acoustic emission data was recorded through the internal sensors from the casting day and resonant sensors started recording from the concrete age of 51 days. Filtering AE data is an important step for reducing the amount of non-relevant data for post-processing. The possible sources of false AE data can be friction between the structural components, such as the steel frame and specimens, and water dripping from the chamber ceiling due to high humidity. Two different filtering procedures were developed to minimize the non-genuine data for the internal and external sensors, separately. The filtering is different for the internal and external sensors due to their differences in sensitivity and location. For instance, the internal sensors are much less sensitive than the external sensors and were located inside the specimens, thereby receiving less environmental noise. The AE data below 32 dB and 41 dB for the internal and external

sensors was filtered from the data set. Then, the signals were further filtered using a Swansong filtering procedure [29,30]. This method is based on the observation that genuine AE signals with high amplitude should have long duration and vice versa [11]. Therefore, false signals in this method are categorized by long duration with low amplitude and short duration with high amplitude. The data is presented in terms of duration versus amplitude distribution. Signals which did not comply with the characteristics of genuine signals were deleted based on visual observation of the waveforms. The rejection limits for the internal and external sensors are presented in Table 4.1. In addition, suspicious signals were removed by inspection of waveforms and the chamber activity timetable provided by the University of Tennessee, Knoxville. The filtered AE data from 50 to 195 days after casting for all sensors is presented in Figure 4.5. The figure illustrates the amplitude and cumulative signal strength (CSS) in terms of specimen age. The time window of 50 to 195 days was selected because the highest strain change rate occurred during this period. The gap in the data from 65 to 100 days is missing data due to a difficulty with the data acquisition system caused by an unexpected energy surge. The amount of data in the control specimen is much lower than the data for the reactive specimens. The difference between AE data for the control and reactive specimens is also observable from plots of cumulative signal strength versus time (Figure 4.5). Therefore, the relatively high AE activity for the reactive specimens can likely be associated with expansion caused by the alkali-silica reaction.

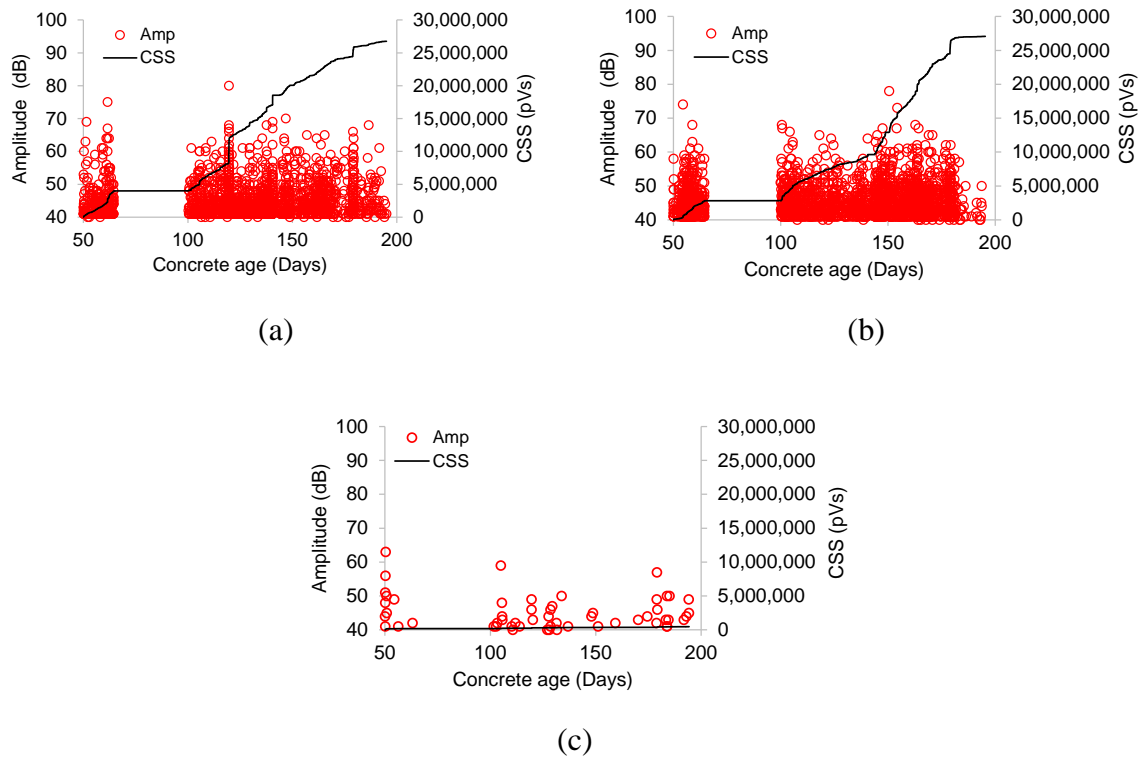


Figure 4.5 Amplitude and cumulative signal strength of AE data in terms of concrete age. (a) Confined specimen; (b) Unconfined specimen; (c) Control specimen.

Table 4.1 Duration-amplitude rejection limits.

External Sensor		Internal Sensor	
Amplitude (dB)	Duration (μ s)	Amplitude (dB)	Duration (μ s)
41–43	400<	32–35	155<
44–45	500<	36–42	260<
46–47	600<	43–100	330<
48–49	650<	-	-
50–53	820<	-	-
54–56	940<	-	-
57–65	1080<	-	-
66–100	1400<	-	-

4.5.1 Acoustic Emission Energy Release

To enable comparisons between the confined and unconfined specimens only AE data recorded by the internal sensors is discussed. These sensors are less sensitive than

the resonant sensors, which results in lower volumes of data. The main reason for choosing the broadband sensors is that their broad frequency response makes them suitable for frequency analysis. The resonant sensors attached on the bottom surface of the specimens are more representative of what may be used in practice for optimized detection and source location. Three dimensional source location of large-scale specimens requires a method to accurately calculate time of arrival for very weak signals, which is a future step of this research. This study involves frequency analysis and therefore focuses on broad band sensors. Analysis of the resonant sensor data is a future consideration.

In Figure 4.1, the red marks and corresponding labels in red font denotes the schematic sensor locations for both confined and unconfined specimens. Sensor coordinates are presented in Table 4.2. The last column of the table represents the coordinates of normal vectors, which are perpendicular to the sensing surfaces of sensors and the directions of vectors are toward the outside of the sensors. The orientation of sensors is shown in Figure 4.1d.

Table 4.2 Sensor coordinates.

Sensor No.	X (m)	Y (m)	Z (m)	\vec{n}
Sensor 1	1.08	1.91	0.86	(0,0,-1)
Sensor 2	1.85	0.78	0.86	(0,0,-1)
Sensor 3	2.34	1.46	0.5	(-1,0,0)
Sensor 4	1.1	1.59	0.86	(0,0,-1)
Sensor 5	1.83	0.88	0.86	(0,0,-1)
Sensor 6	2.36	1.59	0.5	(-1,0,0)

The AE cumulative signal strengths of the internal sensors for the reactive specimens are presented in Figure 4.6a and b. The total CSS versus time for the confined specimen is much higher than the CSS for the unconfined specimen at 195 days (the CSS

for the confined specimen is 2.35 times the value for the unconfined specimen). Moreover, in Figure 4.6a and c, it can be seen that a significant portion of released AE energy is attributed to sensor 3, which is located at mid-height of the confined specimen. The CSS rate for sensor 3 (5805 pVs/Day) is much larger than for sensors 1 and 2 (1545 and 1212 pVs/Day), thereby increasing the difference in the CSS between the sensors. On the other hand, this trend in the confined specimen is not observed in the unconfined specimen where AE energy release is not concentrated in one specific sensor. The distribution of energy was approximately uniform among the sensors. However, the CSS for the sensors at the top reinforcement mesh (sensors 4 and 5) is larger than in sensor 6.

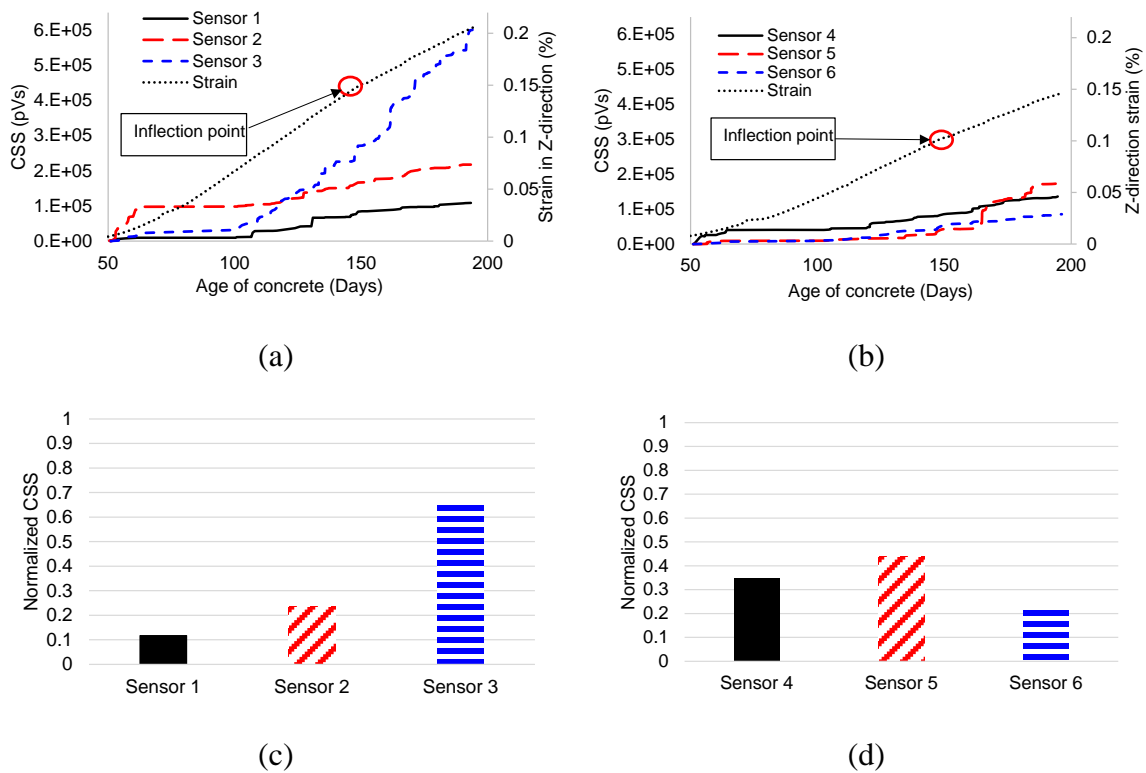


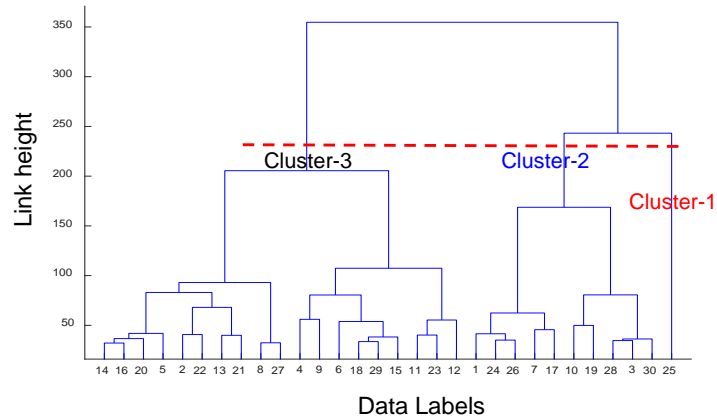
Figure 4.6 Cumulative signal strength (CSS) contribution for sensors. (a) CSS vs. age of concrete for confined specimen; (b) CSS vs. age of concrete for unconfined specimen; (c) Normalized CSS for confined specimen; (d) Normalized CSS for unconfined specimen.

These observations illustrate that the confined specimen has larger AE energy release in the middle layers of the specimen, which is increasing with the progression of the ASR reaction, than the unconfined specimen. This may be due to a larger expansion strain through the thickness of the confined specimen. This large expansion is expected to cause more damage through the thickness of specimen and consequently more AE energy release at middle of the thickness. In the unconfined specimen the crack distribution is expected to be less anisotropic than in the confined specimen. Therefore, it is expected that the AE energy was more uniformly distributed through the thickness of this specimen.

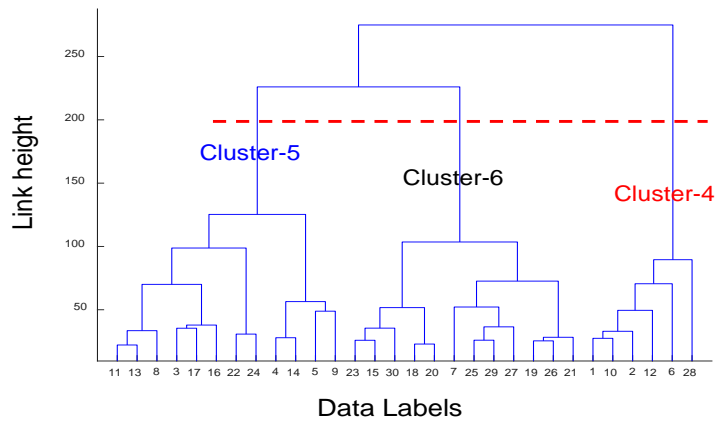
4.5.2 Pattern Recognition of AE Data

The AE signals were classified according to the agglomerative hierarchical algorithm as explained in section 4.4. Dendrograms resulting from the analysis are presented in Figure 4.7. Dashed red lines in the subfigures indicate the desired height of links for clustering. The results of the pattern recognition show three clusters for each reactive specimen (both confined and unconfined). The clusters of confined specimens are indicated by Cluster-1, Cluster-2, and Cluster-3. Accordingly, the clusters of the unconfined specimen are labeled Cluster-4, Cluster-5, and Cluster-6. The horizontal axis in Figure 4.7. gives the data labels, which show either labels of the original data sets (signal number) or the label number of the clusters that resulted from merging the original data. The height of each link shows the distance between the two objects. Each link between two objects is shown by an upside-down U-shaped line in the figure. The data is shown in terms of the first three principal components (PC) to visualize the distribution of clusters with respect to each other in Figure 4.8. Although some signals in

the cluster 5 and 6 were not ideally separated, in general, the clusters indicate a reasonable separation in the PC space (Figure 4.8). The reason for an overlap between clusters 5 and 6 is that some signals in cluster 5 have a similar energy contribution in a specific frequency range to some signals in cluster 6. As seen in Figure 4.9b, clusters 5 and 6 have similar average energy contribution between 250 to 300 kHz.



(a)



(b)

Figure 4.7 Clustering dendrograms. (a) Confined specimen; (b) Unconfined specimen.

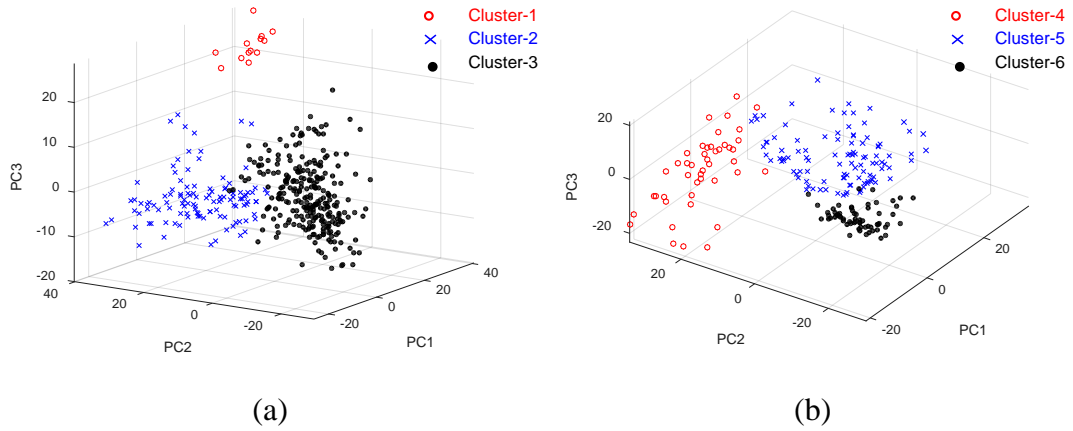
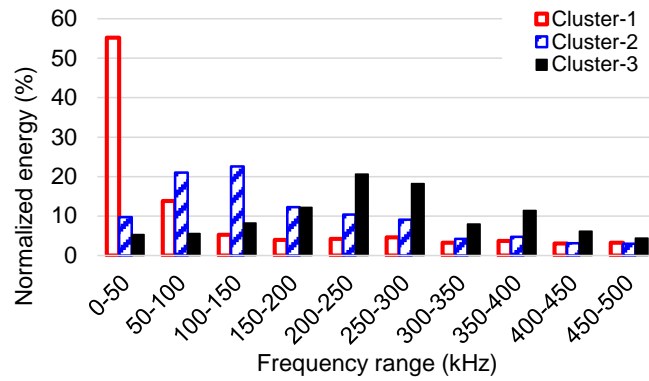
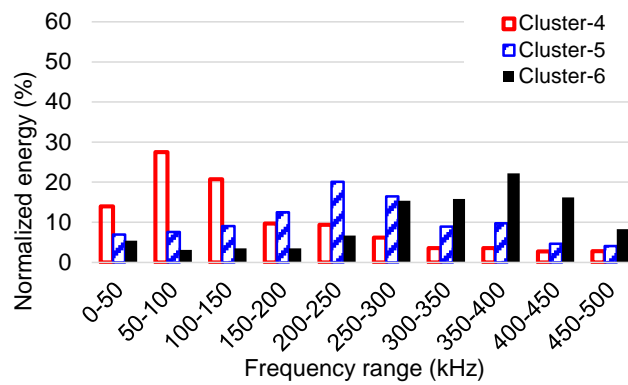


Figure 4.8 Clusters in principle component dimensions. (a) Confined specimen; (b) Unconfined specimen.



(a)



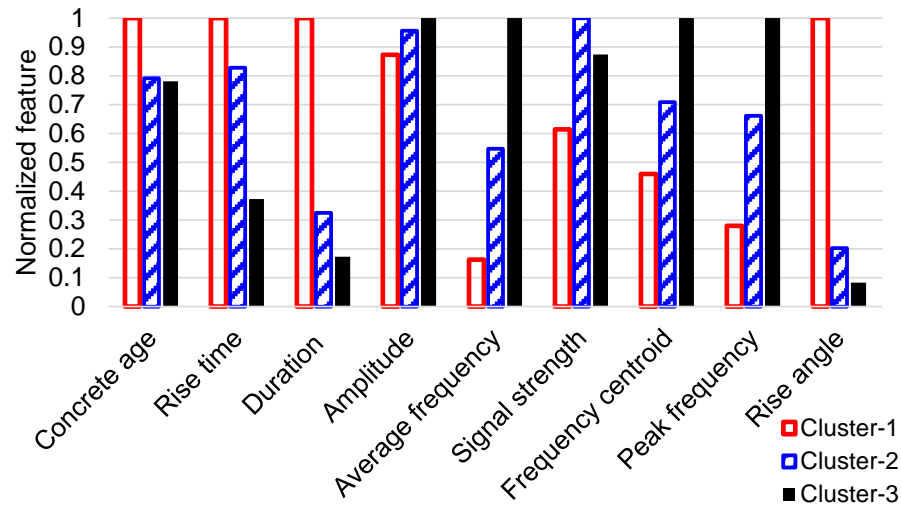
(b)

Figure 4.9 Average normalized signal energy in frequency domain. (a) Confined specimen; (b) Unconfined specimen.

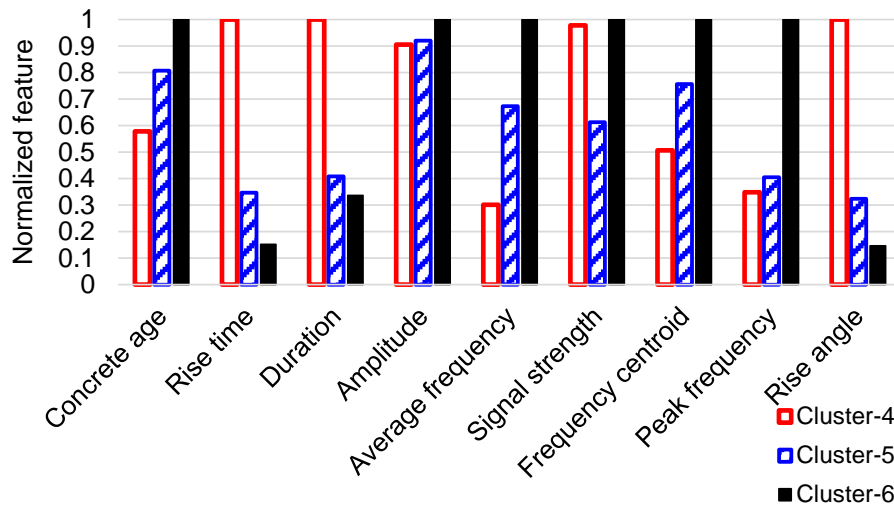
The average energy of signals in terms of frequency ranges is shown in Figure 4.9 for the reactive specimens. These values, as previously mentioned, were calculated using the FFT amplitude spectrum. Afterward, the calculated values were normalized by the total energy of the signal. The average values for each cluster were then calculated. The energy shift to the higher frequency components for the unconfined specimen is apparent when viewed alongside the confined specimen. The clusters in each specimen can be separated based on the frequency content. In the confined specimen, the low-frequency cluster (Cluster-1) has approximately 69% of its energy in a frequency range of 0–100 kHz. The medium-frequency cluster (Cluster-2) has 42% of its energy concentrated in a frequency range of 50–150, while the high-frequency cluster (Cluster-3) has 51% of its energy between 150–300 kHz.

In the unconfined specimen, the low-frequency cluster (Cluster-4) has 62% of its energy in a frequency range of 0–150 kHz and the medium-frequency cluster (Cluster-5) has 49% of its signal energy in the frequency range of 150–300 kHz. The high-frequency cluster (Cluster-6) has 54% of its signal energy concentrated between the frequencies of 300–450 kHz. The Cluster-3 and Cluster-5 share similar frequency content. More signal features for the clusters are illustrated in Figure 4.10. The average feature values for each cluster were normalized by the maximum feature values for each cluster. In the confined specimen, Cluster-1 initiated at a higher concrete age (data was analyzed through a concrete age of 195 days) than clusters with higher frequencies (Cluster-2 and Cluster-3). The average amplitude of the signals in Cluster-3 (the highest frequency) is higher than the other signals. Average signal strength for Cluster-1 is lower than the values for

Cluster-2 and Cluster-3, and duration is higher for the cluster with the lowest frequency content, for example, Cluster-1.



(a)



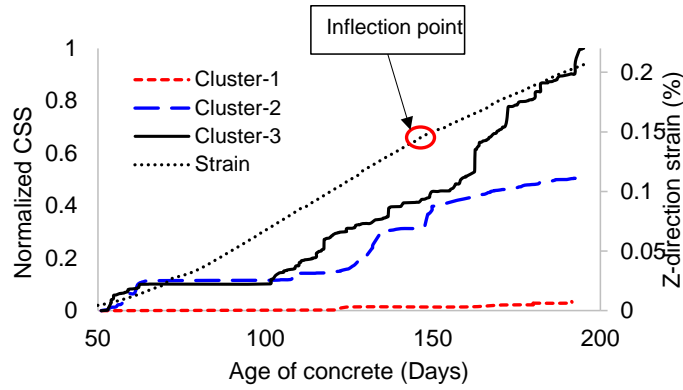
(b)

Figure 4.10 Normalized signal features. (a) Confined specimen; (b) Unconfined specimen.

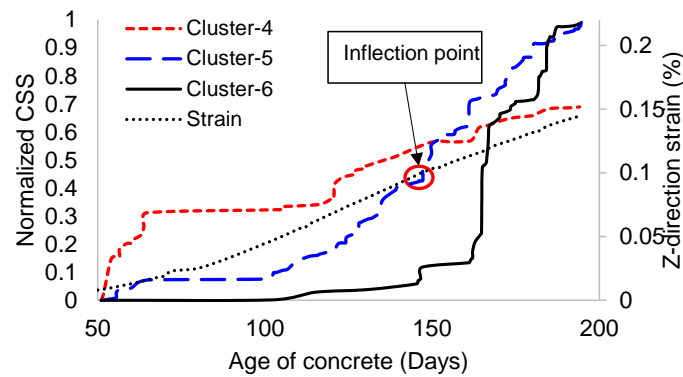
A clear correlation is present between the frequency content of the signal clusters and the rise angle values (rise time over amplitude ratio) as has been observed by other

researchers [31,32]. The higher the frequency components are in a signal, the lower rise angle value the signal possesses. In the unconfined specimen, Cluster-5 and Cluster-6 exhibit higher hit rates at the higher concrete age compared to Cluster-4, and the average amplitude of signals for the clusters with higher frequency components is slightly higher than for signals in Cluster-4. However, the average duration for the signals in the cluster with the low-frequency components (Cluster-4) is much longer than the duration for Cluster-5 and Cluster-6.

In Figure 4.11, the variation of cumulative signal strength in terms of the age of the concrete for each cluster is presented. The cumulative signal strengths were normalized by the maximum value for each specimen. In the confined specimen, the signals with the highest frequency components (Cluster-3) have dominant CSS from the early age. However, the CSS of Cluster-2 is very close to the CSS of Cluster-3 up to the concrete age of 150 days. After 150 days, the CSS rate for Cluster-3 increases, while the CSS rate of Cluster-2 continues with approximately the same rate. The signals in cluster Cluster-1 have negligible signal strength compared to Cluster-2 and Cluster-3 and initiate primarily after 120 days. In the unconfined specimen, the AE energy is primarily attributed to cluster Cluster-4 up to approximately 150 days. After 150 days, the clusters with the higher frequency components (Cluster-5 and Cluster-6) become prominent in terms of AE energy release.



(a)



(b)

Figure 4.11 Normalized cumulative signal strength. (a) Confined specimen; (b) Unconfined specimen.

The distribution of total AE signal strength for the classified clusters and sensors at different ages of the concrete (66, 150, 195 days) are illustrated in Figure 4.12. These distributions are referred to as signal strength contribution factors (SSCF). The 66th day and 195th day were selected to illustrate the trend of data at the beginning and end of the evaluated time window. The 150th day was selected because in both reactive specimens there was an obvious change in the rate of CSS of the clusters with high-frequency components in comparison to the lower frequency components. The figures on the left

show results of the confined specimen and the figures to the right show data from the unconfined specimen.

In the confined specimen, most of the energy contribution is related to Cluster-2 (energy concentration in 50–150 kHz) and Cluster-3 (energy concentration in 150–300 kHz). The SSCF for Cluster-3 is increases with time, particularly after 150 days. Most of the AE energy for Cluster-3 is concentrated in sensor 3 (mid-thickness of the specimen) after 100 days. Cluster-2 and Cluster-3 both have prominent AE energy at sensor 2 before the 66th day. Then the highest AE energy portion moves to sensor 3, whereas SSCF of Cluster-2 is much lower than Cluster-3, especially after 150 days. The SSCF for cluster Cluster-1 is negligible compared to other clusters. In the unconfined specimen, the highest SSCF is for cluster Cluster-4 (energy concentration between 0–150 kHz) at sensor 4 (attached to top reinforcement) at 66 days. However, this energy contribution decreases with time, and the SSCF of the clusters with high-frequency components (Cluster-5 and Cluster-6) increases with time. There is no obvious energy concentration in the sensor located at mid-thickness of the specimen (sensor 6), which is different from what is observed in the confined specimen. In both specimens, the SSCF declines in low-frequency signals and increases in high-frequency signals with time. This trend in signal frequency from low to high in the confined specimen is not pronounced before 150 days. The SSCF for cluster Cluster-3 is slightly greater than the Cluster-2 at 150 days. The signal frequency trend initiates primarily after 150 days in this specimen. On the other hand, in the unconfined specimen, the frequency content evolution of AE signals is obvious from an earlier stage of ASR reaction (66 days) and is more significant after 150 days.

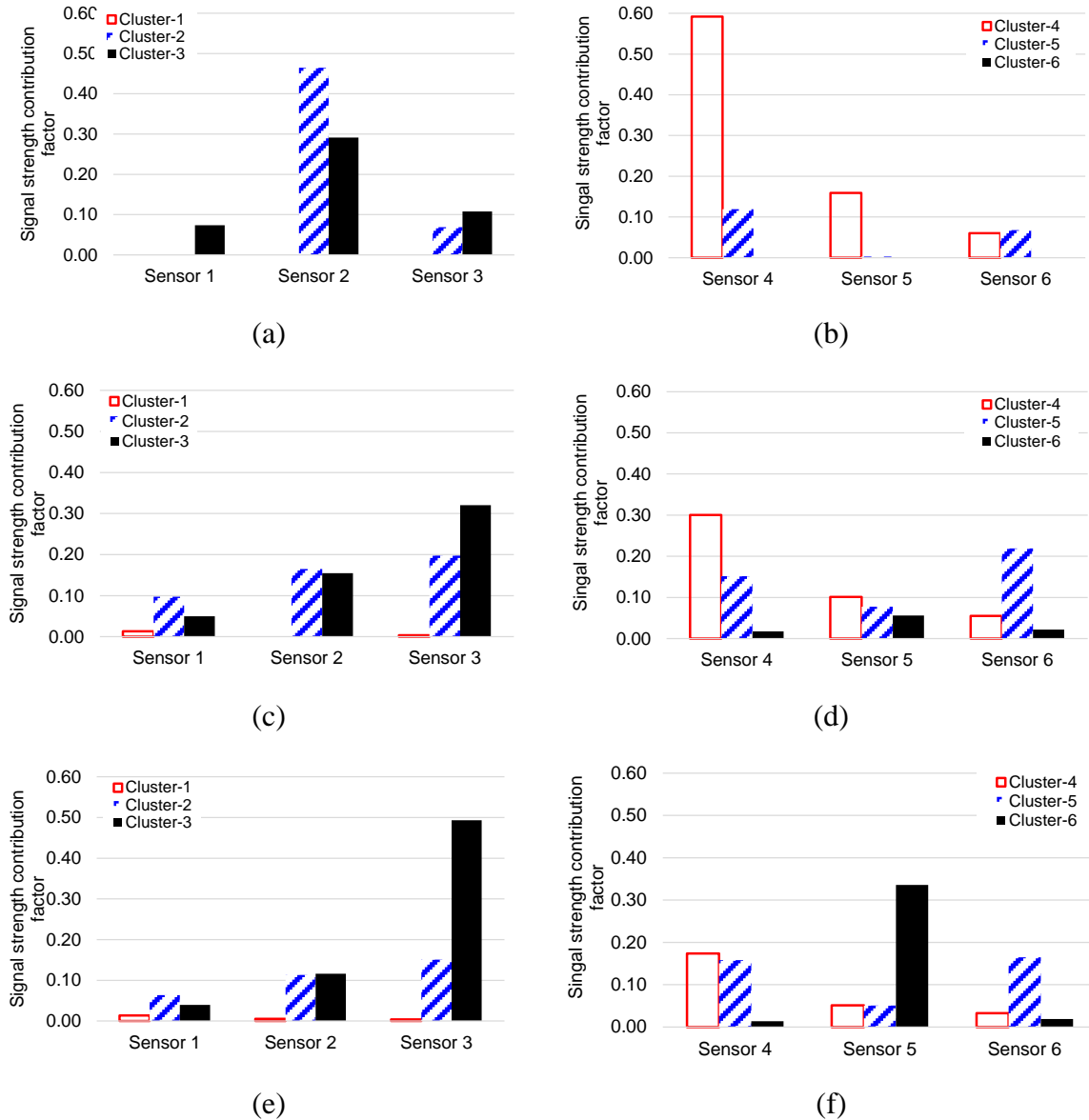


Figure 4.12 Distribution of total AE signal strength in terms of clusters and sensors. (a) Confined specimen at age of 66 days; (b) Unconfined specimen at age of 66 days; (c) Confined specimen at age of 150 days; (d) Unconfined specimen at age of 150 days; (e) Confined specimen at age of 195 days; (f) Unconfined specimen at age of 195 days.

The confined specimen has a higher extensional strain along the Z direction than the unconfined specimen (approximately 42% more at 195 days). This expansion leads to tension concentration through the thickness of the confined specimen. Since there is no confinement through the specimen thickness it is susceptible to crack formation. In the

unconfined specimen, the expansion strain is more evenly distributed between the X-Y plane and the thickness. Therefore, the tension is more uniformly distributed in the entire specimen in comparison to the confined specimen. This is also observable from the AE data, where sensor 3, located at the mid-height of the confined specimen, has a larger SSCF than the unconfined specimen (e.g., 65% for the confined specimen versus 35% for the unconfined specimen at 195 days).

As mentioned previously, the frequency of AE signals progresses from low to high as the concrete ages. This may be attributable to the formation of cracking through the coarse aggregate due to ASR progression. The crack formation inside the aggregate is expected to have higher frequency components than the cement matrix and interfacial transition zone (ITZ) as mentioned by Farnam et al. [17]. The transition from low-frequency signals to the high-frequency signals in the confined specimen initiated later than for the unconfined specimen (after 150 days). However, there are different contradictory hypotheses relating to formation of cracks in concrete due to ASR [33]. For instance, osmotic pressure theory was proposed by Hanson to describe the mechanism of expansion [34]. In this theory, the cement paste surrounding to reactive aggregates acts as a semi-permeable membrane, which water solution can pass inside the region around the reactive aggregates, but alkali-silica ions are enclosed in the reactive regions. This causes osmotic pressure and alkali-silica gel swells and exerts pressure to the cement paste. This pressure leads to crack formation in the cement paste [34]. McGowan and Vivian also proposed a similar theory as osmotic theory, which transforming a solid alkali-silica layer on a reactive aggregate to a gel by absorbing moisture from the pore solution was explained as a main reason of cracking in the cement paste due to ASR [35]. Bazant and

Steffens suggested that the cracking is caused in the cement paste and interfacial transition zone due to accumulation of alkali-silica gel in the interfacial transition zone and resulting gel pressure [36]. On the other hand, Dron and Brivot assumed that crack formation occurred far away from reactive aggregates due to diffusing dissolved silica away from aggregate into the pores in the cement paste [37]. Some researchers observed that ASR gel initially forms inside a reactive aggregate and causes the pressure and crack formation inside the aggregate and surrounding cement paste [12,38-41]. Ponce and Batic [42] related the cracking pattern of concrete due to ASR to the types of reactive aggregate. ASR cracks start to form inside aggregate or in the cement matrix depending on the aggregate type [42].

In the confined specimen, the CSS rate of Cluster-3 (energy concentration 150–300 kHz), started to increase at the age of 150 days. In the unconfined specimen, the CSS rate for the cluster with the higher frequency components also increases around that time. 150 days is close to the inflection point of the volumetric strain curve, after which point expansion rates decrease. In addition, the first visible cracks were observed at the age of 150 days on the sides of the unconfined specimen, but no cracks were visible on the top surface of the unconfined specimen. Cracks could not be traced in the confined specimen on the sides due to the steel confinement frame. From the above observations, 150 days is a significant time period for ASR in the specimens, which generally agrees with trends in the AE data.

4.6 Conclusions

Acoustic emission was utilized for monitoring the activities caused by ASR in large-scale reinforced concrete specimens. The specimens resemble common nuclear

power plant containments with no shear reinforcement. An agglomerative hierarchical algorithm was used to classify the AE data based on the energy-frequency dependent features to study and identify the damage mechanisms in the specimens with different stress boundary conditions. The conclusions of this study are summarized as follows:

- A significant portion of the AE data (in terms of cumulative signal strength) in the confined specimen was recorded by sensor 3, which was located at mid-thickness. However, the portion of cumulative signal strength for the corresponding sensor at mid-thickness of the unconfined specimen was less in comparison to the other two sensors in that specimen. This agrees with expectations, as the confined specimen exhibited increased out-of-plane expansion in comparison to the unconfined specimen, meaning that the crack distribution is expected to be more concentrated near mid-thickness of the confined specimen than near the reinforcement layers.
- The frequency contents of signals in the confined and unconfined specimens evolved from low to high frequency with the age of concrete although this evolution started later in the confined specimen than the unconfined specimen. Since the high-frequency AE signals have been associated to the cracking in aggregates [17], different crack mechanisms in aggregate for the confined and unconfined specimens are expectable. However, there are different contradictory ASR cracking hypotheses that have been proposed by the researchers [33-38,41-43].

- There is a coincident point observed in the strain curves and the CSS of Cluster-3 in the confined specimen and Cluster-6 in the unconfined specimen. The CSS rate in terms of concrete age increases at the time (around 150 days), when the strain rate is decreasing. This point is named as inflection point of strain curve, where the curvature of strain curve changes from positive to negative. The inflection point location in terms of concrete age depends on the kinetic of ASR reaction and diffusion process. Determining the inflection point, latency and characteristic time are experimentally estimated, which are the two important modeling parameters. According to the results of AE data and clustering, the inflection point location in terms of concrete age could be estimated from the variation in CSS rate change of clustered AE data.
- Monitoring of a structural system with acoustic emission can provide useful information regarding condition based maintenance and/or retrofit. For example, one potential time of action for treating affected structures is around the inflection point in the volumetric strain curve which can be approximated through acoustic emission data. This point coincided with observation of first visible surface cracking. After identifying the time of action, treatment methods may be implemented to mitigate the effects of ASR. Injection of lithium solution is a chemical alternative to mitigate ASR provided that enough solution penetration in the structure can be achieved. Another method is to remove moisture through coatings and sealers such as silane sealers and bituminous or elastomeric coatings.

After conducting these methods, structures should be monitored for enough time to evaluate the efficiency of the method or methods.

Acknowledgments: This material is based upon work partly supported by the U.S. Department of Energy, Office of Nuclear Energy, Light Water Reactor Sustainability Program, under contract number DE-AC05-00OR22725. This manuscript has been co-authored by UT-Battelle, LLC under Contract No. DE-AC05-00OR22725 with the U.S. Department of Energy. The United States Government retains and the publisher, by accepting the article for publication, acknowledges that the United States Government retains a non-exclusive, paid-up, irrevocable, worldwide license to publish or reproduce the published form of this manuscript, or allow others to do so, for United States Government purposes. The Department of Energy will provide public access to these results of federally sponsored research in accordance with the DOE Public Access Plan (<https://www.energy.gov/downloads/doe-public-access-plan>).

4.7 References

1. Schmidt, J.W.; Hansen, S.G.; Barbosa, R.A.; Henriksen, A. Novel shear capacity testing of asr damaged full scale concrete bridge. *Engineering Structures* **2014**, *79*, 365-374.
2. Clark, L. *Critical review of the structural implications of the alkali silica reaction in concrete*. Bridges Design, Structures Group, Transportation and Road Research Laboratory: 1989.

3. Bach, F.; Thorsen, T.S.; Nielsen, M. Load-carrying capacity of structural members subjected to alkali-silica reactions. *Construction and Building Materials* **1993**, 7, 109-115.
4. Bakker, J. In *Control of asr related risks in the netherlands*, Proceedings of the 13th International Conference on Alkali-Aggregate Reaction in Concrete, 2008; T rondheim:[sn]: pp 21-31.
5. Charlwood, R.; Solymar, S.; Curtis, D. In *A review of alkali aggregate reactions in hydroelectric plants and dams*, Proceedings of the international conference of alkali-aggregate reactions in hydroelectric plants and dams, 1992.
6. Saouma, V.E.; Hariri-Ardebili, M.A. A proposed aging management program for alkali silica reactions in a nuclear power plant. *Nuclear Engineering and Design* **2014**, 277, 248-264.
7. Takakura, T.; Ishikawa, T.; Mitsuki, S.; Matsumoto, N.; Takiguchi, K.; Masuda, Y.; Nishiguchi, I. In *Investigation on the expansion value of turbine generator foundation affected by alkali-silica reaction*, Proceedings of 18th International Conference on Structural Mechanics in Reactor Technology, 2005.
8. Takakura, T.; Masuda, H.; Murazumi, Y.; Takiguchi, K.; Masuda, Y.; Nishiguchi, I. Structural soundness for turbine-generator foundation affected by alkali-silica reaction and its maintenance plans. **2007**.
9. Tchner, J.; Aziz, T. In *Effects of aar on seismic assessment of nuclear power plants for life extensions*, Proceedings SMiRT, 2009; pp 1-8.

10. Charlwood, R. In *Predicting the long term behaviour and service life of concrete dams*, Long Term Behaviour of Dams, LTBD09, Graz, Austria, 2009; Graz, Austria.
11. Abdelrahman, M.; ElBatanouny, M.K.; Ziehl, P.; Fasl, J.; Larosche, C.J.; Fraczek, J. Classification of alkali–silica reaction damage using acoustic emission: A proof-of-concept study. *Construction and Building Materials* **2015**, *95*, 406-413.
12. Garcia-Diaz, E.; Riche, J.; Bulteel, D.; Vernet, C. Mechanism of damage for the alkali–silica reaction. *Cement and Concrete Research* **2006**, *36*, 395-400.
13. Sargolzahi, M.; Kodjo, S.A.; Rivard, P.; Rhazi, J. Effectiveness of nondestructive testing for the evaluation of alkali–silica reaction in concrete. *Construction and Building Materials* **2010**, *24*, 1398-1403.
14. Anay, R.; Soltangharaei, V.; Assi, L.; DeVol, T.; Ziehl, P. Identification of damage mechanisms in cement paste based on acoustic emission. *Construction and Building Materials* **2018**, *164*, 286-296.
15. Soltangharaei, V.; Anay, R.; Assi, L.; Ziehl, P.; Matta, F. In *Damage identification in cement paste amended with carbon nanotubes*, AIP Conference Proceedings, 2018; AIP Publishing: p 030006.
16. Lokajiček, T.; Příkryl, R.; Šachlová, Š.; Kuchařová, A. Acoustic emission monitoring of crack formation during alkali silica reactivity accelerated mortar bar test. *Engineering Geology* **2017**, *220*, 175-182.
17. Farnam, Y.; Geiker, M.R.; Bentz, D.; Weiss, J. Acoustic emission waveform characterization of crack origin and mode in fractured and asr damaged concrete. *Cement and Concrete Composites* **2015**, *60*, 135-145.

18. Rajabipour, F.; Giannini, E.; Dunant, C.; Ideker, J.H.; Thomas, M.D. Alkali-silica reaction: Current understanding of the reaction mechanisms and the knowledge gaps. *Cement and Concrete Research* **2015**, *76*, 130-146.
19. Weise, F. Innovative measurement techniques for characterising internal damage processes in concrete due to asr. **2012**.
20. Morenon, P.; Multon, S.; Sellier, A.; Grimal, E.; Hamon, F.; Bourdarot, E. Impact of stresses and restraints on asr expansion. *Construction and Building Materials* **2017**, *140*, 58-74.
21. Saouma, V.E.; Hariri-Ardebili, M.A.; Le Pape, Y.; Balaji, R. Effect of alkali-silica reaction on the shear strength of reinforced concrete structural members. A numerical and statistical study. *Nuclear Engineering and Design* **2016**, *310*, 295-310.
22. Hayes, N.W.; Gui, Q.; Abd-Elssamd, A.; Le Pape, Y.; Giorla, A.B.; Le Pape, S.; Giannini, E.R.; Ma, Z.J. Monitoring alkali-silica reaction significance in nuclear concrete structural members. *Journal of Advanced Concrete Technology* **2018**, *16*, 179-190.
23. Hsu, N. Characterization and calibration of acoustic emission sensors. *Mater. Eval.* **1981**, *39*, 60-68.
24. Express-8 ae system user's manual, mistras group, inc. **2014**.
25. Murtagh, F.; Legendre, P. Ward's hierarchical agglomerative clustering method: Which algorithms implement ward's criterion? *Journal of classification* **2014**, *31*, 274-295.

26. Tan, P.N.; Steinbach, M.; Kumar, V. Data mining cluster analysis: Basic concepts and algorithms. *Introduction to data mining* **2013**.
27. Saouma, V.; Perotti, L.J.A.m.j. Constitutive model for alkali-aggregate reactions. **2006**, *103*, 194.
28. Ulm, F.-J.; Coussy, O.; Kefei, L.; Larive, C.J.J.o.e.m. Thermo-chemo-mechanics of asr expansion in concrete structures. **2000**, *126*, 233-242.
29. Fowler, T.J.; Blessing, J.A.; Conlisk, P.J.; Swanson, T.L. The monpac system. *Journal of acoustic emission* **1989**, *8*, 1-8.
30. ElBatanouny, M.K.; Ziehl, P.H.; Larosche, A.; Mangual, J.; Matta, F.; Nanni, A. Acoustic emission monitoring for assessment of prestressed concrete beams. *Construction and Building Materials* **2014**, *58*, 46-53.
31. Aggelis, D.; Soulioti, D.; Gatselou, E.; Barkoula, N.-M.; Matikas, T.J.C.a.B.M. Monitoring of the mechanical behavior of concrete with chemically treated steel fibers by acoustic emission. **2013**, *48*, 1255-1260.
32. Xargay, H.; Folino, P.; Nuñez, N.; Gómez, M.; Caggiano, A.; Martinelli, E.J.C.a.B.M. Acoustic emission behavior of thermally damaged self-compacting high strength fiber reinforced concrete. **2018**, *187*, 519-530.
33. Pan, J.; Feng, Y.; Wang, J.; Sun, Q.; Zhang, C.; Owen, D.J.F.o.S.a.C.E. Modeling of alkali-silica reaction in concrete: A review. **2012**, *6*, 1-18.
34. Hanson, W. In *Studies relating to the mechanism by which the alkali-aggregate reaction produces expansion in concrete*, Journal Proceedings, 1944; pp 213-228.

35. McGowan, J.J.A.J.A.S. Studies in cement-aggregate reaction xx, the correlation between crack development and expansion of mortar. **1952**, 3, 228-232.
36. Bažant, Z.P.; Steffens, A.J.C.a.C.R. Mathematical model for kinetics of alkali-silica reaction in concrete. **2000**, 30, 419-428.
37. Dron, R.; Brivot, F.J.C.a.C.R. Thermodynamic and kinetic approach to the alkali-silica reaction. Part 1: Concepts. **1992**, 22, 941-948.
38. Idorn, G.J.C.a.C.R. A discussion of the paper "mathematical model for kinetics of alkali-silica reaction in concrete" by zdenek p. Bazant and alexander steffens. **2001**, 7, 1109-1110.
39. Jun, S.S.; Jin, C.S.J.K.J.o.C.E. Asr products on the content of reactive aggregate. **2010**, 14, 539-545.
40. Goltermann, P.J.M.J. Mechanical predictions of concrete deterioration; part 2: Classification of crack patterns. **1995**, 92, 58-63.
41. Ichikawa, T.; Miura, M.J.C.a.C.r. Modified model of alkali-silica reaction. **2007**, 37, 1291-1297.
42. Ponce, J.; Batic, O.R.J.C.a.C.R. Different manifestations of the alkali-silica reaction in concrete according to the reaction kinetics of the reactive aggregate. **2006**, 36, 1148-1156.
43. Escalante-García, J.; Sharp, J. The microstructure and mechanical properties of blended cements hydrated at various temperatures. *Cement and Concrete Research* **2001**, 31, 695-702.

Chapter 5

Temporal Evaluation of ASR Cracking in Concrete Specimens Using Acoustic Emission¹

¹ Vafa Soltangharai, Rafal Anay, Li Ai, Eric R. Giannini, Jinying Zhu, and, Paul Ziehl, Temporal evaluation of ASR cracking in concrete specimens using acoustic emission. Accepted by *ASCE-Journal of Materials in Civil Engineering*. Reprinted here with permission from ASCE, This material may be downloaded for personal use only. Any other use requires prior permission of the American Society of Civil Engineers. This material may be found at [DOI: 10.1061/(ASCE)MT.1943-5533.0003353]. 3/5/2020

5.1 Abstract

The effect of boundary conditions on the distribution of alkali-silica reaction (ASR) damage in concrete blocks is studied by leveraging acoustic emission sensing with a data-driven approach. The innovation lies in deriving damage contours caused by ASR based on a minimal sensor array. Through this approach, damage progression can be traced in time and event distribution can be visualized. A gap in the current literature, namely evaluating ASR progress in concrete structures with different boundary conditions using AE, is addressed. Unsupervised pattern recognition is utilized to study the effect of the temporal damage condition. In the confined specimen, the distribution of AE events in the mid-width region of the specimen is concentrated and has a sharp peak. The surface cracks are mostly oriented along the specimen length and in the mid-width region. However, in the unconfined specimen, the distribution of AE events is more uniform, and cracks are randomly distributed.

Keywords: Acoustic emission; alkali-silica reaction; damage imaging; unsupervised pattern recognition

5.2 Introduction

Alkali-silica reaction (ASR) is one source of damage in concrete structures. The reaction occurs between the alkali hydroxides (NaOH, KOH) in the pore solution, mainly from the cement, and certain siliceous minerals present in some concrete aggregates [1,2]. The result of the reaction is a hygroscopic alkali-silica gel which tends to absorb water and expand. The reaction and subsequent swelling are accelerated by high temperatures and humidity over ~80%. The gel expands and exerts pressure on the cement matrix and aggregates [3]. This pressure causes microcracks and macrocracks in

the concrete components. Different structures have been affected by ASR such as concrete dams [4-6], bridges [1,7,8], and nuclear structures (nuclear power plants and nuclear waste containments) [9-14].

Several methods have been used for monitoring ASR progress in structures. Some common methods include visual inspection, coring [1,15], petrographic analysis [1,16], demountable mechanical strain gauges (DEMEC gauge) [17-19], relative humidity or moisture content measurement, and crack indexing [19,20]. Despite the simplicity of these methods, they have some drawbacks. For instance, visual inspection is not efficient for the early detection of ASR damage since ASR damage initiates internally in the concrete and then extends to the surface. This is more critical in thick shear walls (e.g., nuclear structures), where most of the expansion happens out-of-plane due to in-plane confinement and the damage on the surface appears in the latter stages of the ASR reaction. Furthermore, visual inspection is time-consuming and often operator-dependent, especially for large-scale structures, although advances in drone inspection and image analysis could improve visual inspection [21-23]. Crack indexing is also time-consuming and not easily applied for evaluating very large and complex structures. Although DEMEC gauges are generally useful for some structural components such as piles and columns, it is not a well-suited index for studying damage in shear walls, because it measures expansion on the surface rather than through the thickness. Petrography is helpful for ASR damage quantification using a damage rating index, but it is time-consuming and intrusive. In addition, the method is focused on microscale damage in the concrete and diagnosing the cause(s) of distress, but it is difficult to generalize petrographic results for the structural capacity. Coring is also a destructive method, and

large numbers of cores are impractical for potentially sensitive structures such as nuclear containments.

Nondestructive methods [24,25] are an alternative for damage quantification and condition assessment of structures affected by ASR. Several methods have been employed for this purpose such as digital image correlation [26], nonlinear Rayleigh surface ultrasonic [27,28], ultrasonic pulse velocity [29], dynamic modulus of elasticity [30], impact-echo [24], and acoustic emission (AE) [16,28,31,32]. Acoustic emission is a passive structural health monitoring approach which has recently been utilized for detection of damage in concrete elements [9,16,28,31,32]. This method uses piezoelectric sensors to respond to elastic stress waves emitted by crack formation and records them as digital signals, usually amplified through external or integral preamplifiers. The sensors are very sensitive and can capture internal microscale damage development. Furthermore, AE can monitor structural condition continuously without disrupting use of the structure, damage localization is feasible [33-35]; and the method is applicable when only one side of the structure is accessible.

To date, AE has mainly been explored for small-scale concrete specimens affected by ASR without steel reinforcement. For example, Abdelrahman et al. [16] utilized AE for monitoring ASR in ASTM standard concrete prisms. The authors found a correlation between AE activity and expansion from ASR measured per ASTM C1293. Furthermore, parameters of intensity analysis were correlated with the petrographic damage rating index (DRI). Farnam et al. [31] used mortar cylinders with a diameter and height of 20 mm and 40 mm. AE signals were characterized according to peak frequency and frequency centroid, and high-frequency signals were related to microcracking in

aggregates. Lokajiček et al. [28] utilized AE to monitor ASR in mortar prisms with different aggregate reactivities and reported a correlation between cumulative AE energy and damage.

In these prior works, small-scale specimens were investigated without specific boundary conditions or confinement. However, in reality, structures have different boundary conditions, and it has been shown that boundary conditions have a significant effect on damage distribution due to ASR [1,17,36-40]. Moreover, the authors are not aware of investigations reported in the open literature to visualize the temporal development of ASR damage in concrete structures using AE. Therefore, the effect of boundary conditions on damage distribution and progression in terms of AE data is addressed in this paper. The temporal development of ASR damage concentration is visualized by developing contours based on AE data. Furthermore, damage distributions and progression are inferred by observing event distributions. Three medium-scale specimens having different confinement conditions were cast and prepared for accelerated aging. AE was continuously monitored and expansion strains and crack width intermittently measured. Correlations between expansion and crack width data to the AE data are discussed.

5.3 Test setup and procedure

Three concrete block specimens with dimensions 305 mm × 305 mm × 1120 mm were cast at The University of Alabama and delivered to the University of South Carolina for testing. The sensor layouts, geometries, and structural details are presented in Figure 5.1. Two specimens were cast with reactive coarse aggregates and the third had non-reactive aggregate to serve as a control specimen. One of the reactive specimens had

reinforcing steel along two dimensions (X and Z). This specimen is referred to as the confined specimen in this paper. The other reactive specimen did not have any reinforcement. This specimen is referred to as the unconfined specimen in this paper. The reinforcement details for the confined specimen is presented in Figure 5.1b. The confined specimen had four longitudinal US #7 steel rebars and US #6 steel rebars at 150 mm on center as transverse reinforcement (Figure 5.1b). All rebars were T-headed to compensate for the short development length. The specimen without reactive aggregate is referred to as the control specimen. It did not have any steel reinforcement like the unconfined specimen as shown in Figure 5.1d.

Ten acoustic emission sensors were affixed to the surface of each reactive specimen (one confined and one unconfined specimen) as illustrated in Figure 5.1a. Two sensors were located at the top and bottom surfaces, and three sensors were attached to the front and back surfaces. Four sensors were mounted on the control specimen (two on the front and two on the back surface) as shown in Figure 5.1c. All sensors were wideband type PKWDI with 26-dB preamplification. Sensor coordinates are presented in Table 5.1. The sensors were attached on the surface of the specimens using epoxy, and constant pressure was applied to the surface of the sensors through specially designed and fabricated holders [9]. The sensor-to-cable connections were protected with heat shrink tubing.

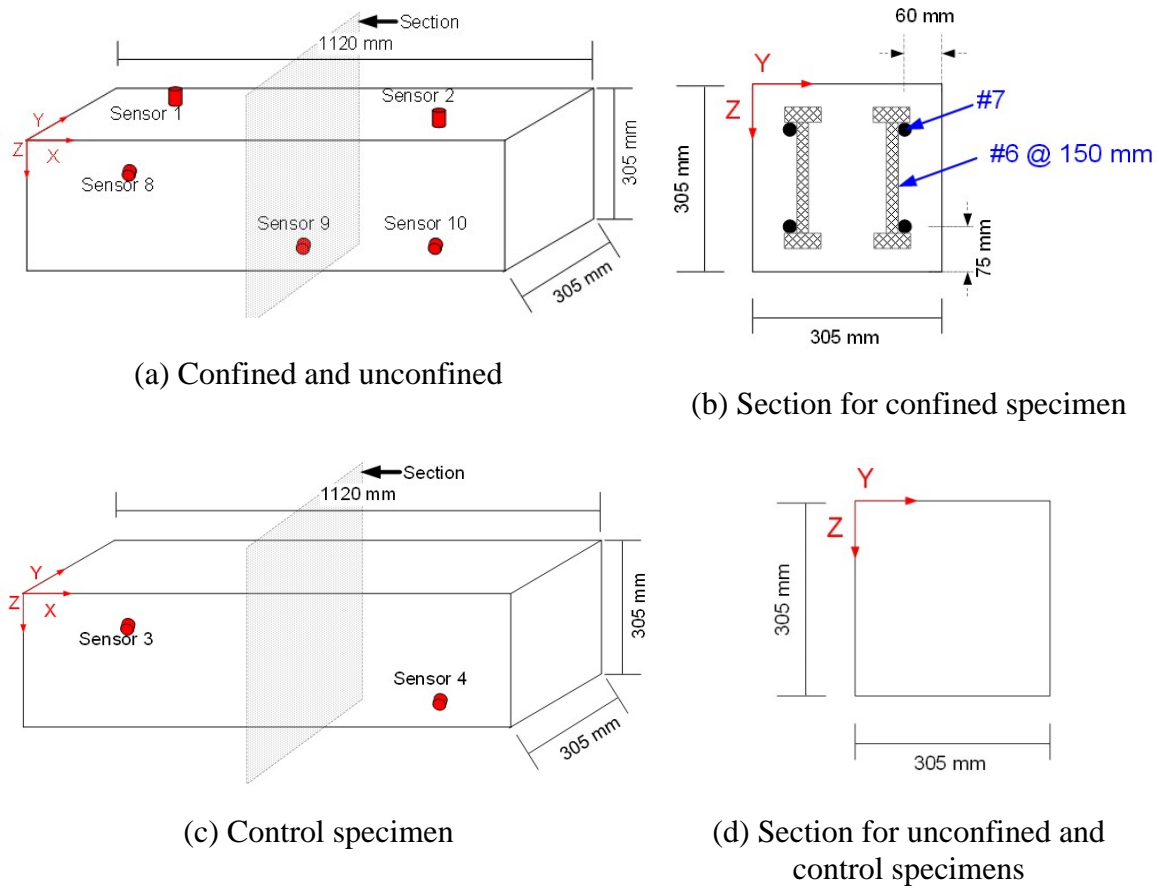


Figure 5.1 Specimen sensor layouts and structural details.

Table 5.1 Sensor coordinates.

Sensor No.	Confined and unconfined specimens			Control specimen		
	X (mm)	Y (mm)	Z (mm)	X (mm)	Y (mm)	Z (mm)
Sensor 1	279	229	0	279	305	229
Sensor 2	838	76	0	838	305	76
Sensor 3	279	76	305	279	0	76
Sensor 4	838	229	305	838	0	229
Sensor 5	279	305	229	-	-	-
Sensor 6	483	305	76	-	-	-
Sensor 7	838	305	76	-	-	-
Sensor 8	279	0	76	-	-	-
Sensor 9	635	0	229	-	-	-
Sensor 10	838	0	229	-	-	-

A 24-channel Micro-II Express, manufactured by MISTRAS Group, Inc. (Princeton Junction, NJ, USA), was utilized for data acquisition with a sampling rate of 5 million samples per second. Equipment setting are provided in Table 5.2.

Table 5.2 Data acquisition setting.

Sampling rate	Threshold	Pretrigger time	Hit definition time
5000 kHz	32 dB	256 μ s	400 μ s
Peak definition time	Hit lockout time	Low-pass digital filter	High-pass digital filter
200 μ s	200 μ s	400 kHz	20 kHz

Concrete mixture proportions are presented in Table 5.3. In the reactive specimens, only the coarse aggregate was reactive. The reactive coarse aggregate was crushed greenschist from North Carolina. The nonreactive coarse aggregate (used in the control specimen) was crushed dolomite from Alabama. The nonreactive fine aggregate used in all specimens was dolomitic limestone sand from Alabama. The cement used in the mixture was an ASTM C150 Type I/II low-alkali cement with 0.48% $\text{Na}_2\text{O}_{\text{eq}}$. Sodium

hydroxide (NaOH) was added to the two reactive specimens to increase the total alkali loading to 1.50% by mass of cement to accelerate the development of ASR.

Table 5.3 Concrete mixture proportions.

Mixture components	Quantity (kg/m ³)	
	Control specimen	Reactive specimens
Cement	350	350
w/c ratio	0.5	0.5
Nonreactive coarse aggregate	1140	-
Reactive coarse aggregate	-	1050
Nonreactive sand	752	851
NaOH solution (50% w/w)	-	9.22

The specimens were supported on specially designed and fabricated steel carriers with wheels. The contact surfaces of the carriers were covered by neoprene pads to minimize the transference of potential vibrations and noise from the ground.

The specimens were retained inside a chamber with dimensions of 243 cm (width) × 243 cm (length) × 122 cm (height). The temperature and humidity of the chambers were kept at 37 ± 3 °C and $95\% \pm 5\%$ during the test with the exception of scheduled shutdown dates (for expansion measurement and maintenance).

The expansions in the specimens were measured monthly using DEMEC gauges (demountable mechanical strain gauges) with gauge lengths of 500 mm for X-direction (length) measurements and 150 mm for Y- and Z-direction (height and width) measurements, respectively. DEMEC gauge measurements were started at 48 days after casting the specimens. Measurement of the crack width was begun at 146 days after casting using a Dino-Lite digital microscope with a maximum magnification of 184 X and ELE crack detection microscope with a magnification of 40 X.

5.4 Analysis procedure

The AE data were continuously collected for 300 days, with the exception of maintenance and expansion measurement time periods. Filters were developed to minimize non-genuine AE data. After filtering, an unsupervised pattern recognition algorithm was employed to aid in classification of the remaining data. The data were localized using an iterative algorithm and modified times of arrival (TOA) of the classified events. Contour graphs were developed to show the potential damage locations.

The filtering method for the AE data was based on the definition of AE events. AE data that were registered by at least four sensors were retained for further filtering by visual inspection of the waveforms. AE data registered by three or fewer sensors was discarded.

5.4.1 Unsupervised pattern recognition algorithm

The AE signals were transferred to the frequency domain by using fast Fourier transform (FFT). The frequency domain of each signal was divided by ten equal portions with bandwidths of 40 kHz. The energies corresponding to the frequency bands were calculated. The energies in the frequency bands were normalized to the total energy of the signal. These normalized energies for different frequency bands are referred to as frequency-energy-based features in this paper [9]. Principal component analysis (PCA) was conducted on the derived frequency-energy-based features to reduce feature redundancy. Eigenvalues were calculated for the covariance matrix of frequency-energy-based features. Then, the first four principal components were selected as an input of the classification algorithm because their cumulative eigenvalue percentages exceeded 93% and an agglomerative hierarchical algorithm [41] was employed to cluster the data. The

Euclidian distances between the input signals with the PC (principal component) features were calculated. Then the paired data, based on shorter distance, were linked to form a new group. The groups were also linked through a similar procedure referred to as Ward's method as described by Murtagh and Legendre [42]. The resulting link is presented as a dendrogram, with height differences between the branches indicating the distance between the linked data. The final cluster number was determined based on the heights of the branches in the dendrogram. More information about the algorithm may be found in [43].

5.4.2 Source localization and modification of time of arrival

One method for source localization of AE data is the time of arrival (TOA) approach [44]. This method is based on the TOAs of signals registered in each sensor and solving a nonlinear equation of velocity versus distance. Estimating a realistic TOA for signals has a direct effect on the source location precision. Most commercial AE data visualization software has two options for estimating TOAs (peak timing and first time crossing), which are based on peak time and threshold [45]. These methods often do not result in realistic TOAs, especially when the source is far away from the sensors due to wave dispersion and attenuation. The errors related to TOAs increase in heterogeneous materials such as concrete in comparison to homogeneous materials. Therefore, in this study, the Akaike Information Criterion (AIC) was utilized for estimating the TOAs. This method has shown relatively good results in previous research investigations for concrete [46-49]. In this method, a window is defined at the beginning of signal to include the region of the expected signal initiation. In this study, the first 356 μ s of each signal is

considered for TOA calculation. For the windowed signals, the AICs are calculated according to the following equation [46,50]:

$$AIC(t_w) = t_w \log(\sigma^2(S(1:t_w))) + (n_w - k_w) \log(\sigma^2((1+t_w):n_w)) \quad (5.1)$$

Where n_w is the last point of the windowed signal (in this paper, equal to the sample point corresponding to 356 μ s); S is the signal voltage value for all samples; t_w is the desired sample point for calculating the AIC, which ranges from 1 to n_w ; and σ^2 is the variance of signal voltages in the desired range. The AICs are calculated for all sample points in the windowed signals, and the minimum values denote TOAs of the signals.

Another factor which can affect the source location results is the selection of appropriate signals (hits) in an event. Each event may have more than four hits (the minimum hit number for 3D source location), some of which are very weak, and it is hard to find the TOA even by using AIC. Therefore, a method [46] based on the second derivative of AIC was employed for hit selection in an event. The certainty levels (CL) of calculated TOAs are calculated by the following equation [46]:

$$CL = [AIC(t_{min} - \delta t) + AIC(t_{min} + \delta t) - 2AIC(t_{min})]/\delta t^2 \quad (5.2)$$

Where t_{min} is the time in a signal corresponding to the minimum AIC and δt is a small-time interval around the estimated TOA (minimum AIC). This parameter is set to 15 μ s for the data in this study. The lower values for CL indicate unreliable estimated TOA by AIC and can be deleted if a sufficient number of hits exists.

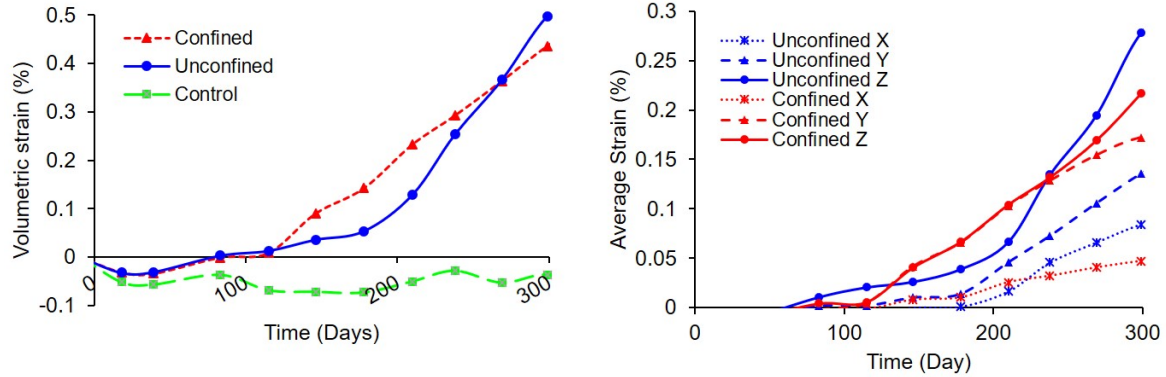
After TOA estimation and selection of the appropriate signals, an iterative source localization algorithm was used to determine the source location. The minimum difference between calculated and observed TOAs is considered as a source location

solution. This procedure was conducted by using a nonlinear least-squares method algorithm [51-54].

The results of source locations are presented in contour diagrams by considering the cumulative signal strength of the events. The specimens were initially meshed, with the enclosed area in each mesh referred to as a “cell”. Then, a customized code was developed to read the input file which was the result of the source location and weight values were assigned to the nodes in each cell according to the number of repeated events in each cell and the average signal strength of each event. The weight values for each cell were updated when a new event occurred inside the cell, with the average signal strength of the new event added to the previous cumulative signal strength in the cell. The weights in all cells were normalized to the maximum weight at the end of the test. The result is a contour diagram corresponding to the concentration of damage.

5.5 Results and discussion

Results of volumetric strain and average strains in the X, Y, and Z directions are presented in Figure 5.2. The reactive specimens expanded; the control specimen did not. The volumetric strain for the confined specimen increased with a higher rate than the unconfined specimen at around 115 days, whereas the volumetric strain for the unconfined specimen reached the value for the confined specimen at 269 days. Based on measured volumetric strain, comparatively more severe damage is expected for the confined specimen than the unconfined specimen between 115 and 220 days.



(a) Volumetric Strain

(b) Average strain

Figure 5.2 Measured strains using DEMEC gauge.

Unconfined specimen: The average strain in the Z direction (specimen depth) exceeds that in the other two directions (Figure 5.2b), potentially due to the lower tensile strength of the concrete along the direction perpendicular to casting [55]. The decreased tensile strength may be associated with a thicker film of bleed water accumulating under aggregates, causing increased porosity and weaker interfacial transition zones around the aggregates. In addition, flat and elongated aggregate particles tend to be preferentially oriented along the plane parallel to the casting direction in concrete, and aggregates having larger specific surface area tend to produce more gel due to ASR [55]. A petrographic study of the unconfined and confined reactive specimens is underway that may provide insight into aggregate particle orientation, directional expansion differences, and the results of those studies will be reported in a future manuscript.

Confined specimen: The strains in the Y and Z directions (width and depth) are almost the same until 238 days. The strains in the Y and Z directions are larger than those in the longitudinal (X) direction. The large strain in the Z direction, despite the confinement, may also be associated with the casting direction effect. It should be noted

that the measurement points for Z-direction expansion were located between the vertical reinforcing bars where confinement may have been locally minimized and this may have contributed to the observed effect. In addition, the confinement along the Z direction caused a redistribution of the ASR induced stress in the Y direction.

The confined/unconfined strain ratio in the Y direction approaches 2.25. Therefore, more cracks oriented parallel to the X direction are expected in the confined specimen, particularly.

Both the number of hits and the cumulative signal strength (CSS) for the control specimen are much less than for the two reactive specimens. Larger amounts of AE activity are observed in the confined versus the unconfined specimen (Figure 5.3).

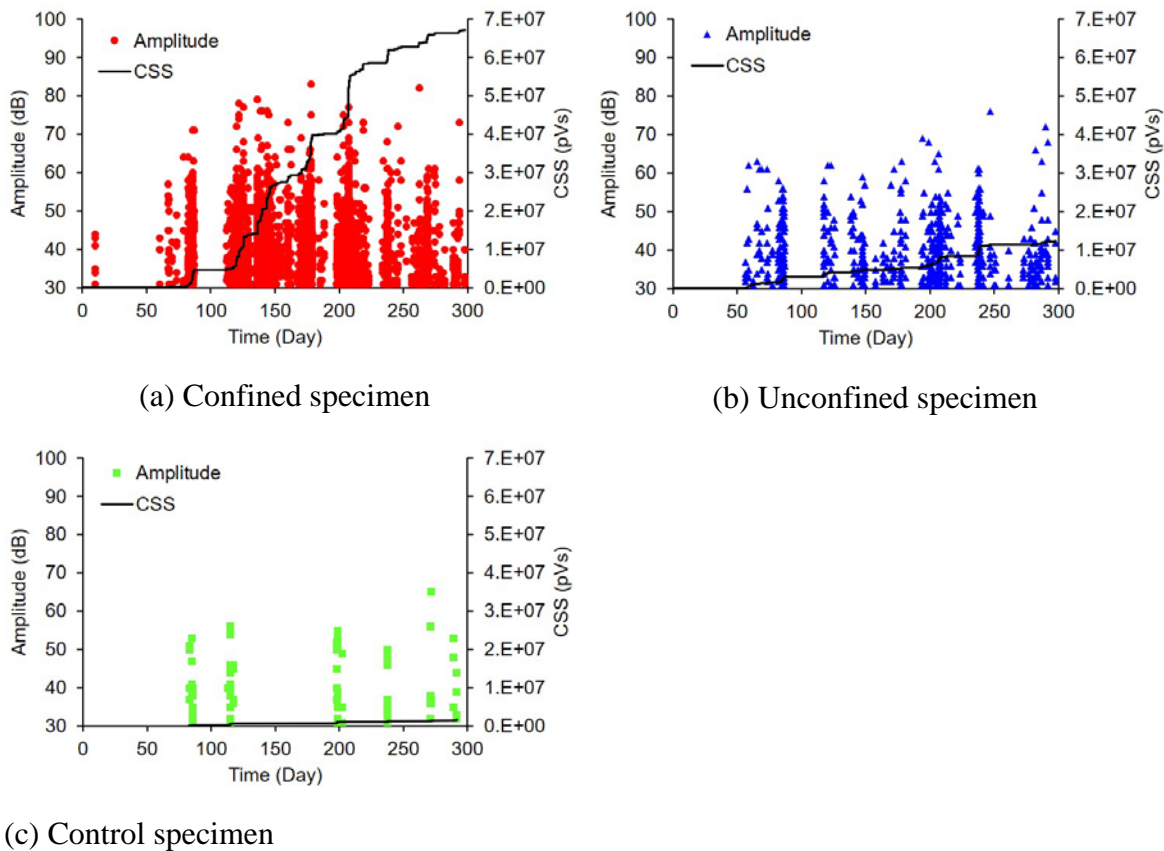


Figure 5.3 Filtered AE data in terms of amplitude and cumulative signal strength versus time.

5.5.1 Frequency-based observations

The data for the confined and unconfined specimens were classified into four clusters and three clusters, respectively. C1 to C4 are for the confined specimen, and U1 through U3 are for the unconfined specimen (Figure 5.4). The number of clusters was determined based on the height of links in the dendrograms, with desired levels for clustering indicated by red lines. The horizontal axis in Figure 5.4 shows data labels, and data are shown in the principal component space in Figure 5.5. Several signals are observed at cluster boundaries which share similar frequency-energy-based features (Figure 5.5 and Figure 5.6).

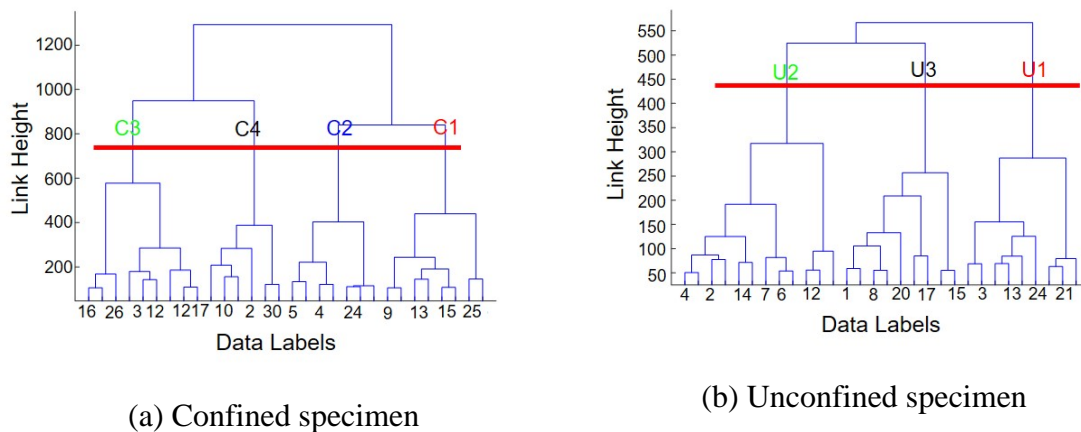
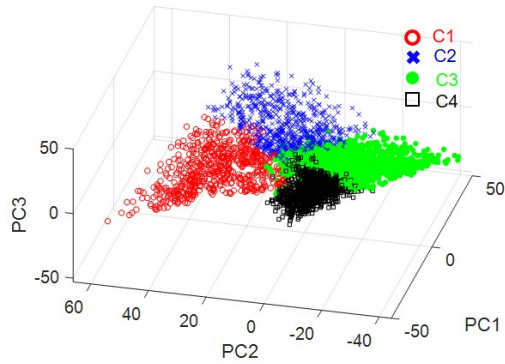
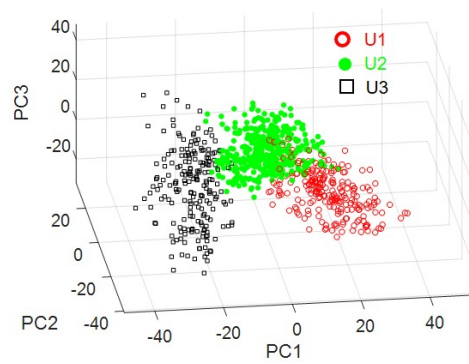


Figure 5.4 Linking dendrograms

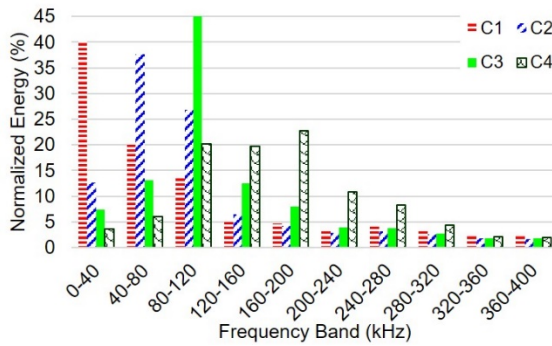


(a) Confined specimen

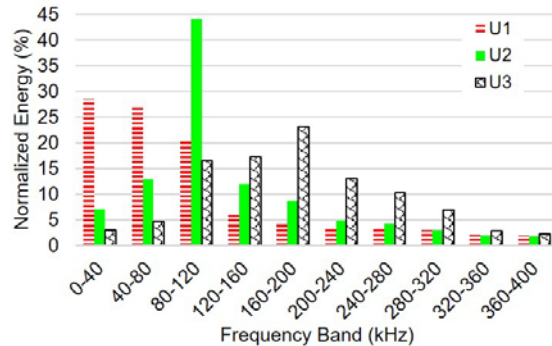


(b) Unconfined specimen

Figure 5.5 Data presentation in principle component space.



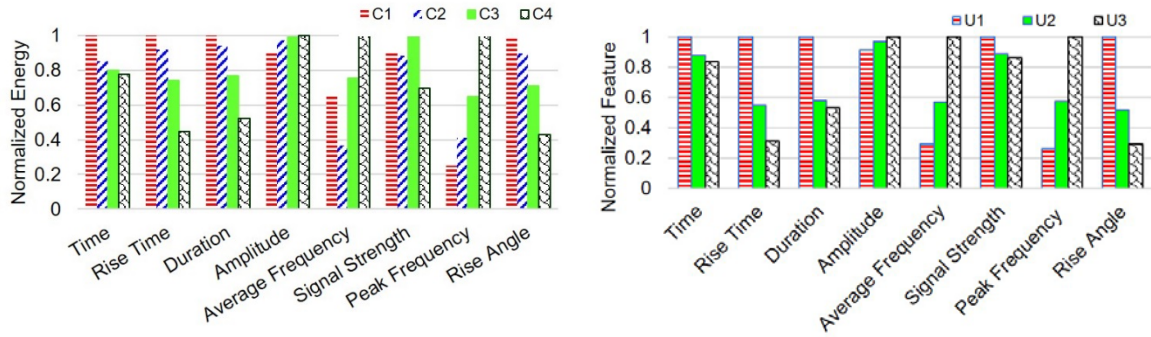
(a) Confined specimen



(b) Unconfined specimen

Figure 5.6 Energy-frequency distributions of clusters.

Unconfined specimen: U1 has 77% energy in the frequency range of 0-120 kHz and is referred to as ‘low’ frequency. U2 has the largest energy concentration (44%) in the range 80-120 kHz and is referred to as ‘medium’ frequency. U3 has 57% energy in the frequency range of 80-200 kHz and is referred to as ‘high’ frequency.



(a) Confined specimen

(b) Unconfined specimen

Figure 5.7 Normalized parametric features.

To better understand the temporal aspects of the AE data, parametric features were averaged and normalized to the maximum values (Figure 5.7). The time parameter refers to the average time of

all signals attributed to a cluster, calculated from when the specimens were moved to the environmental chamber and exposed to high temperature and humidity. The high-frequency clusters (C4 and U3) occurred earlier than the others, and lower frequency clusters appeared later.

The rise angles for both reactive specimens have an inverse relationship with their peak frequencies as also observed in previous studies [9,43,56,57].

The CSS curves in terms of time for the clusters are shown in Figure 5.8. The CSS values were normalized to maximum final values

Confined specimen: The CSS for the ‘medium’ frequency (C3) increases abruptly at 115 days, coinciding with the sudden increase in strain rates in the Y and Z directions. The activity rate starts to decrease after 200 days when the expansion rate in the Y direction decreases.

Unconfined specimen: Strain rates in both Y and Z directions increase modestly up to 178 days, as reflected in the AE data. Strain rate started to increase between 178 to 270 days, especially in the Z direction, causing an increased rate in AE data. The CSS increases significantly, especially in U2, and later in U1 between 180 to 250 days.

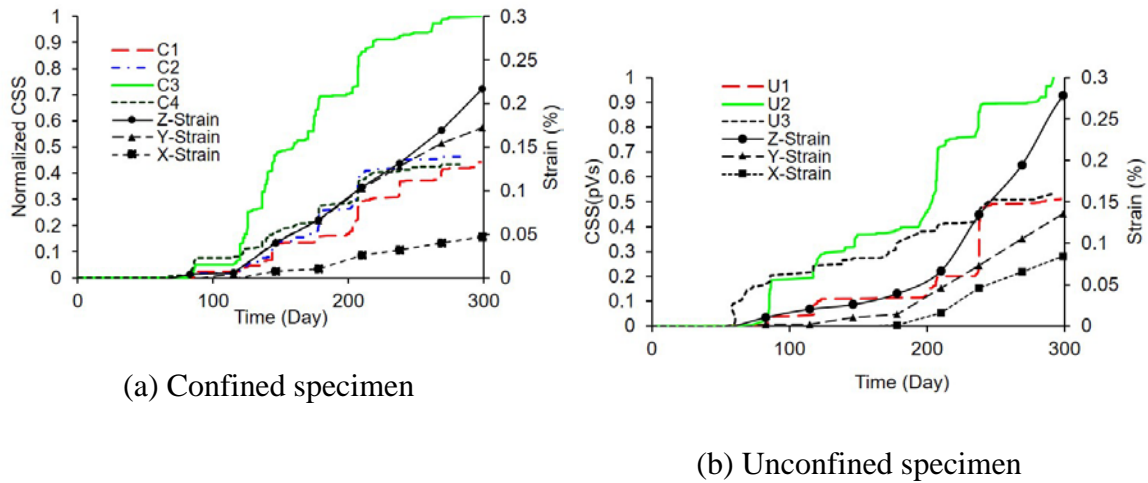


Figure 5.8 Cumulative signal strength for clustered data.

These observations indicate correlations between anisotropic expansion caused by ASR and CSS rates for clusters with differing frequencies. To investigate this further, the number of signals in each cluster within the specific time intervals was calculated and normalized to the total number of AE signals in those intervals (Figure 5.9). In Figure 5.9, the number of signals in C1 and C2 is compared with the number of signals in C3 and C4. In Figure 5.9b, the number of signals in U1 is compared with the number of signals in U2 and U3.

In both confined and unconfined specimens, the percentage of low-frequency signals increased after 200 days. However, this increasing trend started earlier for the confined specimen than for the unconfined specimen. As the ASR process continued,

more macrocracks were expected to form, and the existing cracks were expected to extend and merge. AE signals with low-frequency have been attributed to large-scale cracks and crack extension, whereas AE signals with high-frequency are attributed to the initiation of small-scale cracks [58,59], which is generally consistent with the observed behavior.

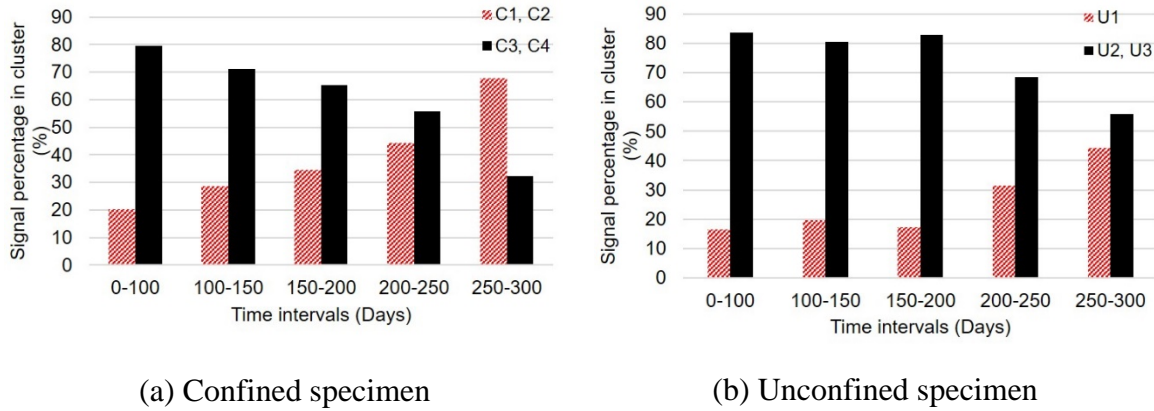


Figure 5.9 Percentage of signals in clusters in terms of time.

One possible explanation of the trends shown in Figure 5.9 is that in the later stage of the ASR process, macrocrack formations and crack extension exceeded microcrack formation. Petrographic and image analyses are in progress to further investigate this. Another possible explanation is wave scattering. In the later stages (after 200 days), the cracks become longer and wider thereby increasing wave scattering, especially for higher-frequency components. A third explanation may be provided [31]. In this study, Farnam et al. suggested that cracks due to ASR initiated inside the aggregates with the emission of high-frequency signals. As the ASR process continued, the cracks propagated inside the cement matrix with the emission of low-frequency signals [31]. However, this explanation depends on the aggregate type [60,61]. In some aggregate types, cracks were observed inside aggregates in addition to the cement matrix.

In other aggregates, cracks were mainly observed in the interfacial transition zones and the cement paste [60,61]. In the specimens for the current investigation, cracks have been observed inside aggregates as well as in the cement matrix. Based on the AE data and visual observation, cracks are expected to generally initiate inside the aggregates and extend to the cement matrix.

The higher percentage of low-frequency signals in later stages of the ASR process may be explained by one of these hypotheses or a combination and is potentially the subject of future investigations.

5.5.2 Source location and event distribution

Source localization was conducted for all events according to the procedure described in section 5.4.2, and contour diagrams were generated based on the source coordinates, source repetition in a cell, and cumulative signal strength in a cell. The diagrams for the unconfined and confined specimens in the X-Y plane are presented for 100, 200, and 300 days in Figure 5.10. The contours show the cumulative signal strength in each cell up to the desired times. The cumulative signal strength for each cell was normalized to the maximum CSS of cells at 300 days, and dimensions are shown in centimeters. The visual surface cracks apparent at 300 days are drawn on the contours to enable comparison. The continuous and dashed lines illustrate the surface cracks at the top and bottom of the specimens, respectively. The crack patterns in the confined and unconfined specimens are different. Most of the cracks in the confined specimens are parallel to the X direction, while the cracks in the unconfined specimen do not follow any specific pattern and are more randomly distributed in the X-Y plane along with both X and Y directions. The damage (cracking) in the confined specimen is more anisotropic

than the unconfined specimen due to partial confinement applied by reinforcement in X and Z directions. The confinement prevents free expansion in the X and Z directions and causes redistribution of ASR stress in the Y direction, consequently causing anisotropic cracking in that specimen.

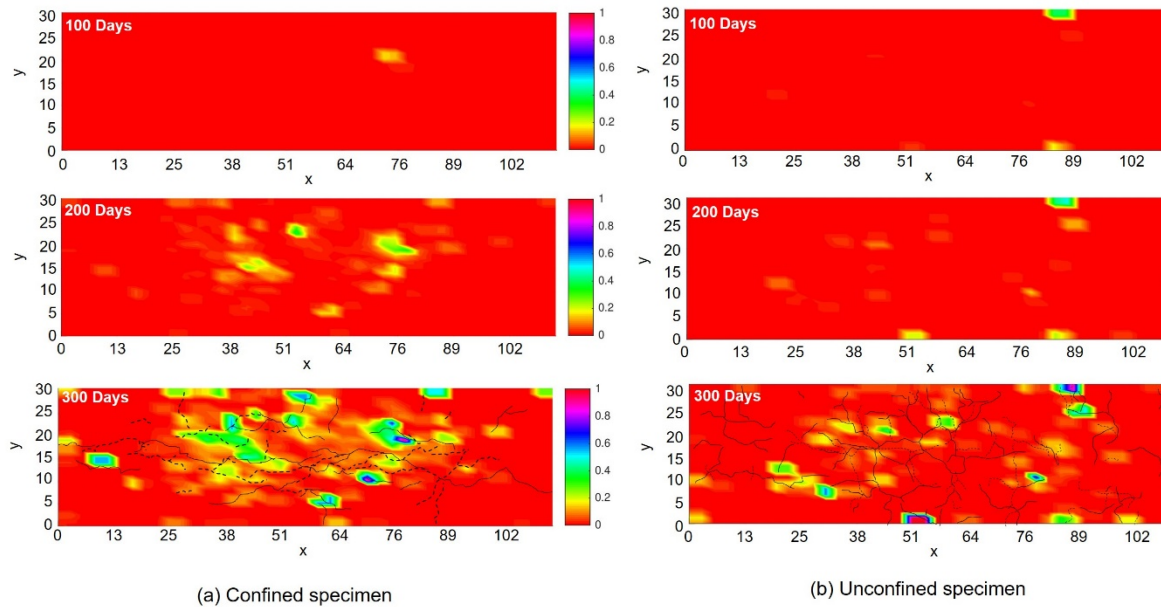


Figure 5.10 Source localization contours in the X-Y plane (top view).

Event distributions in the confined and unconfined specimens were generated along the Y direction. The examples of distributions are presented as histograms at 300 days in Figure 5.11. The value in each bin was normalized to the total number of hits. Therefore, the sum of the bar heights in a specific distance range shows the relative probability of occurrence of the AE signals (distribution of AE events) and the total sum of the bar heights is equal to unity. The AE events in the confined specimen are more concentrated in the middle width of the specimen than the unconfined specimen. The continuous vertical lines in the distributions illustrate the median of the event distribution along the Y direction, and the dashed vertical lines show first and third quartiles of the

event distribution along the Y direction. The first and third quartiles separate the lowest 25% of the data from the highest 75%, and the highest 25% of data from the lowest 75%, respectively.

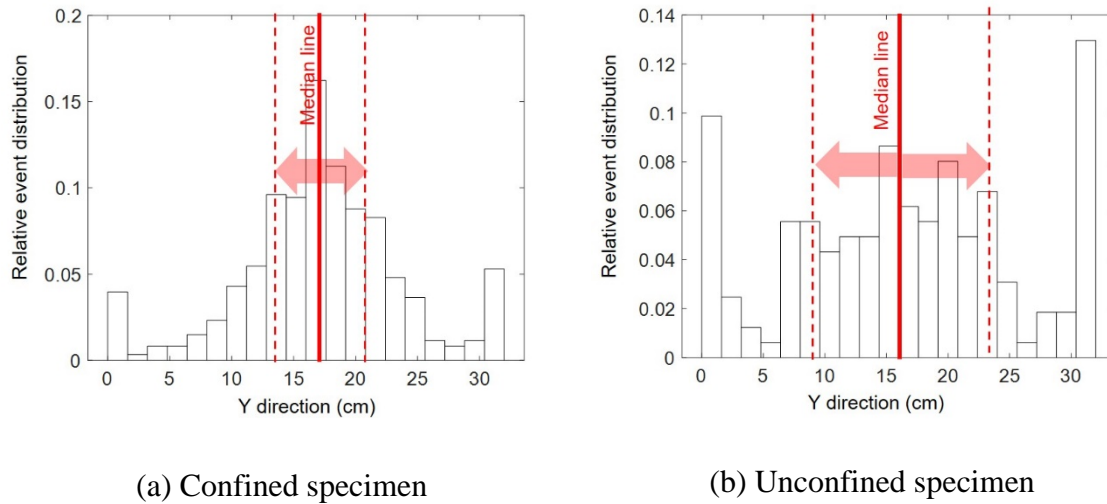


Figure 5.11 AE event distributions in Y direction at 300 days.

To evaluate and quantify the concentration and distribution of the AE events along the Y direction, two parameters are calculated in terms of the experiment time. The first is calculated by summing the bar heights attributed to the middle 50% portion of specimen widths (8 to 24 cm). This value shows the relative probability of occurrence of AE events at the mid-width of the specimens (referred to as middle relative probability (MRP) in this paper). In other words, MRP shows the ratio of the located events in the mid-section of dimension (mid-width and mid-height refer to the region between 8 and 24 cm of the associated dimensions).

The second parameter is the normalized interquartile range (IQR). This parameter is calculated by dividing the difference between first and third quartiles by the specimen dimension. This parameter shows the sharpness of event distribution in the mid-section of

dimension. For instance, MRP values for the confined and unconfined specimens for 300 days along the Y direction are 81% and 58%, respectively. This means that 81% of all events for the confined specimen are located between 8 and 24 cm. Furthermore, IQR values for the confined and unconfined specimens for 300 days along the Y direction are 22% and 43%, respectively, meaning that the distribution of the located AE events for the confined specimen is much sharper than for the unconfined. The larger amount and concentration of AE events for the confined specimen in the mid-width of the specimen illustrates the consistency of the AE data with the expansion observations, and the anisotropic damage caused by the confinement imposed by the reinforcing steel is likewise observed in the AE data.

To further evaluate the behavior of the specimens due to ASR, the aforementioned parameters were calculated in terms of the experiment time and are presented graphically in Figure 5.12. MRP values for the confined specimen are larger than the values for the unconfined specimen. In addition, IQR values for the confined specimen are much less than the IQR values for the unconfined specimen. This shows the concentration of stress in the middle-width of the confined specimen is much larger than the unconfined specimen. The stress concentration causes the accumulation of AE events in the middle region of the confined specimen with sharp event distribution. In the unconfined specimen, the amount of AE events in the middle region increases up to 220 days and decreases thereafter. The increase rate is sharper between 200 and 220 days, which coincides with a major jump in the cumulative signal strength (Figure 5.8b). The AE events that occurred between 200 and 220 days was mainly concentrated in the middle region of the Y direction. The IQR values decreased as the MRP values increase,

and vice versa. In other words, the more events in the mid-width of the specimen, the sharper the event distribution becomes.

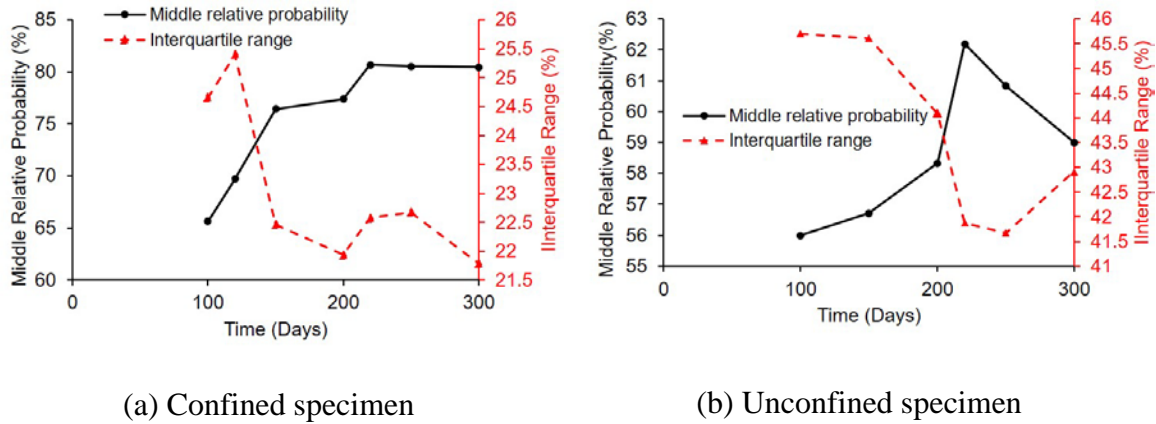


Figure 5.12 AE event distribution parameters along Y axis versus experiment time.

Comparing Figure 5.12a and b, it can be concluded that in the confined specimen, damage concentration in the middle-width of the specimen (Y direction) starts earlier than in the unconfined specimen. The concentration of AE events for the confined specimen is much denser along the Y-axis from an earlier time (100 days) than for the unconfined specimen. On the other hand, the AE events are distributed (damage) more uniformly at 100 days along the Y direction in the unconfined specimen.

Source location contours for the X-Z plane are presented in Figure 5.13. The continuous line shows the surface crack in the X-Z plane in the front view, according to Figure 5.1 (Y = 0). The dashed lines show the surface crack in the backside of the specimen (Y = 31 cm). In the figure, Z = 0 is the top surface of the specimen. Cracks oriented in the longitudinal dimension (X direction) are observed in both confined and unconfined specimens (Figure 5.13). These longitudinal cracks were caused due to anisotropic expansion. However, cracks also appeared along with the height of the

unconfined specimen (Z direction). In the confined specimen, fewer cracks are oriented in Z-direction (specimen height) than the unconfined specimen. This may be due to the longitudinal confinement provided by the steel reinforcement in the confined specimen along the X direction.

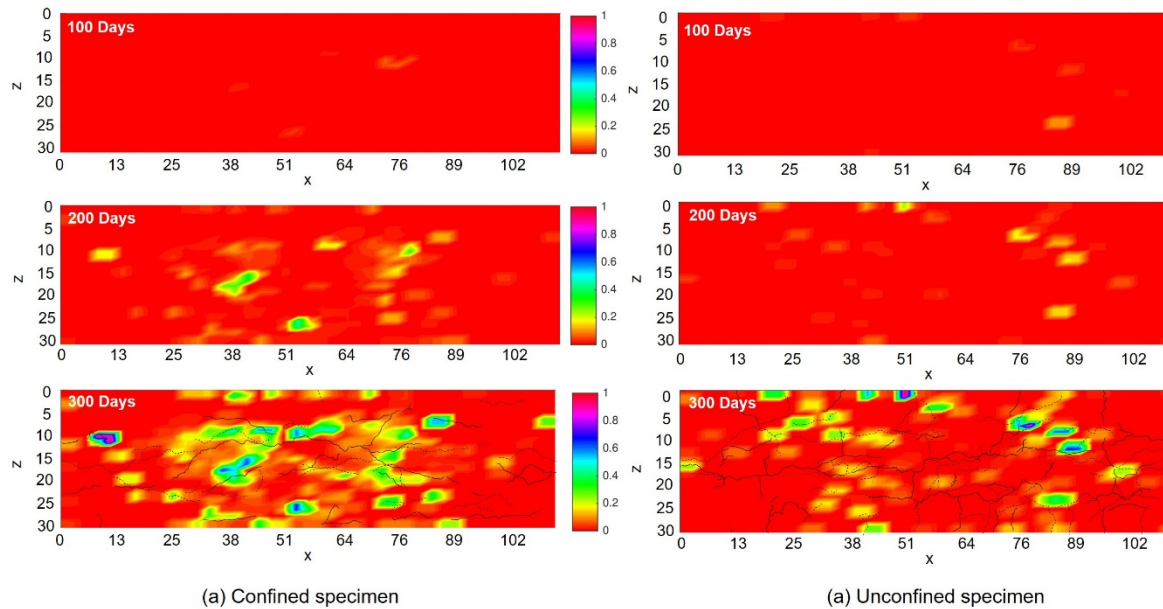


Figure 5.13 Source location contours in X-Z plane.

Distributions of the AE events located along the Z direction (specimen height) were also evaluated. An example of event distribution along the Z direction at 300 days is illustrated in Figure 5.14. The MRP values were calculated by summing the bar heights attributed to the middle 50% portion of specimen heights (8 to 24 cm). The MRP values at 300 days for the confined and unconfined specimens are 71% and 50%, and IQR values are 30% and 50%, respectively. This shows a larger concentration of the AE events at the mid-height of the confined specimen than the unconfined specimen. As mentioned, the casting direction may cause anisotropic expansion due to ASR in the specimen height. This expansion causes stress concentration in the confined specimen in

the Z direction. The transverse reinforcements may affect stress distribution in the Z direction. The variation of the MRP and IQR in terms of time for the confined and unconfined specimens is presented in Figure 5.15. In the confined specimen, the MRP increased at a larger rate up to 150 days, and the increasing rate diminishes thereafter. The events in the unconfined specimen do not show any trend of absolute increase or decrease, and the MRP values of the event fluctuate in terms of time. This shows that damage distributed more randomly along the height of the unconfined specimen compared to the confined specimen.

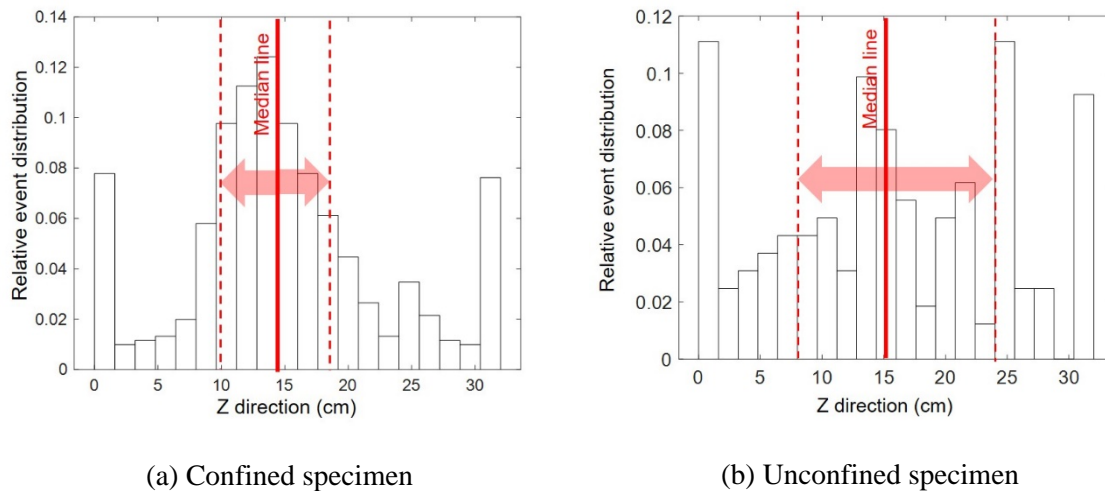
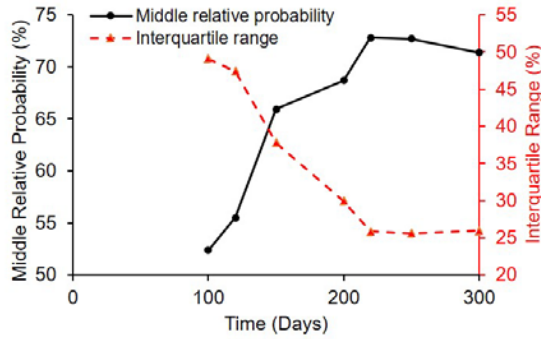
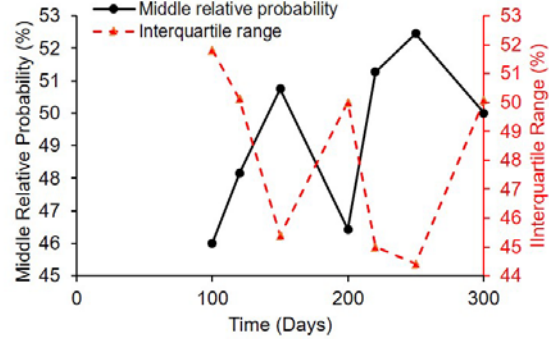


Figure 5.14 AE event distributions in Z direction at 300 days.



(a) Confined specimen



(b) Unconfined specimen

Figure 5.15 AE event distribution parameters along Z axis versus experiment time.

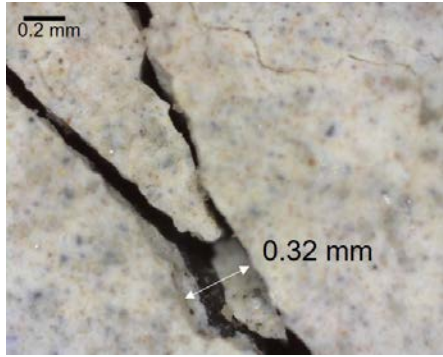
The MRP values for the confined specimen along the Z direction at 300 days are smaller than the corresponding value along the Y direction, which supports observations about anisotropy caused by the confinement along the specimen width.

5.5.3 Surface crack measurements

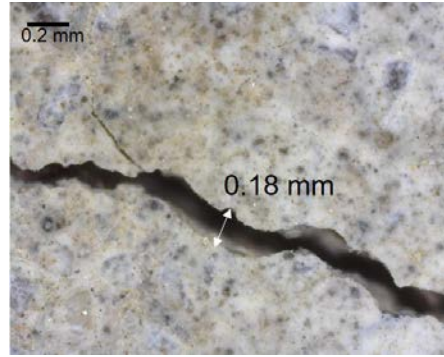
As mentioned, crack widths were measured beginning at 146 days after casting on the top surface of the specimens. Examples of crack measurements are shown in Figure 5.16. The figure depicts the cracks with the largest width at 269 and 300 days. The maximum crack widths were not necessarily attributed to the same crack and same location during the ASR process. Figure 5.16a and Figure 5.16c are related to a crack on the confined specimen, which was oriented in the X direction (parallel to the confinement plane). Figure 5.16b and Figure 5.16d are related to the cracks on the unconfined specimen, which were oriented in both X and Y directions. The magnification in the pictures is 184X. The widths of cracks for the top surface of the confined and unconfined specimens in terms of time are illustrated in Figure 5.17. As seen in the figures, the maximum crack widths on the top surface of the confined specimen are larger than those

on the unconfined specimen. Furthermore, there are more visible cracks observed on the top surface of the confined specimen than on the unconfined specimen at 146 days.

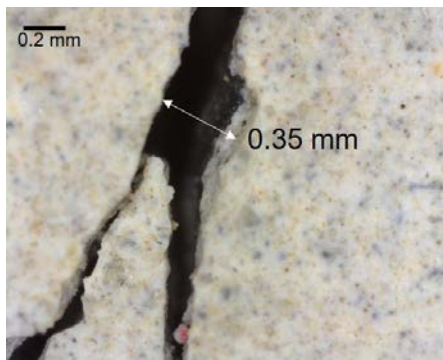
The wider crack widths found on the confined specimen illustrate a larger stress concentration in the mid-width of the specimen when compared to the unconfined specimen, which is expected as the reinforcement in the confined specimen caused more anisotropic resistance to the ASR expansion. The mid-width of the confined specimen was more expanded than the unconfined specimen, and stress more concentrated in the mid-width of the specimen, which had the least restraint. Consequently, this led to wider cracks on the surface of the confined specimen. In addition, the stress concentration due to reinforcement in the confined specimen caused a larger number of cracks in the specimen at 146 days. The wider cracks and larger number of cracks earlier in the ASR process in the confined specimen are consistent with the AE results.



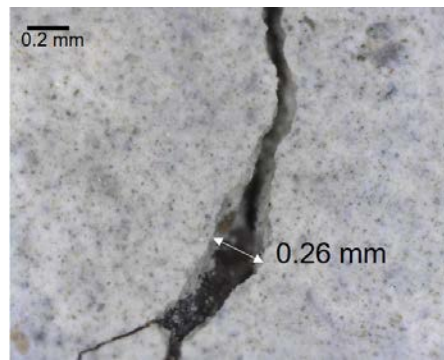
(a) Confined specimen at 269 days



(b) Unconfined specimen at 269 days



(c) Confined specimen at 300 days



(d) Unconfined specimen at 300 days

Figure 5.16 Maximum crack width measurement.

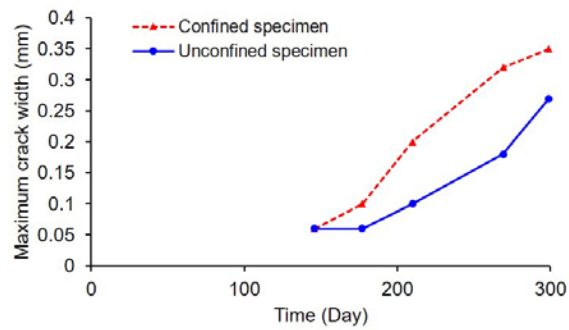


Figure 5.17 Crack quantification on top surface in terms of time.

5.6 Conclusion

The effect of confinement provided by longitudinal and transverse reinforcement was studied through data-driven methods. Unsupervised pattern recognition in combination with source location and statistical analysis were utilized. Three specimens were cast and exposed to high temperature and humidity for almost 300 days. Two specimens contained a reactive coarse aggregate, and the control specimen contained only nonreactive aggregates. One of the reactive specimens had confinement, provided through steel reinforcement, along with X and Z coordinates. The other reactive specimen and the nonreactive control specimen did not have any steel reinforcement. The ASR expansion was regularly measured with DEMEC gauge. In addition, the crack widths on the top surface of the specimens were measured. The main conclusions of the study are summarized as follows:

The effect of the boundary conditions on ASR damage distribution is clearly reflected in the AE data. Significantly more AE activity was detected in the confined specimen than in the unconfined specimen, with AE events were concentrated in the mid-width region of the confined specimen, and these events exhibited a relatively sharp distribution. The distribution of AE events for the unconfined specimen across the specimen width was more uniform. These observations in AE data correlate with anisotropic expansion in the confined specimen.

Damage from ASR in the confined specimen initiated earlier and was manifested in higher severity than the damage in the unconfined specimen; this can be observed from the AE data, expansion strains, and visible crack formation. The cumulative signal strength rate for the confined specimen increased abruptly in the 115 days (early stage of

ASR). This behavior was not observed for the unconfined specimen. The volumetric strains for the confined specimen were greater than for the unconfined specimen up to 260 days. This difference between the volumetric strains was mainly due to very large strains for the confined specimen in the Y direction. Furthermore, the number of cracks in the confined specimen were greater than the unconfined specimen at 146 days (start of the crack measurement), and maximum crack widths on the top surface of the confined specimen was larger than the crack widths of the unconfined specimen.

Acknowledgments: This research was partially supported by the U.S Department of Energy-Nuclear Energy University Program (NEUP) under the contract DE-NE0008544 and the U.S. Department of Energy Office of Science, Office of Basic Energy Sciences and Office of Biological and Environmental Research under Award Number DE-SC-00012530.

5.7 Reference

1. Barbosa, R.A.; Hansen, S.G.; Hansen, K.K.; Hoang, L.C.; Grelk, B. Influence of alkali-silica reaction and crack orientation on the uniaxial compressive strength of concrete cores from slab bridges. *Construction Building Materials* **2018**, *176*, 440-451.
2. Rajabipour, F.; Giannini, E.; Dunant, C.; Ideker, J.H.; Thomas, M.D. Alkali-silica reaction: Current understanding of the reaction mechanisms and the knowledge gaps. *Cement and Concrete Research* **2015**, *76*, 130-146.
3. Garcia-Diaz, E.; Riche, J.; Bulteel, D.; Vernet, C. Mechanism of damage for the alkali-silica reaction. *Cement Concrete Research* **2006**, *36*, 395-400.

4. Campos, A.; Lopez, C.M.; Blanco, A.; Aguado, A. Effects of an internal sulfate attack and an alkali-aggregate reaction in a concrete dam. *Construction Building Materials* **2018**, *166*, 668-683.
5. Plusquellec, G.; Geiker, M.R.; Lindgård, J.; De Weerd, K. Determining the free alkali metal content in concrete—case study of an asr-affected dam. *Cement and Concrete Research* **2018**, *105*, 111-125.
6. Blanco, A.; Pardo-Bosch, F.; Cavalaro, S.; Aguado, A. Lessons learned about the diagnosis of pathologies in concrete dams: 30 years of research and practice. *Construction Building Materials* **2019**, *197*, 356-368.
7. Schmidt, J.W.; Hansen, S.G.; Barbosa, R.A.; Henriksen, A. Novel shear capacity testing of asr damaged full scale concrete bridge. *Engineering Structures* **2014**, *79*, 365-374.
8. Lahdensivu, J.; Köliö, A.; Husaini, D. Alkali-silica reaction in southern-finland's bridges. *Case studies in construction materials* **2018**, *8*, 469-475.
9. Soltangharai, V.; Anay, R.; Hayes, N.; Assi, L.; Le Pape, Y.; Ma, Z.; Ziehl, P. Damage mechanism evaluation of large-scale concrete structures affected by alkali-silica reaction using acoustic emission. *Applied Sciences* **2018**, *8*, 2148.
10. Saouma, V.E.; Hariri-Ardebili, M.A. A proposed aging management program for alkali silica reactions in a nuclear power plant. *Nuclear Engineering Design* **2014**, *277*, 248-264.
11. Saouma, V.E.; Hariri-Ardebili, M.A. Seismic capacity and fragility analysis of an asr-affected nuclear containment vessel structure. *Nuclear Engineering* **2019**, *346*, 140-156.

12. Takakura, T.; Ishikawa, T.; Mitsuki, S.; Matsumoto, N.; Takiguchi, K.; Masuda, Y.; Nishiguchi, I. In *Investigation on the expansion value of turbine generator foundation affected by alkali-silica reaction*, Proceedings of 18th International Conference on Structural Mechanics in Reactor Technology, 2005.
13. Tcherner, J.; Aziz, T. In *Effects of aar on seismic assessment of nuclear power plants for life extensions*, Proceedings of the 20th International Conference on Structural Mechanics in Reactor Technology (SMiRT), Espoo, Finland, 2009; pp 9-14.
14. Hariri-Ardebili, M.A.; Saouma, V.E. Sensitivity and uncertainty analysis of aar affected reinforced concrete shear walls. *Engineering Structures* **2018**, *172*, 334-345.
15. Islam, M.S.; Ghafoori, N. A new approach to evaluate alkali-silica reactivity using loss in concrete stiffness. *Construction Building Materials* **2018**, *167*, 578-586.
16. Abdelrahman, M.; ElBatanouny, M.K.; Ziehl, P.; Fasl, J.; Larosche, C.J.; Fraczek, J. Classification of alkali-silica reaction damage using acoustic emission: A proof-of-concept study. *Construction Building Materials* **2015**, *95*, 406-413.
17. Allard, A.; Bilodeau, S.; Pissot, F.; Fournier, B.; Bastien, J.; Bissonnette, B. Expansive behavior of thick concrete slabs affected by alkali-silica reaction (asr). *Construction Building Materials* **2018**, *171*, 421-436.
18. Sinno, N.; Shehata, M.H. Effect of sample geometry and aggregate type on expansion due to alkali-silica reaction. *Construction Building Materials* **2019**, *209*, 738-747.

19. Hayes, N.W.; Gui, Q.; Abd-Elssamd, A.; Le Pape, Y.; Giorla, A.B.; Le Pape, S.; Giannini, E.R.; Ma, Z.J. Monitoring alkali-silica reaction significance in nuclear concrete structural members. *Journal of Advanced Concrete Technology* **2018**, *16*, 179-190.
20. Thomas, M.D.A.; Folliard, K.J.; Fournier, B.; Rivard, P.; Drimalas, T.; Garber, S.I. *Methods for evaluating and treating asr-affected structures: Results of field application and demonstration projects—volume ii: Details of field applications and analysis*; US Department of Transportation, Federal Highway Administration: 2013.
21. Seo, J.; Wacker, J.P.; Duque, L. *Evaluating the use of drones for timber bridge inspection*; General Technical Report FPL-GTR-258; Department of Agriculture, Forest Service, Forest Products Laboratory: Madison, WI, U.S., 2018; pp 1-152.
22. Zink, J.; Lovelace, B. *Unmanned aerial vehicle bridge inspection demonstration project*; MN/RC 2015-40; Minnesota Department of Transportation, Office of Transportation System Management: 2015.
23. Yang, C.-H.; Wen, M.-C.; Chen, Y.-C.; Kang, S.-C. In *An optimized unmanned aerial system for bridge inspection*, ISARC. Proceedings of the International Symposium on Automation and Robotics in Construction, 2015; IAARC Publications: p 1.
24. Giannini, E.R.; Folliard, K.J.; Zhu, J.; Bayrak, O.; Kreitman, K.; Webb, Z.; Hanson, B. *Non-destructive evaluation of in-service concrete structures affected by alkali-silica reaction (asr) or delayed ettringite formation (def)—final report, part i*; 2013.

25. Mahadevan, S.; Agarwal, V.; Neal, K.; Nath, P.; Bao, Y.; Cai, G.; Orme, P.; Adams, D.; Kosson, D. *A demonstration of concrete structural health monitoring framework for degradation due to alkali-silica reaction*; Idaho National Lab.(INL), Idaho Falls, ID (United States): 2016.
26. Teramoto, A.; Watanabe, M.; Murakami, R.; Ohkubo, T. Visualization of internal crack growth due to alkali-silica reaction using digital image correlation. *Construction Building Materials* **2018**, *190*, 851-860.
27. Kim, G.; Park, S.; Kim, J.-Y.; Kurtis, K.E.; Hayes, N.W.; Jacobs, L.J. Nonlinear rayleigh surface waves to characterize microscale damage due to alkali-silica reaction (asr) in full-scale, nuclear concrete specimens. *Construction Building Materials* **2018**, *186*, 1114-1118.
28. Lokajíček, T.; Přikryl, R.; Šachlová, Š.; Kuchařová, A. Acoustic emission monitoring of crack formation during alkali silica reactivity accelerated mortar bar test. *Engineering geology* **2017**, *220*, 175-182.
29. Rivard, P.; Saint-Pierre, F. Assessing alkali-silica reaction damage to concrete with non-destructive methods: From the lab to the field. *Construction Building Materials* **2009**, *23*, 902-909.
30. Sargolzahi, M.; Kodjo, S.A.; Rivard, P.; Rhazi, J. Effectiveness of nondestructive testing for the evaluation of alkali-silica reaction in concrete. *Construction Building Materials* **2010**, *24*, 1398-1403.
31. Farnam, Y.; Geiker, M.R.; Bentz, D.; Weiss, J. Acoustic emission waveform characterization of crack origin and mode in fractured and asr damaged concrete. *Cement and Concrete Composites* **2015**, *60*, 135-145.

32. Weise, F.; Volland, K.; Pirskawetz, S.; Meinel, D. In *Innovative measurement techniques for characterising internal damage processes in concrete due to asr*, Proceedings of the International Conference on Alkali Aggregate Reaction (ICAAR), University of Texas, Austin, TX, USA, 2012; pp 20-25.
33. Shiotani, T.; Osawa, S.; Kobayashi, Y.; Momoki, S. Application of 3d ae tomography for triaxial tests of rocky specimens. In *Proceedings of the European Working Group on Acoustic Emission*, Dresden, Germany, 2014; pp 3-5.
34. Shiotani, T.; Nishida, T.; Nakayama, H.; Asaue, H.; Chang, K.-C.; Miyagawa, T.; Kobayashi, Y. Fatigue failure evaluation of rc bridge deck in wheel loading test by ae tomography. In *Advances in acoustic emission technology*, Springer: 2017; pp 251-264.
35. ElBatanouny, M.K.; Ziehl, P.H.; Larosche, A.; Mangual, J.; Matta, F.; Nanni, A. Acoustic emission monitoring for assessment of prestressed concrete beams. *Construction Building Materials* **2014**, *58*, 46-53.
36. Liaudat, J.; Carol, I.; López, C.M.; Saouma, V.E. Asr expansions in concrete under triaxial confinement. *Cement Concrete Composites* **2018**, *86*, 160-170.
37. Morenon, P.; Multon, S.; Sellier, A.; Grimal, E.; Hamon, F.; Bourdarot, E. Impact of stresses and restraints on asr expansion. *Construction Building Materials* **2017**, *140*, 58-74.
38. Karthik, M.M.; Mander, J.B.; Hurlbauss, S. Deterioration data of a large-scale reinforced concrete specimen with severe asr/def deterioration. *Construction Building Materials* **2016**, *124*, 20-30.

39. Saouma, V.E.; Hariri-Ardebili, M.A.; Le Pape, Y.; Balaji, R. Effect of alkali-silica reaction on the shear strength of reinforced concrete structural members. A numerical and statistical study. *Nuclear Engineering Design* **2016**, *310*, 295-310.
40. Gorga, R.; Sanchez, L.; Martín-Pérez, B. Fe approach to perform the condition assessment of a concrete overpass damaged by asr after 50 years in service. *Engineering Structures* **2018**, *177*, 133-146.
41. Tan, P.-N.; Steinbach, M.; Kumar, V. Classification: Basic concepts, decision trees, and model evaluation. In *Introduction to data mining*, Pearson Addison-Wesley: 2006.
42. Murtagh, F.; Legendre, P. Ward's hierarchical agglomerative clustering method: Which algorithms implement ward's criterion? *Journal of classification* **2014**, *31*, 274-295.
43. Soltangharaei, V.; Anay, R.; Assi, L.; Ziehl, P.; Matta, F. In *Damage identification in cement paste amended with carbon nanotubes*, AIP Conference Proceedings, 2018; AIP Publishing: p 030006.
44. Ge, M. Analysis of source location algorithms part 1: Overview and non-iterative methods. *Acoustic Emission* **2003**, *21*, 14-24.
45. Mistras-Group. Express-8 ae system user manual. Princeton Junction, NJ, USA, 2014.
46. Carpinteri, A.; Xu, J.; Lacidogna, G.; Manuello, A. Reliable onset time determination and source location of acoustic emissions in concrete structures. *Cement concrete composites* **2012**, *34*, 529-537.

47. Madarshahian, R.; Ziehl, P.; Caicedo, J.M. Acoustic emission bayesian source location: Onset time challenge. *Mechanical Systems Signal Processing* **2019**, *123*, 483-495.
48. Bai, F.; Gagar, D.; Foote, P.; Zhao, Y. Comparison of alternatives to amplitude thresholding for onset detection of acoustic emission signals. *Mechanical Systems Signal Processing* **2017**, *84*, 717-730.
49. Van Steen, C.; Pahlavan, L.; Wevers, M.; Verstrynge, E. Localisation and characterisation of corrosion damage in reinforced concrete by means of acoustic emission and x-ray computed tomography. *Construction Building Materials* **2019**, *197*, 21-29.
50. Akaike, H. Information theory and an extension of the maximum likelihood principle. In *Selected papers of hirotugu akaike*, Springer: 1998; pp 199-213.
51. Ge, M. Analysis of source location algorithms: Part 2. Iterative methods. *Journal of Acoustic Emission* **2003**, *21*, 29-51.
52. Dennis Jr, J.E.; Welsch, R.E. Techniques for nonlinear least squares and robust regression. *Communications in Statistics-Simulation Computation* **1978**, *7*, 345-359.
53. Torkjazi, M.; Mirjafari, P.S.; Poorzahedy, H. Reliability-based network flow estimation with day-to-day variation: A model validation on real large-scale urban networks. *Journal of Intelligent Transportation Systems* **2018**, *22*, 121-143.
54. Khan, S.M.; Islam, S.; Khan, M.Z.; Dey, K.; Chowdhury, M.; Huynh, N.; Torkjazi, M. Development of statewide annual average daily traffic estimation

- model from short-term counts: A comparative study for south carolina. *Transportation Research Record* **2018**, 2672, 55-64.
55. Smaoui, N.; Bérubé, M.-A.; Fournier, B.; Bissonnette, B. Influence of specimen geometry, orientation of casting plane, and mode of concrete consolidation on expansion due to asr. *Cement, concrete aggregates* **2004**, 26, 1-13.
56. Xargay, H.; Folino, P.; Nuñez, N.; Gómez, M.; Caggiano, A.; Martinelli, E. Acoustic emission behavior of thermally damaged self-compacting high strength fiber reinforced concrete. *Construction Building Materials* **2018**, 187, 519-530.
57. Aggelis, D.; Soulioti, D.; Gatselou, E.; Barkoula, N.-M.; Matikas, T. Monitoring of the mechanical behavior of concrete with chemically treated steel fibers by acoustic emission. *Construction Building Materials* **2013**, 48, 1255-1260.
58. Lacidogna, G.; Piana, G.; Carpinteri, A. Acoustic emission and modal frequency variation in concrete specimens under four-point bending. *Applied Science* **2017**, 7, 339.
59. Landis, E.N.; Shah, S.P. Frequency-dependent stress wave attenuation in cement-based materials. *Journal of Engineering Mechanics* **1995**, 121, 737-743.
60. Ponce, J.; Batic, O.R. Different manifestations of the alkali-silica reaction in concrete according to the reaction kinetics of the reactive aggregate. *Cement Concrete Research* **2006**, 36, 1148-1156.
61. Pan, J.; Feng, Y.; Wang, J.; Sun, Q.; Zhang, C.; Owen, D. Modeling of alkali-silica reaction in concrete: A review. *Frontiers of Structural Civil Engineering* **2012**, 6, 1-18.

Chapter 6

Investigation of Temporal Evolution of AE Data for Concrete Specimens Affected by ASR Using Information entropy, b-value, Regression analysis, and Gradient of Cumulative Signal Strength¹

¹ Vafa Soltangharai, Rafal Anay, Li Ai, and, Paul Ziehl, Temporal evaluation of ASR cracking in concrete specimens using acoustic emission. To be submitted to *Construction Building and Material*.

6.1 Abstract

This study investigates the efficacy of differing information entropy calculation approaches for concrete structures undergoing Alkali-Silica Reaction (ASR) induced damage. In prior work, information entropy has only been utilized to better understand damage in metallic structures under external loading. To our knowledge, no research has been published regarding information entropy for concrete structures affected by ASR. This scientific gap is addressed in this paper. The innovation lies in using coefficients of determination instead of b-values for damage identification. The entropy results show that the randomness of events increases at the earlier stage of ASR, which is expected due to the microcrack formation and decreases at the later stage due to the formation of macrocracks. Moreover, a correlation is observed between the coefficients of determination and the evolution of cumulative signal strength.

Keywords: Acoustic emission; alkali-silica reaction; b-value analysis; damage evaluation; information entropy; intensity analysis

6.2 Introduction

One potential source of degradation in concrete structures is Alkali-Silica Reaction (ASR) [1-5]. This chemical reaction occurs between siliceous minerals in some aggregates and alkali hydroxides in pore solution [6,7]. The chemical product is a hygroscopic material, called Alkali-Silica gel, which absorbs water causing its volume to increase. The raise in volume of gel induces stress to aggregates and the cement matrix causing cracking and damage [3,8]. The chemical reaction gradually continues for several years. In a laboratory, aging caused by ASR is usually accelerated by exposing concrete specimens to high temperatures and humidity exceeding 80% [8].

Several methods have been employed to detect ASR and the corresponding damage in concrete structures including visual inspection, petrographic analysis, demountable mechanical strain gauges (DEMEC gauge), and cracking index [9-14]. These methods are not always efficient in early damage detection. In addition, some (e.g. coring, petrographic analysis enabled through coring) are sometimes prohibited in nuclear structures.

New nondestructive methods and health monitoring techniques such as digital image correlation (DIC) [15], ultrasonic pulse velocity (UPV) [16], impact-echo [17], and acoustic emission (AE) [18-21] are alternatives for ASR damage detection. These methods also have limitations. For instance, DIC is a surface imaging method, which may not be preferable for concrete shear walls, where most of the expansion occurs out of plane. In addition, using DIC in the field presents challenges associated with lighting and other considerations. In the UPV method, the emitter and receiver sensors are generally located across from each other on two sides of the structure. This causes a restriction in monitoring for some structures, particularly those that are only accessible from one side. Furthermore, the frequency ranges of emitted signals are often not high enough to reliably capture disturbance caused by small-scale damage (e.g. microcracking in the paste).

AE is a passive structural health monitoring technique, which can be employed to continuously monitor structures. AE piezometric sensors are sensitive to damage initiation and growth and can be attached on one side of structures. The sensors detect and record elastic stress waves emitted due to crack formation. In addition, source localization is feasible with an appropriate sensor layout. Recently, research has been conducted to employ AE for monitoring ASR-induced damage [18-20], primarily focused on small-scale specimens without reinforcement or confinement. Correlations between features of AE

waveform data such as cumulative signal strength (CSS) and ASR expansion have been observed. Conventional parametric AE features such as signal strength and amplitude are highly dependent on source to sensor distance and material considerations. Therefore, researchers seek dimensionally independent parameters to evaluate damage in structures using AE.

Along these lines, Shannon entropy (information entropy) has recently been investigated for damage evaluation of metallic material under fatigue loading [22-29]. Before Shannon entropy, thermodynamic entropy was employed for evaluation of damage in metallic structures under fatigue and corrosion fatigue [30-33]. The main problem with thermodynamic entropy is the measurement challenge of hysteresis energy, particularly in large-scale structures [23]. Another issue is the relatively minor temperature variation in metallic structures under high cycle fatigue testing [23]. Therefore, researchers have proposed using AE and Shannon entropy in lieu of thermodynamic entropy. Kahirdeh et al. [23], utilized information entropy and relative entropy to study the damage evolution of bone-shaped aluminum specimens under cyclic loading. The trend of standardized cumulative entropy was similar to the Vickers hardness trend. Chai et al. [22] calculated Shannon entropy for hits recorded during a fatigue crack growth test conducted on a notched alloyed steel plate and a monotonic three-point bending test conducted on a small stainless steel beam. The results indicated that Shannon entropies for AE signals were useful to inform discrimination between damage stages, while the temporal distribution of amplitude did not show any clear trend.

Although some studies have been conducted regarding an application of information entropy as a damage criterion for metallic material under cyclic loading, to our

knowledge, research has not been published regarding information entropy for cementitious materials under different loading conditions or the ASR process. Therefore, in this study, information entropy results for damage evaluation of cementitious material with different scales and under different stress boundary conditions are presented. The primary focus is evaluating Shannon entropy as a damage indicator for concrete structures affected by ASR without external loading.

Several AE-based analyses, such as intensity and b-value analyses have been proposed and employed in the previous literature to evaluate damage in structures under external loading [34-41]. Despite a large amount of literature regarding the application of intensity and b-value analyses for structures under loading, limited research has been published about using these analyses for damage evaluation of structures under ASR-induced stresses [18]. Moreover, the efficiency of these analyses has not been evaluated for damage evaluation of concrete structures under ASR expansion. This gap in the literature is also covered in this paper in addition to information entropy.

6.3 Test setup

In this study, AE data for three types of specimens having different scales were investigated. Each specimen type has a different test setup and boundary conditions. The medium-scale specimens were concrete blocks with dimensions of 305 mm × 305 mm × 1120 mm with differing reinforcement conditions. Two specimens possessed reactive coarse aggregates (reactive specimens), and one served as a non-reactive control specimen. One of the reactive specimens had steel reinforcement along two dimensions (length and depth), which is referred to as the medium-scale confined specimen in this paper. The other reactive specimen did not have any steel reinforcement and is referred to as the medium-

scale unconfined specimen. The control specimen was also unreinforced. Only AE data related to the reactive specimens are considered for analysis. Ten broadband AE sensors were mounted on the surfaces of the reactive specimens. A 24-channel Micro-II Express, manufactured by MISTRAS Group, Inc. (Princeton Junction, NJ, USA), was utilized as a data acquisition system. The sampling rate was 5000 kHz, pre-trigger time was 256 μ s, HDT (hit definition time) PDT (peak definition time), and HLT (hit lockout time) were 400 μ s, 200 μ s, and 200 μ s, respectively. Bandpass digital and analog filters with a frequency range of 20-400 kHz were set in the data acquisition system. A background test was conducted before the test, and the threshold was set at 32 dB.

Also included in the study are three large-scale concrete specimens with dimensions of 3500 mm \times 3000 mm \times 1000 mm. Similar to the medium-scale specimens, two specimens were reactive, and one was a non-reactive control specimen. The concrete mixture for the reactive and control specimens was the same. In the control specimen, LiNO₃ was added to deter the ASR reaction. The reactive specimens had reinforcement on the top and bottom of the specimens. One of the reactive specimens was restrained in a rigid steel frame, which is referred to as the large-scale confined specimen. The other reactive specimen was not enclosed by a steel frame, namely the large-scale unconfined specimen in this study. The test setup details are explained in [42]. In this study, the AE data for the reactive specimens is investigated. Three broadband AE sensors were embedded in the reactive specimens before casting. A 16-channel Sensor Highway II (SHII), manufactured by MISTRAS Group, Inc. (Princeton Junction, NJ, USA), was utilized as the data acquisition system. The sampling rate was set to 1000 kHz, pre-trigger

time was 256 μ s, HDT, HLT, and PDT were 400 μ s, 200 μ s, and 200 μ s. The initial data acquisition threshold was 32 dB.

The third specimen investigated in this study is a relatively small cement paste specimen (referred to as the small-scale specimen) with dimensions of 38.1mm \times 38.1mm \times 152.4mm loaded in uniaxial compression. Eight micro-30 resonant sensors were attached to the specimen surfaces. A 16-channel DiSP system manufactured by MISTRAS Group, Inc. (Princeton Junction, New Jersey) was utilized for data acquisition. Pre-amplifiers with a 40 dB gain and bandpass internal filters with the frequency range of 100 to 1200 kHz were connected to the sensors. The sampling rate was set to 1000 kHz, pre-trigger time was 256 μ s, and HDT, HLT, and PDT were 400 μ s, 200 μ s, and 200 μ s. The initial data acquisition threshold was 32 dB.

6.4 Analysis method and procedure

AE data was utilized to calculate signal entropies in all three specimen types. Conventional features such as amplitude and signal strength were used in addition to entropies to calculate AE-based damage indices. Methods for calculating signal entropies and damage indices are presented in the following sub-sections.

6.4.1 Signal entropy

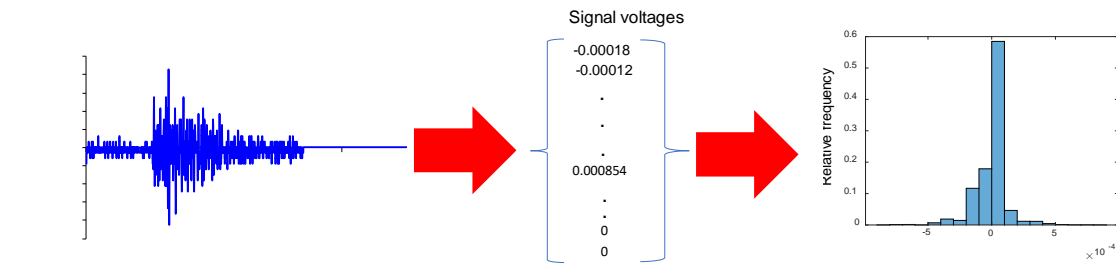
Three methods for calculating signal entropy may be found in literature, and they have been employed for fatigue loading [22,23,43-45]. The methods, which include voltage amplitude entropy, feature entropy, and fast Fourier transform (FFT) entropy, are presented in this section.

Voltage entropy is calculated based on the distribution of amplitude voltages of AE signals. The voltage amplitudes of each AE signal are used to develop a histogram of the signal. The bin size is recommended to be close to the resolution of AE data acquisition systems [22]. The resulting histogram contains several bars corresponding to the bins. Each bar shows the relative frequency of voltages within a bin. Then, voltage entropy is calculated according to the Shannon entropy equation:

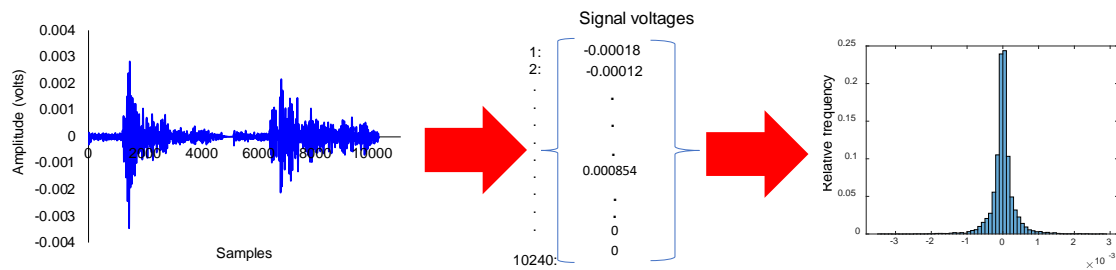
$$Entropy = - \sum_{i=1}^n P(x_i) * \log (P(x_i)) \quad (6.1)$$

In this equation, n is the number of bins in each signal; x_i represents the bins defined in each signal; and $P(x_i)$ is the relative frequency of each bin calculated according to the signal histogram. The procedure is shown in Figure 6.1. With this method, it is assumed that the voltage value changes constantly and independently between samples. There are two approaches for calculating the entropy. One approach is calculating the entropy for each signal, namely discrete voltage entropy (DVE) in this paper (Figure 6.1a). The other

approach is calculating the entropy, based on all signal voltages up to the desired experiment time. In this method, the amplitude voltages of all signals up to the desired time are used to derive a histogram and calculate an entropy. This method is referred to as global voltage entropy (GVE). In Figure 6.1b, the signal voltages for two signals were used for developing a histogram and calculating associated entropy. The next entropy is calculated by using three signals. This is continued until all signals are included in the calculation.



(a) Discrete voltage entropy



(b) Global voltage entropy

Figure 6.1 Entropy calculation using signal amplitude voltage

Another method is referred to as counts-entropy. There are two methods for calculating counts-entropy. For both calculation methods, it is assumed that each count is independent of other counts. In the first calculation method, the probability is calculated by dividing the counts of a signal corresponding to the desired time over the cumulative counts up to that time. Then counts-entropy is calculated by using Shannon entropy Eq.

(6.1). This method is referred to as CE. CE will be updated when a new signal is received. In the second procedure, the cumulative distribution function (CDF) for counts up to the desired time is estimated by using the empirical CDF method [43] and the corresponding probability distribution function (PDF) is derived. The entropy is estimated using the probability distribution for each bin using Eq. (6.1). This method is referred to as CE_CDF in this study. The procedure is repeated when a new signal is received.

The third method, FFT Entropy, is calculated by using FFT spectra of signals. The AE signals are converted into the frequency domains using FFT, resulting in FFT spectra. The spectra are normalized by the total energies of the signals. The normalized spectra are considered as probability distributions in the frequency domain. Then, Shannon entropy is estimated from each spectrum. The procedure is presented in Figure 6.2.

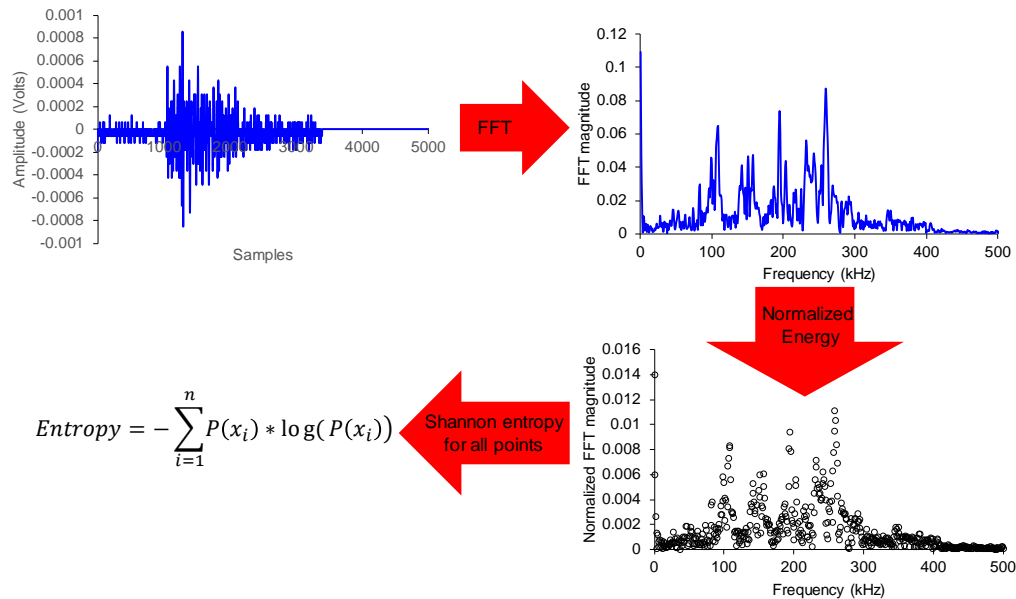


Figure 6.2 FFT Entropy

6.4.2 AE damage index methods

One of the common methods for deriving damage indices based on AE data is intensity analysis. This analysis has been utilized for damage level identification for different structures under loading [46-50]. In this analysis, two parameters of the historic index (HI) and severity (S_r) are calculated. The parameters are presented as follows:

$$H(t) = \frac{N}{N-K} \frac{\sum_{i=k+1}^N S_{oi}}{\sum_{i=1}^N S_{oi}} \quad (6.2)$$

$$S_r = \frac{1}{J} \sum_{i=1}^{i=50} S_{oi} \quad (6.3)$$

In the above equations, N is the number of hits up to the desired time and K and J are empirically derived parameters. Although this method has been utilized for different structures, especially structures under external loading, the empirical dependency of parameters causes limitations. Researchers have proposed different parameters for the intensity analysis [41,48,50], therefore, comparisons between analysis results from case to case are challenging.

In the case of ASR, the variability between empirical parameters for the intensity analysis is even more pronounced, because AE temporal distribution depends on several factors such as stress boundary conditions, the concrete mixture, aggregate types, and environmental conditions (e.g. temperature and humidity) in addition to specimen size, sensor types, and sensor layout.

The rate change in cumulative signal strength (CSS) can be a proper parameter to evaluate damage in structures based on AE data. The CSS rate is roughly estimated by HI in the intensity analysis. The HI in each desired time is an average ratio between the CSS for the hits adjacent to the desired time to the CSS for the hits from the beginning of the

test up to the desired time. Therefore, HI directly depends on the AE data distribution, which is not uniform during ASR and varied for different structures.

In this study, gradients of normalized CSS of the medium-scale unconfined and confined specimens are employed for comparison purposes and observation of temporal evolution in data. Numerical gradients using centered differentiation is used according to the following equation.

$$G(i) = \frac{CSS(i+1) - CSS(i-1)}{2} \quad (6.4)$$

To reduce the dependency of the gradient on the AE distribution, linear interpolation is used to derive samples corresponding to the desired time with a constant sampling rate. Then, resulting CSS is used for calculating the gradient in each sample (i). The sampling rate in this study is one sample per day.

Another common method for damage detection using AE is b-value analysis. This method is based on the Gutenberg-Richter equation in seismology [36]. The modified version of the equation has been utilized in AE for damage identification [35-37]. An almost-linear distribution between the logarithm of AE amplitude frequency and AE amplitude is derived for a data set, and the slope of a fitted line to the distribution is referred to as the b-value. A smaller absolute b-value shows the contribution of AE data with higher amplitudes and is expected to be related to damage formation. The b-values are usually calculated using the following equation:

$$\log N = a - b \left(\frac{A_{dB}}{20} \right) \quad (6.5)$$

Where N is the number of AE hits with a magnitude equal to or greater than an amplitude of a hit. Linear regression is conducted between the $\log N$ and $A_{dB}/20$ to calculate model parameters (a and b). All data are separated into a specific subset number. Then, the

b-values are calculated separately in each subset. This method is referred to as the incremental b-value (Inc-b).

The coefficient of determination for each b-value is calculated. This factor may also be considered as a damage identification criterion because it is expected that severe damage formation emits AE signals with large amplitudes. The AE signals with large amplitudes cause deviation from mostly linear amplitude- $\log N$ distribution and consequently, reduction in coefficients of determination.

The $\log N$ versus amplitude distribution is usually not perfectly linear, especially for large and small amplitudes (upper and lower part of the distribution). Therefore, some researchers have proposed to consider upper and lower bands for the dataset [35,51,52]. This method is referred to as Improved b-value in the literature. If it is calculated based on incremental intervals and is referred to as the incrementally improved b-value (Inc-Ib). The upper limit and lower limit are defined by A_2 and A_1 .

$$A_2 = \mu - \alpha_1\sigma \text{ and } A_1 = \mu + \alpha_2\sigma \quad (6.6)$$

The slope between upper and lower limits in $\log N$ versus amplitude distribution results in an improved b-value (Ib). This calculation is based on the assumption that the distribution between upper and lower limits is linear.

$$Ib = \frac{[\log A_2 - \log A_1]}{[A_2 - A_1]} \quad (6.7)$$

In this study, instead of using the above equation, average (μ) and standard deviation (σ) of each data subset is calculated, and the data, which exceed $\mu + \alpha_2\sigma$ or are less than $\mu - \alpha_1\sigma$, are deleted. Then, b-values for the remaining data are calculated. The parameters α_1 and α_2 range from 0.5 to 2. In this paper, α_1 and α_2 are set equal to unity.

6.5 Results

In this section, results for signal entropy and damage indices are presented. Entropies were first calculated for the medium-scale specimens. Then, entropies were calculated for large-scale and small-scale specimens and compared to the results for the medium-scale specimens. Finally, AE-based damage indices were calculated for the medium-scale specimens.

6.5.1 Entropy for the medium-scale specimens

Discrete voltage entropy was calculated for the medium-scale specimens. The results for the confined and unconfined specimen are presented in Figure 6.3.

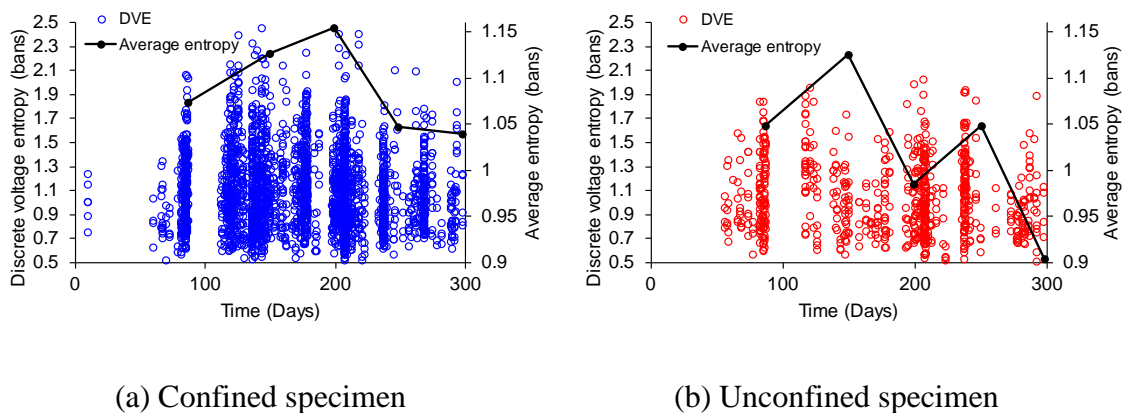


Figure 6.3 Discrete voltage entropy (DVE) for medium-scale specimens, bin size: 0.0001 volts

As seen in Figure 6.3, the range of entropy values is almost same for both specimens. The solid black line shows the average entropy in 50-day intervals. The average entropies are presented in the secondary vertical axis to show the trend of curves better. Generally, the variation of the average entropy for both specimens were minor. The average entropy in the confined specimen increased up to 200 days and then decreased, while in the unconfined specimen, it increased up to 150 days and then had a generally decreasing

trend despite some fluctuations. Figure 6.4 shows the average entropy for the 50-day intervals when using different bin sizes. Although slight variations in entropy values with different bin sizes are observed, trends of entropy values with different bin sizes are similar; showing the trends of voltage entropies to be insensitive to the bin size.

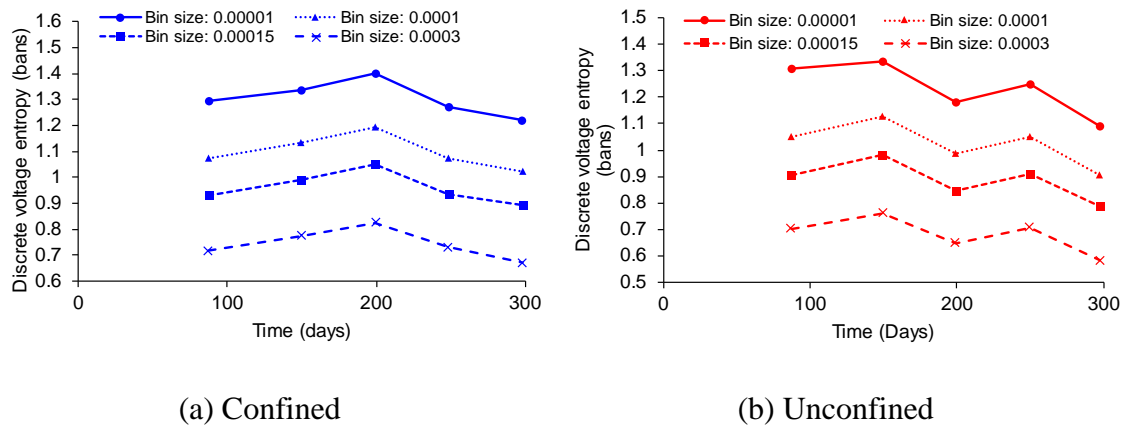


Figure 6.4 Discrete voltage entropy for medium-scale specimens using different bin sizes

Global voltage entropy was calculated for each desired time by considering all previously recorded data from the beginning of the test. The results for the bin size of 0.0001 volts are shown in Figure 6.5. In the confined specimen, the GVE increased up to 200 days and then it remained almost constant. In the unconfined specimen, the GVE increased up to 123 days and decreased slightly after that. The GVE remained almost constant after 180 days in the unconfined specimen. The trends of GVE in both specimens were similar to the patterns observed in DVE curves. At first, the entropy had an increasing trend and then a decreasing trend. Furthermore, the GVE range for the two specimens was similar, although the peak value for the confined specimen was slightly larger than the unconfined specimen.

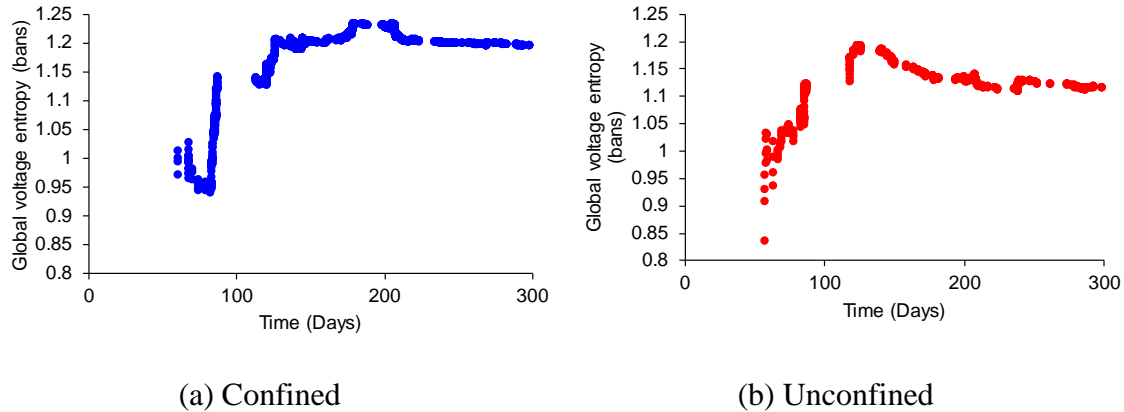


Figure 6.5 Global voltage entropy (GVE) for medium-scale specimens

The second entropy method is calculating the entropy of counts, namely counts-entropy. Two different approaches were utilized in this paper for calculating probability distribution. The results for the first method (as mentioned in section 6.3.1) are illustrated in Figure 6.6. As seen in the figure, the CE rates were much higher earlier in the experiment than later. The CE rates for both specimens declined by specimen age. The CE variation in the confined specimen was almost constant after 200 days, while CE variation in the unconfined specimen was constant after 237 days. The CE values for the confined specimen were more than for the unconfined specimens. The reason might be related to the dependency of this method on the number of signals, which were larger for the confined specimen.

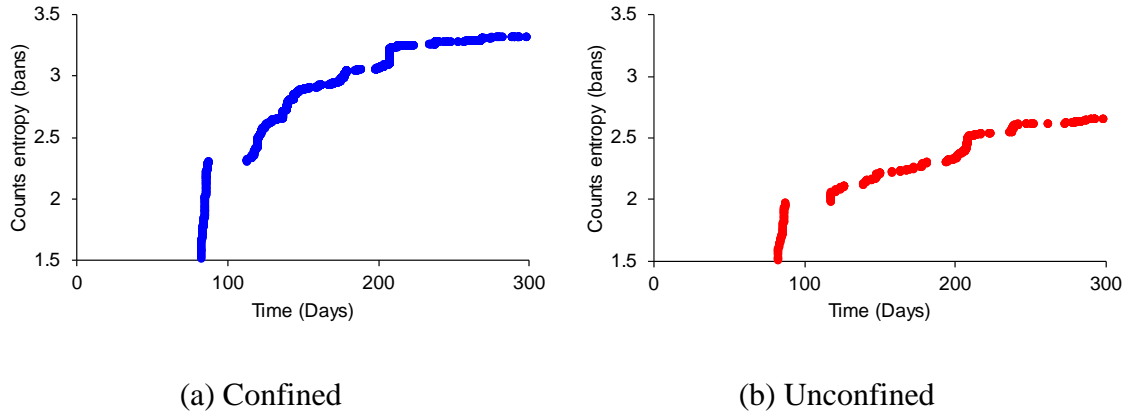


Figure 6.6 Counts entropy (CE) for medium-scaled specimens.

The second method utilized for calculating counts-entropy was by deriving empirical CDF and PDF of the counts, results are presented in Figure 6.7. The values for CE_CDF for both specimens were almost in the same range, contrary to CE values (Figure 6.6). Therefore, it can be concluded that CE_CDF did not depend on the number of hits contrary to CE.

The CE_CDF values for both specimens had an increasing trend and reached peak value, followed by a decreasing trend. In the unconfined specimen, the decreasing trend started earlier than for the confined specimen, although there was a slight increase at 242 days for the unconfined specimen.

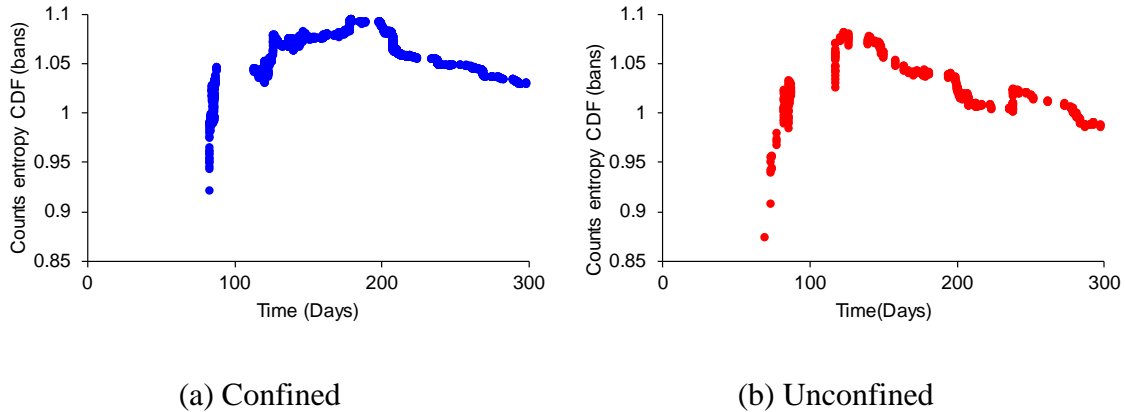


Figure 6.7 Counts entropy using CDF (CE_CDF) for medium-scale specimens.

The results of FFT entropies for the medium-scale specimens were averaged every 50 days and are presented in Figure 6.8. The average standard deviations are indicated in the figure. FFT entropies for both specimens were almost in the same range. In the confined specimen, the entropy decreased up to 200 days and then increased after that. However, in the unconfined specimen, the FFT entropy initially decreased and then increased up to 200 days. After 200 days, it decreased again, and in the end, it increased. The FFT entropy has an inverse relationship with the discrete voltage entropy.

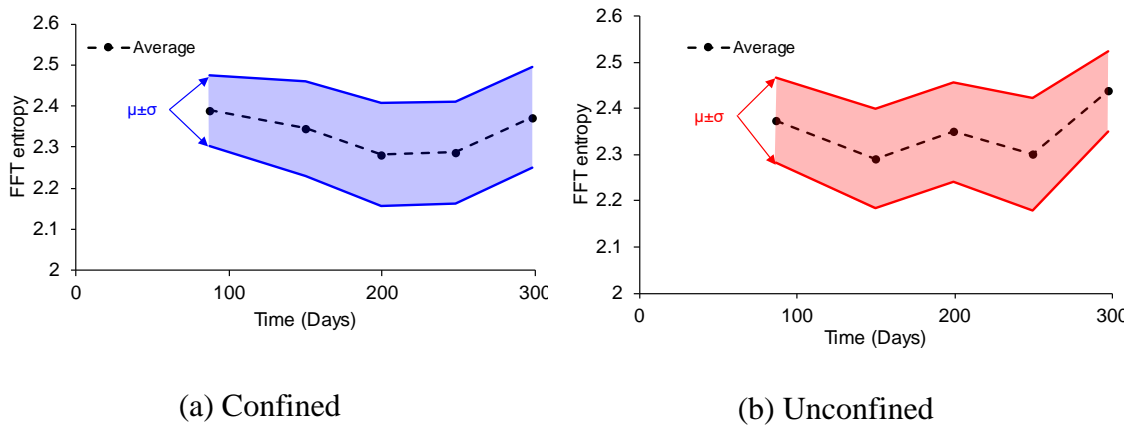


Figure 6.8 FFT entropy for medium-scale specimens

6.5.2 Voltage entropies for specimens with different scales

In this section, voltage entropies for three types of specimens: large-scale, medium-scale, and small-scale are discussed. The compressive load was applied on a cement paste prism (small-scale specimen) and stopped when the load reached 40% of expected ultimate capacity. The DVE was calculated for each signal by using a bin size of 0.0001 volts, results are presented in Figure 6.9a. The entropy ranged from 0.69 to 2.6.

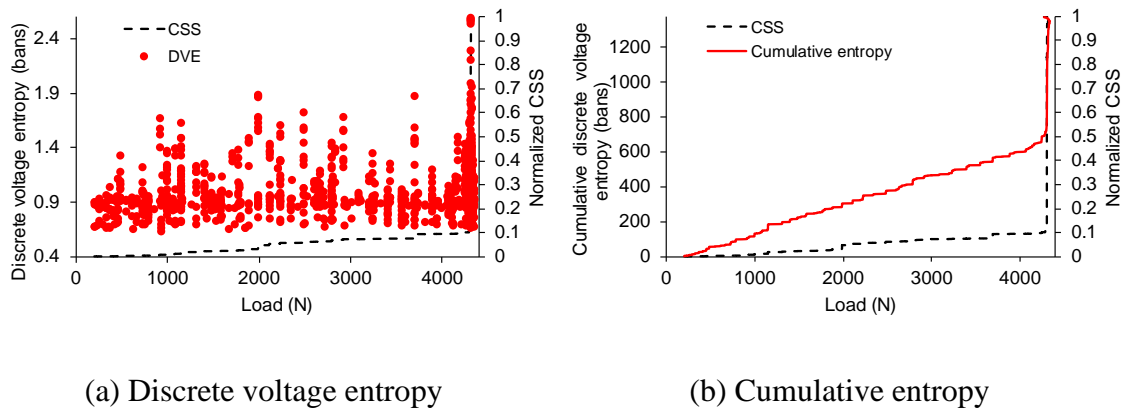


Figure 6.9 Discrete voltage entropy (DVE) and cumulative entropy for small-scale specimens

Cumulative voltage entropy and CSS are presented in Figure 6.9b. The trend of cumulative entropy was different from CSS for the small-scale specimen, despite a correlation between two parameters. The difference was more clear before the jump in CSS at the end of loading. The correlation coefficient between CSS and cumulative entropy is 0.907. The cumulative entropy increased with a constant rate and then experienced a sudden jump at the end of loading. The cumulative entropy showed two phases of cracking in the cement paste. The first phase is potentially related to microcrack formation and the second phase, at the end of loading, is more likely associated with unstable crack formation, propagation, and coalescence of existing cracks and formation of macrocracks [53].

Voltage entropies for the medium-scale and large-scale specimens are presented in Figure 6.10 and Figure 6.11, respectively. The DVE values for the medium-scale confined specimen ranged between 0.42 to 2.57, and the DVE values for the medium-scale unconfined specimen ranges were between 0.4 to 2.03. The correlation between CSS and cumulative entropy for the medium-scale and large-scale specimens is higher than the correlation for the small-scale specimen as seen in Figure 6.10 and Figure 6.11, which might be due to the differences in the loading and boundary conditions for the specimens under ASR versus compressive loading. The correlation coefficients between CSS and cumulative entropy for the medium-scale confined and unconfined specimen are 0.996, and the correlation coefficients for the large-scale confined and unconfined specimens are 0.999 and 0.995, respectively.

The entropy values for the large-scale confined specimen (Figure 6.11) ranged from 0.5 to 1.4, and the entropy for the large-scale unconfined specimen ranged from 0.46 to 1.5.

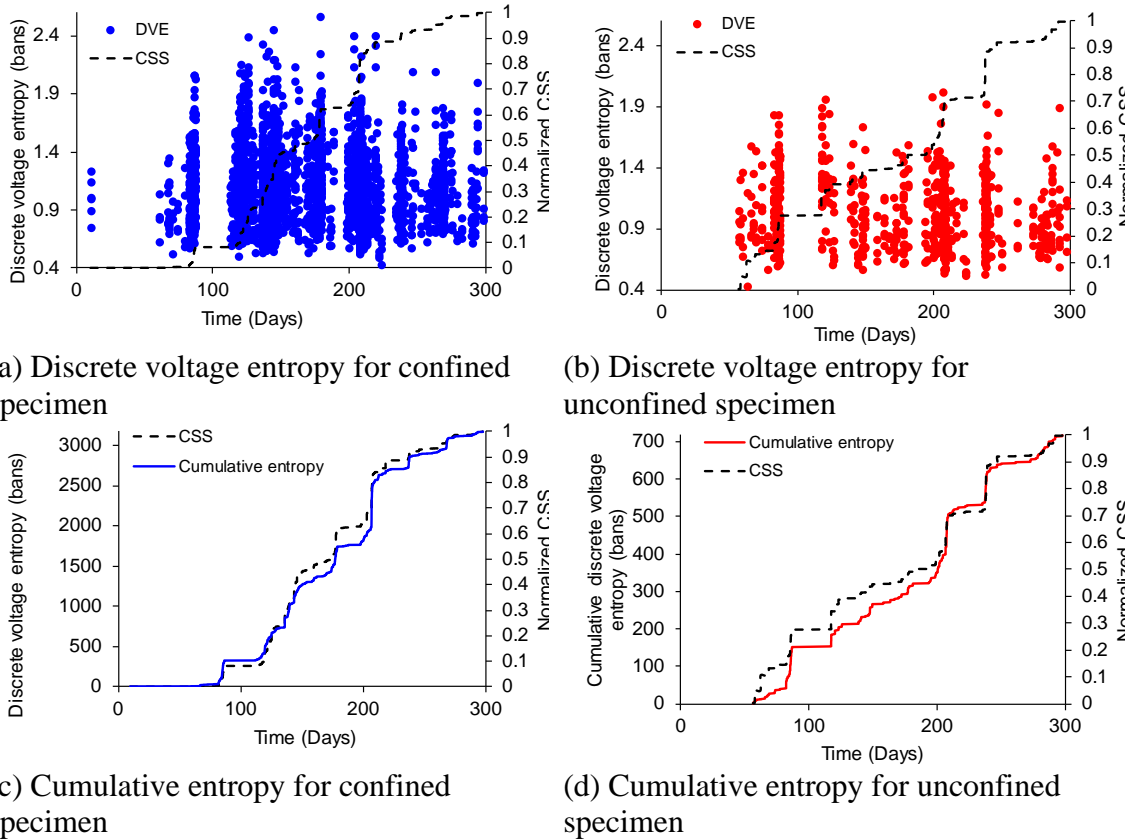
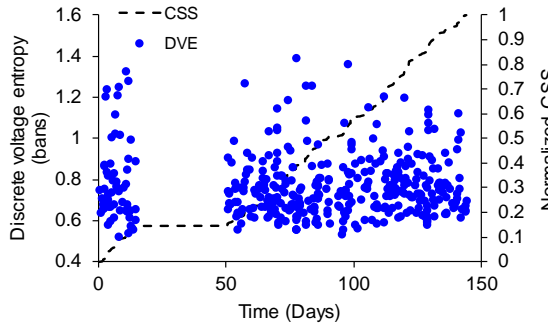
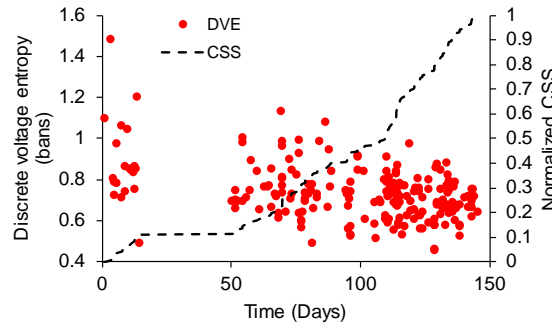


Figure 6.10 Discrete voltage entropy and cumulative entropy for medium-scale specimens

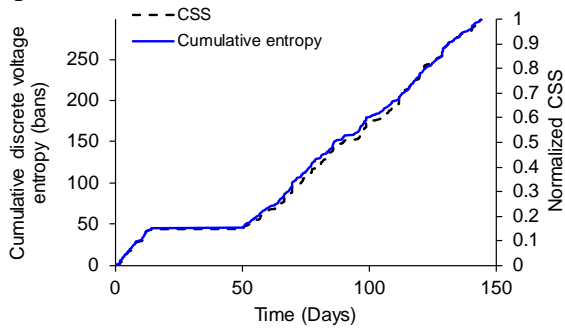
The distributions of voltage entropies for all specimens were estimated using nonparametric kernel distribution [54,55] and are presented in Figure 6.12a. In addition, the PDF of the signal strength is also illustrated in Figure 6.12b for comparison. The variation of voltage entropies for all specimens is much less than the variation of signal strength, indicating dimensional independence of entropy.



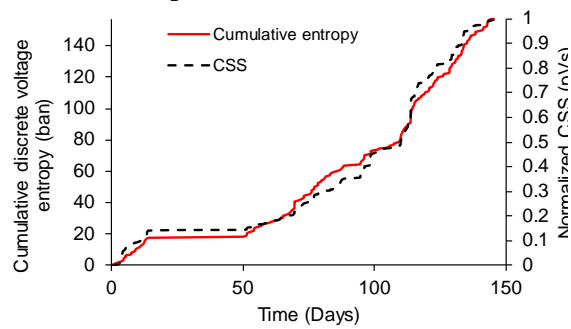
(a) Discrete voltage entropy for confined specimen



(b) Discrete voltage entropy for unconfined specimen

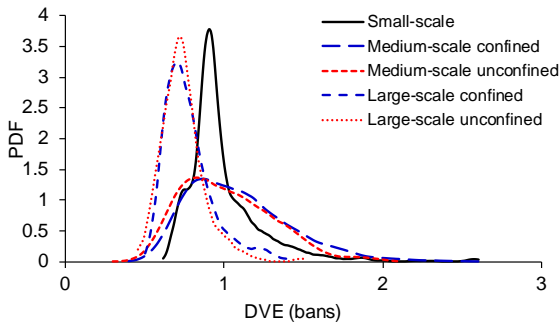


(c) Cumulative entropy for confined specimen

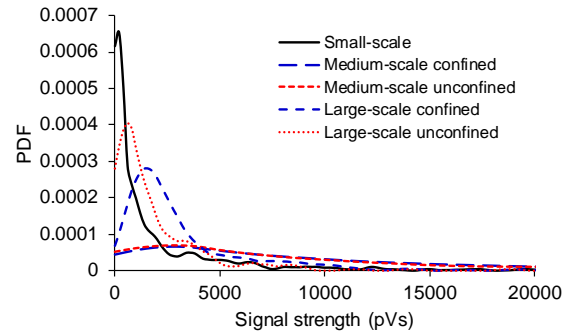


(d) Cumulative entropy for unconfined specimen

Figure 6.11 Discrete voltage entropy and cumulative entropy for large-scale specimens



(a) Distribution of voltage entropy



(b) Distribution of signal strength

Figure 6.12 Probability distribution functions of signal strength and entropy.

The ranges of voltage entropies for the specimens with different scales are similar. Therefore, Shannon entropy can be contemplated as a dimensionally independent parameter which may be used to compare AE data for specimens with different scales but similar boundary conditions and sensor type. The differences in the entropy trends between the specimens were due to different materials, boundary conditions, loading conditions, number of sensors, and sensor types. The specimens in this study were made of different materials. The small-scale specimen was a cement paste prism. The confined and unconfined medium-scale specimens were reinforced concrete and plain concrete, respectively. The large-scale specimens were also reinforced concrete. The cement paste material is more brittle and more homogeneous than concrete. Consequently, the cracking mechanism of the small-scale specimen was different from the medium-scale and large-scale specimens. The wave scattering in the small-scale specimen was expected to be less than other specimens since the small-scale specimen did not contain aggregate or reinforcement. The loading condition was also reflected in the inconsistencies between the entropy trends. The cement-paste was under compressive load, while no external loading was applied on the medium-scale and large-scale specimens. The medium-scale and large-scale specimens were exposed to ASR expansion and resulted internal strains. ASR-induced stresses were gradually formed in the specimens, while the external loading on the cement paste was applied within a much shorter time compared to the ASR process. The number of sensors and sensor coupling were other important factors which may influence the entropy trends. In the large-scale specimens, only three broadband sensors were used to monitor a large volume of concrete, while in the medium-scale specimens, a much denser sensor layout (ten sensors) was employed. Attachment of the sensors was another

potentially important factor. In the large-scale specimens, the sensors were embedded inside the specimens before casting. The concrete shrinkage may reduce the contact between the sensor and concrete. However, in the medium-scale specimens, the sensors were attached to the specimen surfaces using epoxy and constant pressure was applied to the sensors by the holders [42]. In the small-scale specimen, the sensors were also affixed on the surfaces, using epoxy and hot glue. The sensor types may also influence the entropy trends. The operating frequency range and sensitivity of the sensors utilized for three specimen types were different.

6.5.3 Intensity analysis and gradient of cumulative signal strength

Intensity analysis was conducted using the AE data from both medium-scale confined and unconfined specimens by employing the empirical parameters suggested in [41,47,56]. Parameter K in Eq. (6.2) is not applicable for $N \leq 50$; for $201 \leq N \leq 500$, $K = 0.85N$; and for $501 \leq N$, $K = N - 75$. Parameter J equals to zero for $N \leq 50$ and $J = 50$ for $51 \leq N$ [41]. The results of HI versus time are presented in Figure 6.13. As seen in the figures, the HI values for both specimens do not have a linear relationship with the CSS temporal evolution. The largest values for the HI do not necessarily indicate the largest jumps in the CSS curve.

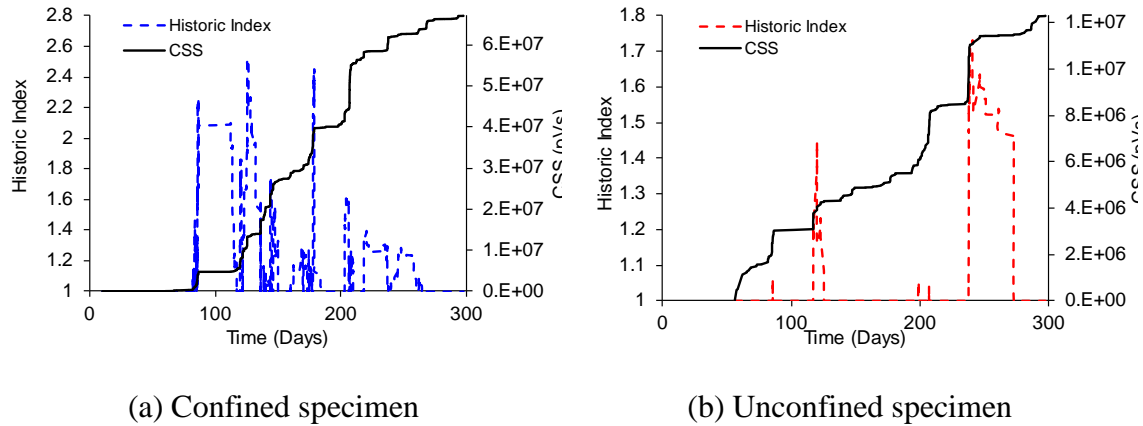


Figure 6.13 Historic index for medium-scale specimens

One reason for this characteristic of HI is the variation of temporal data distribution. The AE data distribution for the specimens in time was calculated by using kernel function [54,55] and is presented in Figure 6.14. The AE data distribution for the two specimens is different and also varies in terms of time. The parameters used for the historic index in this study are commonly used for damage evaluation of bridges under loading [34,41]. The AE distribution for loading differs from the AE distribution for the specimens affected by ASR. Therefore, the parameters should be adjusted based on the AE distribution for the specimens or structures affected by ASR.

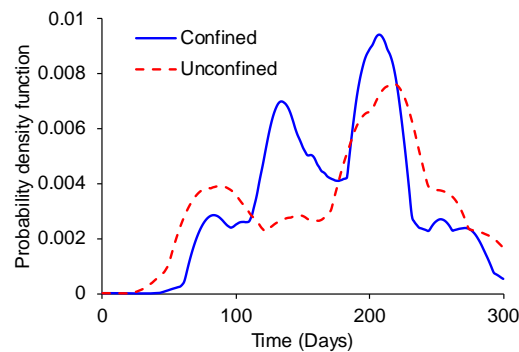


Figure 6.14 Probability density function of AE hits in time for the medium-scale specimens

The severities for the confined and unconfined specimens were calculated according to the intensity analysis parameters presented in [41] and illustrated in terms of HI in Figure 6.15. The HI values in the figure are the maximum HI up to the desired volumetric strains. The graph was separated based on the volumetric strains associated to the shown data point. The lines related to the volumetric strains of 0.3 % and 0.44 % are merged close to a data point related to the unconfined specimen. This shows that there is no significant variation of intensity parameters in the unconfined specimens within 0.3% to 0.44%. Generally, the variation of intensity analysis parameters for the confined specimen in terms of volumetric strain is larger than the variations for the unconfined specimen. This may be related to a larger stress concentration in the confined specimen compared to the unconfined specimen. The data for the confined specimens is mostly located on the top right corner of the graph, while the data for the confined specimens have a lower HI and severity and are located in the middle region of divided regions. The reason may be related to larger damage in the confined specimen than the unconfined specimen. In the confined specimen, the specimen experienced anisotropic expansion caused by the reinforcement. The anisotropic expansion caused the stress concentration in a specific direction, which may result into more damage in the confined specimen than the unconfined specimen.

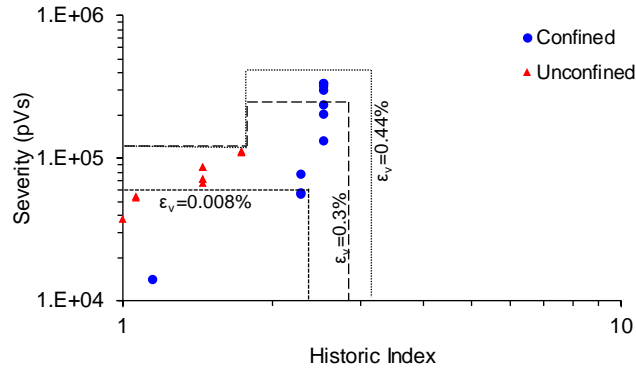


Figure 6.15 Intensity analysis graph for medium-scale specimens

The CSS gradients can present the evolution of CSS in terms of time. The CSS gradients for the medium-scale specimens are presented in Figure 6.16. In the confined specimen, the CSS gradient decreased after 200 days, while in the unconfined specimen, the gradient reduction started later after 250 days. The CSS gradient had an increasing trend, followed by a decreasing trend. The descending part might be due to the formation of large-scale cracks at the later stage of the ASR process. In the later stage of ASR, the macrocracks are formed by coalescence of existing microcracks or widening the existing cracks due to ASR pressure, while in the earlier stage microcracks are formed in an almost-intact concrete. The large-scale cracks may increase scattering and attenuation for the emitted signals and decrease the signal strengths. In addition, the signal strength of AE signals emitted by coalescence and widening of existing cracks may be less than the microcrack formation in the intact concrete.

From above observation it is concluded that ASR progress and associated damage can be roughly traced by observing the temporal evolution of CSS using the gradient.

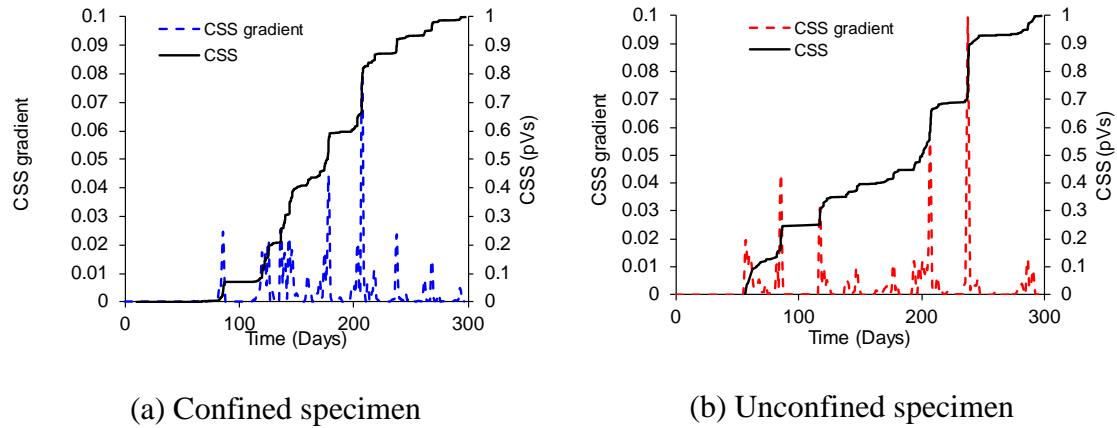


Figure 6.16 CSS gradients for medium-scale specimens

6.5.4 *b* value analysis

The Inc-*b* values and coefficients of determination of the amplitude distributions were calculated for the medium-scale specimens (confined and unconfined), and results are shown in Figure 6.17. The *b*-values did not have a clear correlation with the CSS in either specimen. However, coefficients of determination illustrated a clear correlation with the CSS. The coefficients of determination abruptly decreased at the jumps in the CSS curve. In the confined specimen, the sudden drops in coefficients of determination occurred at 174 and 207 days, when the large CSS jumps happened. In addition, in the unconfined specimen, a similar correlation was observed. For instance, the coefficients of determination decreased at 207 and 237 days. When severe damage happened in the specimens, a large amount of acoustic energy was expected to be released, which would generate AE data with strong signal strength and amplitude. The signals that generated a large amount of energy acted as outliers for the amplitude-logN distribution and made the distribution deviate more from linearity. This deviation resulted in a lower coefficient of determination.

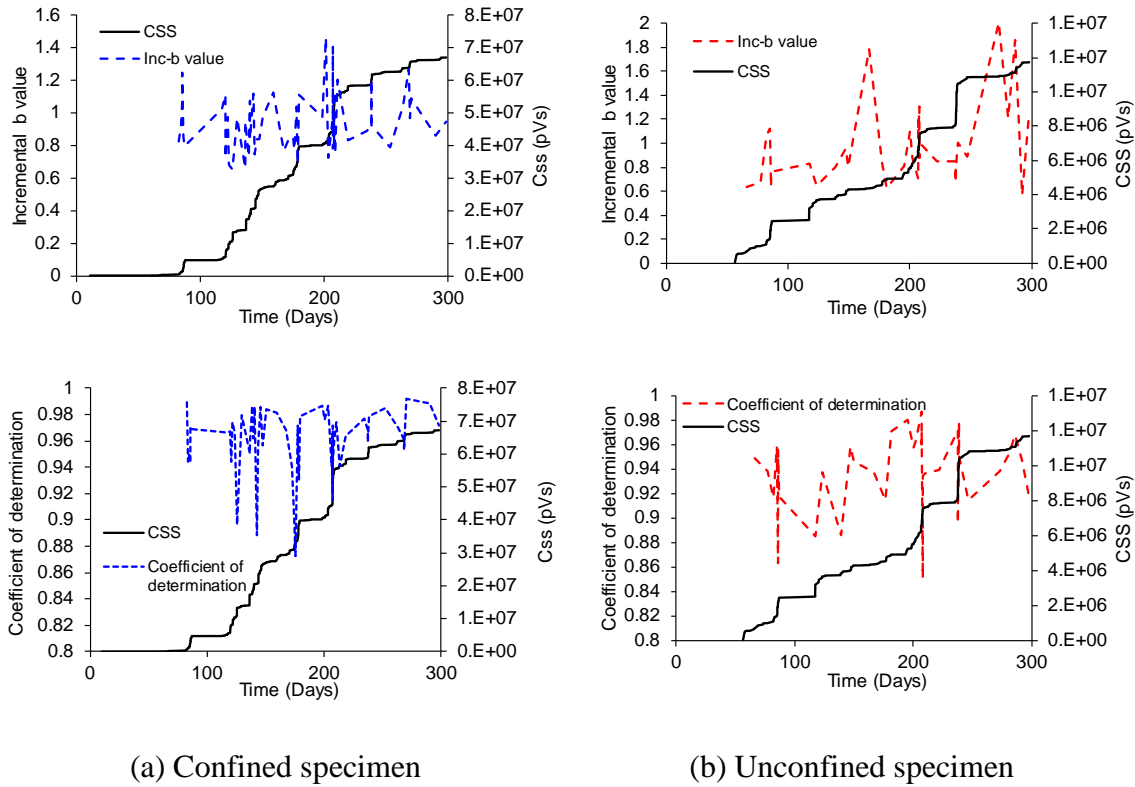


Figure 6.17 Incremental b values and coefficients of determination of amplitude distribution for medium-scale specimens

The Inc-Ib values were also calculated by deleting the data which were outside of average plus/minus standard deviation ($\mu \pm \sigma$) in each interval. The results are illustrated in Figure 6.18. The slight reductions in the Inc-Ib values were observed at the jumps in the CSS curve. The sudden reductions in the coefficients of determination were more apparent than the Inc-Ib values.

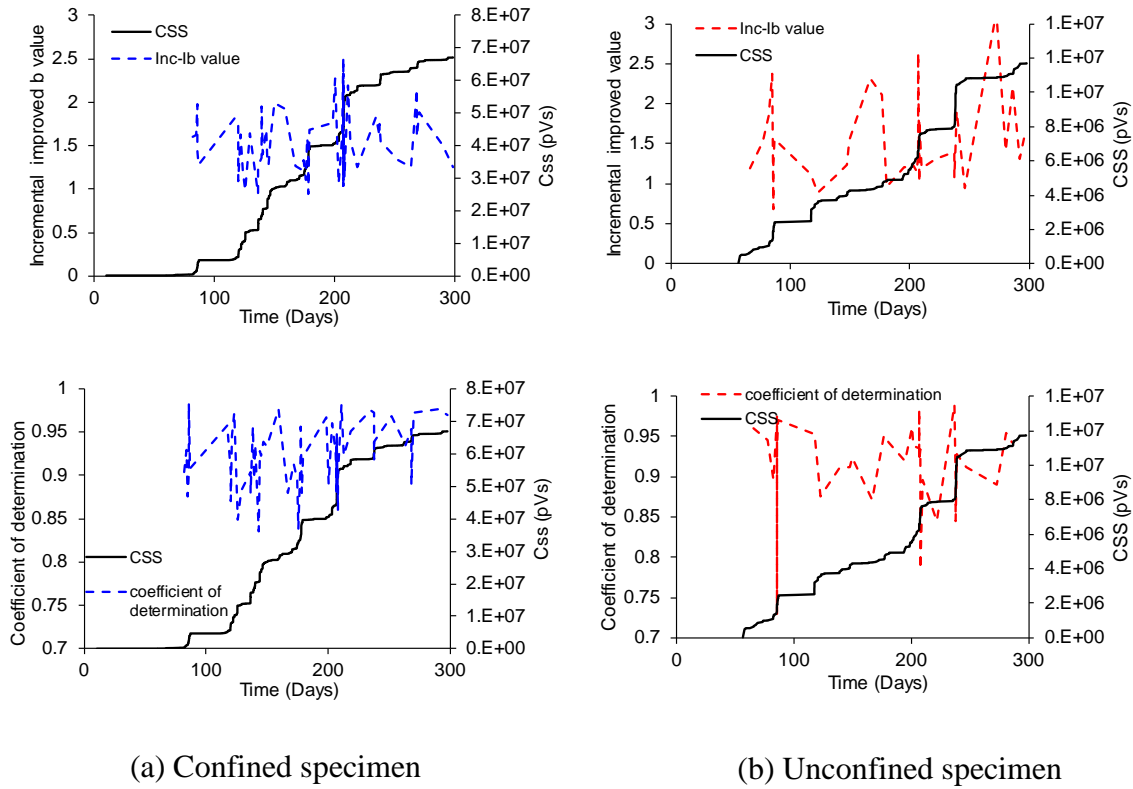


Figure 6.18 Incremental improved b values and coefficients of determination of amplitude distribution for medium-scale specimens

From the above observations, it is concluded that b-values did not show clear temporal trends for the specimens under ASR-induced expansion. On the other hand, the coefficient of determination can be used as an indicator to detect the occurrence of significant damage in lieu of the b-value.

6.6 Conclusion and summary

In this study, information entropy was calculated using different methods for the AE data recorded during the ASR process, and comparisons have been made between different methods. The efficacy of entropy for damage detection of concrete structures affected by ASR was evaluated in addition to studying the temporal evolution of entropies in the specimens. Moreover, an application of intensity, b-value analysis, and CSS gradient

was evaluated for the concrete specimens affected by ASR without external loading. The following are the conclusions drawn from the study:

- Although there were only minor variations in the discrete voltage entropy values, a trend was observed in the average values of entropies in terms of experiment time. The average entropy values initially showed an increasing trend, followed by a decreasing trend. The decreasing trend started earlier for the unconfined medium-scale specimen than the confined specimen. A similar trend was also observed in the global voltage entropy and counts-entropy using CDF for the medium-scale specimens. The entropy initially increased and then decreased or stayed constant at the later stages of ASR (after 200 days and 150 days for the confined and unconfined specimens). The information entropy quantifies the randomness of events. In this context, the randomness of events initially increased in the specimens and later decreased. At the earlier ASR stage, the microcracks randomly occurred inside the specimens. The random microcrack formation reflected in increasing entropy values. As the ASR progressed the macrocracks formed in the specific locations with a larger stress concentration and less strength. Therefore, the occurrence of macrocracks was less randomized. Therefore, the entropy had decreasing trend in this stage.
- The gradient of CSS can be used to identify the time of large acoustic energy release, which represents the damage accumulation. Moreover, the damage accumulation has a correlation with the ASR progression. Therefore, ASR progression can roughly be followed by observing the gradient of CSS.

- The variations of the b-values in terms of time for the confined and unconfined specimens were almost constant and the b-values did not show any obvious temporal trend. However, a correlation was observed between the coefficient of determination and the CSS curves. The coefficients of determination dropped at the CSS jumps, which indicates that the coefficients of determination were more sensitive to the damage formation than b-values. The coefficients of determination were dropped to the less than 92% at the large jumps in the CSS curves. The use of coefficients of determination is recommended for ASR damage identification in time.
- Comparing the discrete voltage entropies for the specimens with different scale and stress boundary conditions, it was observed that entropy ranges were not significantly changed by the specimen scale or boundary conditions. Therefore, this parameter may hold promise as an alternative for the comparison of damage conditions between different structures in terms of AE data.

The above conclusions are based on the initial research results. More research should be conducted regarding this subject.

6.7 Acknowledgments

This research was partially supported by the U.S Department of Energy-Nuclear Energy University Program (NEUP) under the contract DE-NE0008544 and the U.S. Department of Energy Office of Science, Office of Basic Energy Sciences and Office of Biological and Environmental Research under Award Number DE-SC-00012530.

6.8 References

1. Bach, F.; Thorsen, T.S.; Nielsen, M. Load-carrying capacity of structural members subjected to alkali-silica reactions. *Construction Building Materials* **1993**, *7*, 109-115.
2. Clark, L. *Critical review of the structural implications of the alkali silica reaction in concrete*; 0266-7045; Transportation and Road Research Laboratory: Crowthorne, UK, 1989.
3. Saouma, V.E.; Hariri-Ardebili, M.A. A proposed aging management program for alkali silica reactions in a nuclear power plant. *Nuclear Engineering Design* **2014**, *277*, 248-264.
4. Charlwood, R. In *Predicting the long term behaviour and service life of concrete dams*, Long Term Behaviour of Dams, LTBD09, Graz, Austria, 2009; Graz, Austria.
5. Takakura, T.; Ishikawa, T.; Mitsuki, S.; Matsumoto, N.; Takiguchi, K.; Masuda, Y.; Nishiguchi, I. In *Investigation on the expansion value of turbine generator foundation affected by alkali-silica reaction*, Proceedings of 18th International Conference on Structural Mechanics in Reactor Technology, 2005.
6. Barbosa, R.A.; Hansen, S.G.; Hansen, K.K.; Hoang, L.C.; Grelk, B. Influence of alkali-silica reaction and crack orientation on the uniaxial compressive strength of concrete cores from slab bridges. *Construction Building Materials* **2018**, *176*, 440-451.

7. Rajabipour, F.; Giannini, E.; Dunant, C.; Ideker, J.H.; Thomas, M.D. Alkali–silica reaction: Current understanding of the reaction mechanisms and the knowledge gaps. *Cement and Concrete Research* **2015**, *76*, 130-146.
8. Garcia-Diaz, E.; Riche, J.; Bulteel, D.; Vernet, C. Mechanism of damage for the alkali–silica reaction. *Cement Concrete Research* **2006**, *36*, 395-400.
9. Islam, M.S.; Ghafoori, N. A new approach to evaluate alkali-silica reactivity using loss in concrete stiffness. *Construction Building Materials* **2018**, *167*, 578-586.
10. Allard, A.; Bilodeau, S.; Pissot, F.; Fournier, B.; Bastien, J.; Bissonnette, B. Expansive behavior of thick concrete slabs affected by alkali-silica reaction (asr). *Construction Building Materials* **2018**, *171*, 421-436.
11. Sinno, N.; Shehata, M.H. Effect of sample geometry and aggregate type on expansion due to alkali-silica reaction. *Construction Building Materials* **2019**, *209*, 738-747.
12. Hayes, N.W.; Gui, Q.; Abd-Elssamd, A.; Le Pape, Y.; Giorla, A.B.; Le Pape, S.; Giannini, E.R.; Ma, Z.J. Monitoring alkali-silica reaction significance in nuclear concrete structural members. *Journal of Advanced Concrete Technology* **2018**, *16*, 179-190.
13. Thomas, M.D.A.; Folliard, K.J.; Fournier, B.; Rivard, P.; Drimalas, T.; Garber, S.I. *Methods for evaluating and treating asr-affected structures: Results of field application and demonstration projects–volume ii: Details of field applications and analysis*; US Department of Transportation, Federal Highway Administration: 2013.

14. Fournier, B.; Berube, M.-A.; Folliard, K.J.; Thomas, M. *Report on the diagnosis, prognosis, and mitigation of alkali-silica reaction (asr) in transportation structures*; 2010.
15. Teramoto, A.; Watanabe, M.; Murakami, R.; Ohkubo, T. Visualization of internal crack growth due to alkali-silica reaction using digital image correlation. *Construction Building Materials* **2018**, *190*, 851-860.
16. Rivard, P.; Saint-Pierre, F. Assessing alkali-silica reaction damage to concrete with non-destructive methods: From the lab to the field. *Construction Building Materials* **2009**, *23*, 902-909.
17. Giannini, E.R.; Folliard, K.J.; Zhu, J.; Bayrak, O.; Kreitman, K.; Webb, Z.; Hanson, B. *Non-destructive evaluation of in-service concrete structures affected by alkali-silica reaction (asr) or delayed ettringite formation (def)—final report, part i*; 2013.
18. Abdelrahman, M.; ElBatanouny, M.K.; Ziehl, P.; Fasl, J.; Larosche, C.J.; Fraczek, J. Classification of alkali-silica reaction damage using acoustic emission: A proof-of-concept study. *Construction Building Materials* **2015**, *95*, 406-413.
19. Lokajiček, T.; Přikryl, R.; Šachlová, Š.; Kuchařová, A. Acoustic emission monitoring of crack formation during alkali silica reactivity accelerated mortar bar test. *Engineering geology* **2017**, *220*, 175-182.
20. Farnam, Y.; Geiker, M.R.; Bentz, D.; Weiss, J. Acoustic emission waveform characterization of crack origin and mode in fractured and asr damaged concrete. *Cement and Concrete Composites* **2015**, *60*, 135-145.
21. Weise, F.; Voland, K.; Pirskawetz, S.; Meinel, D. In *Innovative measurement techniques for characterising internal damage processes in concrete due to asr*,

- Proceedings of the International Conference on Alkali Aggregate Reaction (ICAAR), University of Texas, Austin, TX, USA, 2012; pp 20-25.
22. Chai, M.; Zhang, Z.; Duan, Q. A new qualitative acoustic emission parameter based on shannon's entropy for damage monitoring. *Mechanical Systems Signal Processing* **2018**, *100*, 617-629.
 23. Kahirdeh, A.; Sauerbrunn, C.; Yun, H.; Modarres, M. A parametric approach to acoustic entropy estimation for assessment of fatigue damage. *International Journal of Fatigue* **2017**, *100*, 229-237.
 24. Unnthorsson, R.; Runarsson, T.P.; Jonsson, M.T. Ae entropy for the condition monitoring of cfrp subjected to cyclic fatigue. *Journal of Acoustic Emission* **2008**, *26*, 262-269.
 25. Amiri, M.; Modarres, M.; Droguett, E.L. In *Ae entropy for detection of fatigue crack initiation and growth*, 2015 IEEE Conference on Prognostics and Health Management (PHM), 2015; IEEE: pp 1-8.
 26. Kahirdeh, A.; Yun, H.; Modarres, M. Degradation entropy: An acoustic emission based approach to structural health assessment. *Structural Health Monitoring* **2017**.
 27. Amiri, M.; Modarres, M. An entropy-based damage characterization. *Entropy* **2014**, *16*, 6434-6463.
 28. Kahirdeh, A.; Khonsari, M. Acoustic entropy of the materials in the course of degradation. *Entropy* **2016**, *18*, 280.
 29. Zhang, X.; Feng, N.; Wang, Y.; Shen, Y. Acoustic emission detection of rail defect based on wavelet transform and shannon entropy. *Journal of Sound Vibration* **2015**, *339*, 419-432.

30. Whaley, P. A mathematical model for internal friction and local fatigue damage based on populations of yielding microelements. *Journal of vibration, acoustics, stress, reliability in design* **1987**, *109*, 201-206.
31. Basaran, C.; Yan, C.-Y. A thermodynamic framework for damage mechanics of solder joints. *Journal of Electronic Packaging* **1998**, *120*, 379-384.
32. Imanian, A.; Modarres, M. Development of a generalized entropic framework for damage assessment. In *Fracture, fatigue, failure and damage evolution*, Springer: 2016; Vol. 8, pp 73-81.
33. Liakat, M.; Khonsari, M. On the anelasticity and fatigue fracture entropy in high-cycle metal fatigue. *Materials design* **2015**, *82*, 18-27.
34. Noorsuhada, M. An overview on fatigue damage assessment of reinforced concrete structures with the aid of acoustic emission technique. *Construction Building Materials* **2016**, *112*, 424-439.
35. Rao, M.; Lakshmi, K.P. Analysis of b-value and improved b-value of acoustic emissions accompanying rock fracture. *Current science* **2005**, 1577-1582.
36. Colombo, I.S.; Main, I.; Forde, M. Assessing damage of reinforced concrete beam using “b-value” analysis of acoustic emission signals. *Journal of Materials in Civil Engineering* **2003**, *15*, 280-286.
37. Jung, D.Y.; Mizutani, Y.; Todoroki, A.; Suzuki, Y. Frequency dependence of the b-value used for acoustic emission analysis of glass fiber reinforced plastics. *Open Journal of Composite Materials* **2017**, *7*, 117.

38. Lamonaca, F.; Carrozzini, A.; Grimaldi, D.; Olivito, R.S. Improved accuracy of damage index evaluation in concrete structures by simultaneous hardware triggering. *Metrology Measurement Systems* **2014**, *21*, 341-350.
39. Abdelrahman, M.; ElBatanouny, M.K.; Ziehl, P.H. Acoustic emission based damage assessment method for prestressed concrete structures: Modified index of damage. *Engineering Structures* **2014**, *60*, 258-264.
40. Sagasta, F.; Zitto, M.E.; Piotrkowski, R.; Benavent-Climent, A.; Suarez, E.; Gallego, A. Acoustic emission energy b-value for local damage evaluation in reinforced concrete structures subjected to seismic loadings. *Mechanical Systems Signal Processing* **2018**, *102*, 262-277.
41. Nair, A.; Cai, C. Acoustic emission monitoring of bridges: Review and case studies. *Engineering Structures* **2010**, *32*, 1704-1714.
42. Soltangharai, V.; Anay, R.; Hayes, N.; Assi, L.; Le Pape, Y.; Ma, Z.; Ziehl, P. Damage mechanism evaluation of large-scale concrete structures affected by alkali-silica reaction using acoustic emission. *Applied Sciences* **2018**, *8*, 2148.
43. Kahirdeh, A. Energy dissipation and entropy generation during the fatigue degradation: Application to health monitoring of composites. Louisiana State University, 2014.
44. Sauerbrunn, C.M. Evaluation of information entropy from acoustic emission waveforms as a fatigue damage metric for al7075-t6. 2016.
45. Kahirdeh, A.; Sauerbrunn, C.; Modarres, M. In *Acoustic emission entropy as a measure of damage in materials*, AIP Conference Proceedings, 2016; AIP Publishing: p 060007.

46. Golaski, L.; Gebiski, P.; Ono, K. Diagnostics of reinforced concrete bridges by acoustic emission. *Journal of acoustic emission* **2002**, *20*, 83-89.
47. Fowler, T.J.; Blessing, J.A.; Conlisk, P.J.; Swanson, T.L. The monpac system. *Journal of acoustic emission* **1989**, *8*, 1-8.
48. Di Benedetti, M.; Nanni, A. Acoustic emission intensity analysis for in situ evaluation of reinforced concrete slabs. *Journal of materials in civil engineering* **2013**, *26*, 6-13.
49. Abouhussien, A.A.; Hassan, A.A. The use of acoustic emission intensity analysis for the assessment of cover crack growth in corroded concrete structures. *Journal of Nondestructive Evaluation* **2016**, *35*, 52.
50. Vélez, W.; Matta, F.; Ziehl, P. In *Acoustic emission intensity analysis of corrosion in prestressed concrete piles*, AIP Conference Proceedings, 2014; AIP: pp 888-894.
51. Shiotani, T. Evaluation of progressive failure using ae sources and improved b-value on slope model tests. *Progress in Acoustic Emission VII* **1994**, 529-534.
52. Shiotani, T. Application of the ae improved b-value to quantitative evaluation of fracture process in concrete-materials. *Journal of acoustic emission* **2001**, *19*, 118-133.
53. Anay, R.; Soltangharaei, V.; Assi, L.; DeVol, T.; Ziehl, P. Identification of damage mechanisms in cement paste based on acoustic emission. *Construction Building Materials* **2018**, *164*, 286-296.
54. Wand, M.P.; Jones, M.C. *Kernel smoothing*. Chapman and Hall/CRC: 1994.
55. Epanechnikov, V.A. Non-parametric estimation of a multivariate probability density. *Theory of Probability Its Applications* **1969**, *14*, 153-158.

56. Chotickai, P. Acoustic emission monitoring of prestressed bridge girders with premature concrete deterioration. University of Texas at Austin, 2001.

Chapter 7

Summary and Conclusion

7.1 Summary

Alkali silica reaction (ASR) is one of the primary causes of degradation in concrete structures, which endangers their integrity and serviceability. Conventional methods for monitoring and tracing ASR-induced damage are subjective, and in some cases, destructive and inefficient. Acoustic emission (AE) may be an alternative for assessing the condition of structures affected by ASR. AE piezoelectric sensors are very sensitive and capable of capturing small-scale defects. In addition, AE is a passive method, and therefore, monitoring of structures using AE is feasible without halting structural serviceability. AE is a nondestructive method, which is preferable for monitoring the structural health monitoring of sensitive structures. In addition, wireless-based AE technology is being developed. Source localization is possible using this method with an appropriate sensor layout. AE can be employed for monitoring the health of structures with limited access. These advantages make AE favorable for condition assessments of structures experiencing ASR-induced damage. However, several challenges and scientific gaps exist in a path toward developing an AE-based condition assessment for ASR induced damage, some of which are covered in this dissertation. One of the scientific gaps is the effect of boundary conditions on distribution of damage caused by ASR and the reflection of anisotropic damage in AE data. Another gap is parametric AE analysis to investigate the temporal evolution of ASR-induced damage. Therefore, four different studies are defined to approach the primary goal.

In the first study, the source of the AE signal signatures in a cement prism under compressive loading was investigated by relating AE data from the compression test to a more controlled test in terms of crack formation (notched four-point bending). Energy-

frequency based features were derived from AE signals emitted from both the compression test and the bending test and the number of features was reduced by using principal component analysis (PCA). The AE data with principal component (PC) features from the compression test were clustered using an agglomerative clustering method, and the data were labeled. A neural network was trained using the AE data from the compression test and corresponding labels. The trained network was employed to cluster an unlabeled AE data from the bending test. The AE data from the bending test were clustered using the trained network and localized. Then, the signal signatures were identified based on the occurrence and locations of the clustered events and signal feature analysis.

In the second study, three large-scale, reinforced concrete blocks were cast. Two were expanded due to ASR and one was a control specimen. The specimens had dimensions of 3.5 m × 3.0 m × 1.0 m (136 inch × 116 inch × 40 inch). All specimens had reinforcements at the top and bottom and did not have any transverse reinforcement. One of the reactive specimens was confined in-plane by a rigid steel frame, and other was partially restrained in-plane by the reinforcement. AE broadband sensors were embedded inside the specimens before casting. The AE data were collected during the ASR process. The effect of in-plane confinement on the damage distribution in the large-scale concrete structures affected by ASR was investigated through AE and strain data. AE data were clustered using unsupervised pattern recognition. Acoustic energies were investigated in terms of clusters and sensor locations.

In the third study, three medium-scale concrete blocks with dimensions of 305 mm × 305 mm × 1120 mm were cast at the University of Alabama and retained in a

chamber with a high temperature and high humidity at the University of South Carolina. Two specimens had reactive aggregates (reactive specimens), and one did not have any reactive aggregates (control specimen). One of the reactive specimens had steel reinforcement along two dimensions (X and Z) (referred to as the confined specimen) and the other reactive specimen did not have steel reinforcement (namely the unconfined specimen). The control specimen also had no reinforcements. Ten broadband AE sensors were affixed on the surfaces of the reactive specimens, which provide feasibility to elaborately study the ASR process and damage distribution caused by the steel reinforcement. ASR damage contours were derived using AE data, and the temporal evolution of the AE data was investigated in terms of signal frequency. Data-driven methods and AE data were employed for understanding the damage distribution in the structures affected by ASR expansion.

In the fourth study, the information entropies of AE data from the ASR test, using different methods, were calculated and compared. The temporal evolution of the different information entropies was investigated for structures affected by ASR. Conventional parametric AE features such as signal strength and amplitude are highly dependent on the specimen scale, sensor type, and sensor layout. Therefore, a need for dimensionally independent parameters to evaluate damage in structures is incontrovertible. Information entropy or Shannon entropy is an alternative to this goal, which has been examined for cementitious material, particularly concrete structures under ASR-induced damage in this dissertation. In addition, the efficacy of intensity analysis and b-value analysis for specimens affected by ASR was also investigated.

7.2 Conclusion of each study

7.2.1 Evaluation of damage propagation in cement paste using pattern recognition

In this study, a combination of unsupervised and supervised pattern recognition was employed to relate the crack formation mechanisms of a cement paste prism under a compression test to a more controlled test, i.e., notched four-point bending. The ray-tracing algorithm was utilized for the source location of AE events. The following conclusions may be drawn:

- The cement paste specimen showed brittle behavior during the four-point bending test. The post-peak regime in the load-CMOD curve is narrow. The fracture energy of the cement paste is very low compared to the absorbed energy (18.6% of the total, energy). Moreover, a correlation between CSS and the absorbed energy rate can be observed. The CSS and absorbed energy rate showed a large jump at the end of loading in the post-peak regime due to the propagation of an unstable crack.
- The cracking mechanisms caused by the compressive load were governed by tensile mode due to the large aspect ratio of the specimens. It is confirmed by the results from the moment tensor analysis and observation of the failure mechanism in the specimens under compressive loading.
- The cluster with the highest frequency components (Cluster 3), were initiated at the beginning of the four-point bending. The potential mechanism assigned to the cluster is microcrack initiation. The cluster with the lower frequency components in the FFT spectrum occurred when cracks were already formed in the specimen, and near the end of loading.

Therefore, this cluster may be assigned to propagation and coalescence of the cracks.

- There is a correlation between frequency and non-frequency dependent features of AE signals. The AE signals with the higher frequency components have larger signal strength and lower rise angles compared to the AE signals with the lower frequency components. This is also supported by observing the CSS curve. The jumps in the cumulative signal strength are mostly due to the signals with higher frequency components (Cluster 2 and Cluster 3).
- The events which were located using the ray-tracing algorithm approximately match the observed crack path. This result is achieved by employing the capability of the algorithm to consider diverse elastic wave velocities in different emission directions. The observed error is caused by scattering of the waves due to damage concentration in the midspan.

7.2.2 Damage Mechanism Evaluation of Large-Scale Concrete Structures Affected by Alkali-Silica Reaction Using Acoustic Emission

Acoustic emission was utilized for monitoring the activities caused by ASR in large-scale reinforced concrete specimens. The specimens resemble common nuclear power plant containments with no shear reinforcement. An agglomerative hierarchical algorithm was used to classify the AE data based on the energy-frequency dependent features in order to study and identify the damage mechanisms in the specimens with different stress boundary conditions. The conclusions of this study are summarized as follows:

- A significant portion of the AE data (in terms of cumulative signal strength) in the confined specimen was recorded by sensor 3, which was located at mid-thickness. However, the portion of cumulative signal strength for the corresponding sensor at mid-thickness of the unconfined specimen was less in comparison to the other two sensors in that specimen. This agrees with expectations, as the confined specimen exhibited increased out-of-plane expansion in comparison to the unconfined specimen, meaning that the crack distribution is expected to be more concentrated near mid-thickness of the confined specimen than near the reinforcement layers.
- The frequency contents of signals in the confined and unconfined specimens evolved from low to high frequency with the age of the concrete, although this evolution started later in the confined specimen than the unconfined specimen. Since the high-frequency AE signals have been associated with cracking in the aggregates [1], different crack mechanisms in aggregates for the confined and unconfined specimens are expectable. However, different and contradictory ASR cracking hypotheses have been proposed by other researchers [2-9].
- There is a coincident point observed in the strain curves and the CSS of Cluster-3 in the confined specimen and Cluster-6 in the unconfined specimen. The CSS rate in terms of concrete age increases at around 150 days when the strain rate is decreasing. The point where the curvature of strain curve changes from positive to negative is referred to as the

inflection point of strain curve. The inflection point location, in terms of concrete age, depends on the kinetics of the ASR reaction and diffusion process. Determining the inflection point, latency and characteristic time are experimentally estimated and are two important modeling parameters. According to the results of AE data and clustering, the inflection point location, in terms of concrete age, could be estimated from a variation in CSS rate change of clustered AE data.

- Monitoring of a structural system with acoustic emission can provide useful information regarding condition-based maintenance and/or retrofit. For example, one potential time of action for treating affected structures is around the inflection point in the volumetric strain curve, which can be approximated through acoustic emission data. This point coincided with the observation of the first visible surface cracks. After identifying the time of action, treatment methods may be implemented to mitigate the effects of ASR. Injection of a lithium solution is a chemical alternative to mitigate ASR provided that enough solution penetration in the structure can be achieved. Another method is to remove moisture through coatings and sealers such as silane sealers and bituminous or elastomeric coatings. After conducting these methods, structures should be monitored for enough time to evaluate the efficiency of the method.

7.2.3 Temporal Evaluation of ASR Damage in Concrete Specimens with a Data-driven Approach

The effects of confinement provided by longitudinal and transverse reinforcement was studied through data-driven methods. Unsupervised pattern recognition in combination with source location and statistical analysis were utilized. Three specimens were cast and exposed to high temperature and humidity for almost 300 days. Two specimens contained a reactive coarse aggregate, and the control specimen contained only nonreactive aggregates. One of the reactive specimens had confinement provided through steel reinforcement along the X and Z coordinates. The other reactive specimen and the nonreactive control specimen did not have any steel reinforcement. The ASR expansion was regularly measured with a DEMEC gauge. In addition, the crack widths on the top surface of the specimens were measured. The main conclusions of the study are summarized as follows:

- The effect of the boundary conditions on ASR damage distribution is clearly reflected in the AE data. Significantly more AE activity was detected in the confined specimen than in the unconfined specimen, with AE events concentrated in the mid-width region of the confined specimen. The events exhibited a relatively sharp distribution. The distribution of AE events for the unconfined specimen across the specimen width was more uniform. These observations in AE data correlate with anisotropic expansion in the confined specimen.
- Damage from ASR in the confined specimen initiated earlier and was manifested in higher severity than the damage in the unconfined

specimen. This can be observed from the AE data, expansion strains, and visible crack formation. The cumulative signal strength rate for the confined specimen increased abruptly at 115 days (early stage of ASR). This behavior was not observed for the unconfined specimen. The volumetric strains for the confined specimen were greater than for the unconfined specimen up to 260 days. This difference between the volumetric strains was mainly due to very large strains in the confined specimen in the Y direction. Furthermore, the number of cracks in the confined specimen was greater than the unconfined specimen at 146 days (start of the crack measurement), and maximum crack widths on the top surface of the confined specimen were larger than the crack widths of the unconfined specimen.

7.2.4 Investigation of Temporal Evolution of AE Data for Concrete Specimens Affected by ASR Using Information entropy, b-value, Regression analysis, and Gradient of Cumulative Signal Strength

In this study, information entropy was calculated using different methods for the AE data recorded during the ASR process, and comparisons have been made between different methods. The efficacy of entropy for damage detection of concrete structures affected by ASR was evaluated in addition to studying the temporal evolution of entropies in the specimens. Moreover, an application of intensity, b-value analysis, and CSS gradient was evaluated for the concrete specimens affected by ASR without external loading. The following are the conclusions drawn from the study:

- Although there were only minor variations in the discrete voltage entropy values, a trend was observed in the average values of entropies in terms of experiment time. The average entropy values initially showed an increasing trend, followed by a decreasing trend. The decreasing trend started earlier for the unconfined medium-scale specimen than the confined specimen. A similar trend was also observed in the global voltage entropy and counts-entropy using CDF for the medium-scale specimens. The entropy initially increased and then decreased or stayed constant at the later stages of ASR (after 200 days and 150 days for the confined and unconfined specimens). The information entropy quantifies the randomness of events. In this context, the randomness of events initially increased in the specimens and later decreased. At the earlier ASR stage, the microcracks randomly occurred inside the specimens. The random microcrack formation reflected in increasing entropy values. As the ASR progressed the macrocracks formed in the specific locations with a larger stress concentration and less strength. Therefore, the occurrence of macrocracks was less randomized. Therefore, the entropy had decreasing trend in this stage.
- The gradient of CSS can be used to identify the time of large acoustic energy release, which represents the damage accumulation. Moreover, the damage accumulation has a correlation with the ASR progression. Therefore, ASR progression can roughly be followed by observing the gradient of CSS.

- The variations of the b-values in terms of time for the confined and unconfined specimens were almost constant and the b-values did not show any obvious temporal trend. However, a correlation was observed between the regression coefficients and the CSS curves. The regression coefficients dropped at the CSS jumps, which indicates that the regression coefficients were more sensitive to the damage formation than b-values. The regression coefficients were dropped to the less than 92% at the large jumps in the CSS curves. The use of regression coefficients is recommended for ASR damage identification in time.
- Comparing the discrete voltage entropies for the specimens with different scale and stress boundary conditions, it was observed that entropy ranges were not significantly changed by the specimen scale or boundary conditions. Therefore, this parameter may hold promise as an alternative for the comparison of damage conditions between different structures in terms of AE data.

The above conclusions are based on the initial research results. More research should be conducted regarding this subject.

7.3 Recommendation and future work

The main goal of this study is employing AE for condition assessment of structures affected by ASR. Some scientific gaps were addressed in this dissertation; however, more research should be conducted before starting to implement AE in the field.

In this dissertation, the temporal damage evolution of specimens affected by ASR was investigated using AE data. Different parameters such as signal frequency, cumulative signal strength, and information entropy have been utilized to study ASR-induced damage of specimens in terms of time. A trend was observed in different AE parameters, and some hypotheses were proposed to justify that. However, more experiments should be conducted to correlate the visual damage quantification to the temporal pattern observed in the AE data. This can be accomplished by using more reactive specimens monitored by AE and simultaneously taking a large number of samples for a Scanning Electron Microscope and petrography analyses during the ASR process.

In addition to the importance of microscopic evolution of specimens affected by ASR, macroscopic behavior and the global capacity of structures are significant as well. This can be accomplished by running more tests to study the specimen capacities such as shear and flexural strength in different ASR stages. An advanced finite element model can also be helpful to achieve this goal in addition to the experimental tests. After that, the AE data is compared to the temporal evolution of structural capacity, and a potential correlation between the AE data and structural capacity can be derived.

ASR damage depends directly on humidity and temperature. The specimens evaluated in the dissertation were exposed to high temperatures and humidity to accelerate the aging process. In reality, structures in the field are not exposed to as harsh conditions as the specimens were under laboratory conditions. Therefore, the effect of temperature and humidity on the temporal damage condition of structures affected by

ASR should be investigated. In addition, the effect of the temperature and humidity fluctuations on AE data should also be studied.

Structures in the field are exposed to environmental weather conditions, which change frequently. Environmental conditions can affect or contaminate AE data. For instance, precipitation and wind can generate AE data, which may increase challenges and difficulty associated with data analysis. More research should be conducted to identify the difference between signal signatures emitted from defect formation and precipitation or environmental noise sources. Machine learning or deep learning algorithms in combination with signal processing can be helpful to achieve this goal.

Damage localization is one of the advantages of the AE method. However, this is fulfilled only if an appropriate sensor layout and sensor number are employed. In real structures, this is usually not feasible due to the large scales of the structures and the limitation of using a large number of sensors. Therefore, more research should be conducted to develop new source localization algorithms with minimal sensor requirement and higher precision. This might be accomplished by using data-driven methods such as deep learning or machine learning methods.

7.4 References

1. Farnam, Y.; Geiker, M.R.; Bentz, D.; Weiss, J. Acoustic emission waveform characterization of crack origin and mode in fractured and asr damaged concrete. *Cement and Concrete Composites* **2015**, *60*, 135-145.
2. Hanson, W. In *Studies relating to the mechanism by which the alkali-aggregate reaction produces expansion in concrete*, Journal Proceedings, 1944; pp 213-228.

3. Escalante-Garcia, J.; Sharp, J. The microstructure and mechanical properties of blended cements hydrated at various temperatures. *Cement and Concrete Research* **2001**, *31*, 695-702.
4. Pan, J.; Feng, Y.; Wang, J.; Sun, Q.; Zhang, C.; Owen, D. Modeling of alkali-silica reaction in concrete: A review. *Frontiers of Structural Civil Engineering* **2012**, *6*, 1-18.
5. McGowan, J. Studies in cement-aggregate reaction xx, the correlation between crack development and expansion of mortar. *Australian Journal of Applied Science* **1952**, *3*, 228-232.
6. Bažant, Z.P.; Steffens, A. Mathematical model for kinetics of alkali-silica reaction in concrete. *Cement Concrete Research* **2000**, *30*, 419-428.
7. Dron, R.; Brivot, F. Thermodynamic and kinetic approach to the alkali-silica reaction. Part 1: Concepts. *Cement Concrete Research* **1992**, *22*, 941-948.
8. Ponce, J.; Batic, O.R. Different manifestations of the alkali-silica reaction in concrete according to the reaction kinetics of the reactive aggregate. *Cement Concrete Research* **2006**, *36*, 1148-1156.
9. Ichikawa, T.; Miura, M. Modified model of alkali-silica reaction. *Cement Concrete research* **2007**, *37*, 1291-1297.

Appendix A

Copyright Permission

The paper entitled “Damage Mechanism Evaluation of Large-Scale Concrete Structures Affected by Alkali-Silica Using Acoustic Emission” is open access and free to share and copy and redistribute in any medium or format as mentioned in the following statement (link) at the end of the paper.



© 2018 by the authors. Licensee MDPI, Basel, Switzerland. This article is an open access article distributed under the terms and conditions of the Creative Commons Attribution (CC BY) license (<http://creativecommons.org/licenses/by/4.0/>).

The paper entitled “Temporal Evaluation of ASR Cracking in Concrete Specimens Using Acoustic Emission”:

A full credit line must be added to the material being reprinted. Please note in your credit that you are using the pre-production version of your paper, with permission from ASCE, and include the DOI (noted below). For reuse in non-ASCE publications, add the words "With permission from ASCE" to your source citation. For Intranet posting, add the following additional notice: "This material may be downloaded for personal use only. Any other use requires prior permission of the American Society of Civil Engineers. This material may be found at [DOI: 10.1061/(ASCE)MT.1943-5533.0003353]." Note: The Doi link will not be activated until the paper is published online.